

State-dependent Charge-controlled Driving Scheme
- SQC -
A Power Saving Technology for PMOLED Displays

Dissertation

zur Erlangung des Grades des Doktors der Ingenieurwissenschaften
der Naturwissenschaftlich-Technischen Fakultät II
- Physik und Mechatronik -
der Universität des Saarlandes

von

Cosmin Codrea

Saarbrücken

2015

Tag des Kolloquiums: 26.06.2015
Dekan: Univ.-Prof. Dr. Georg Frey
Mitglieder des Prüfungsausschusses: Univ.-Prof. techn. Romanus Dyczij-Edlinger
Univ.-Prof. Dr.-Ing. Chihao Xu
Dr. Andreas Karrenbauer
Univ.-Prof. Dr.-Ing. Michael Möller
Dr. Tilman Sauerwald

Eidesstaatliche Versicherung

Hiermit versichere ich an Eides statt, dass ich die vorliegende Arbeit selbständig und ohne Benutzung anderer als der angegebenen Hilfsmittel angefertigt habe. Die aus anderen Quellen oder indirekt übernommenen Daten und Konzepte sind unter Angabe der Quelle gekennzeichnet. Die Arbeit wurde bisher weder im In- noch im Ausland in gleicher oder ähnlicher Form in einem Verfahren zur Erlangung eines akademischen Grades vorgelegt.

Sterrebeek (bei Brüssel),

European Commission Disclaimer

This work presents the findings of the research carried out by the author between 2006 and 2009 at the Institute of Microelectronics of Saarland University in Saarbrücken. In 2009 he joined the European Commission in Brussels. Neither the European Commission nor any person acting on its behalf is responsible for the use which might be made of the information contained in the present publication. The European Commission is not responsible for the external web sites referred to in the present publication. The views expressed in this publication are those of the author and do not necessarily reflect the official European Commission's view on the subject.

Abstract

The display of modern mobile devices has become a major energy demander using more than one third of system power. Organic light emitting devices (OLED) promise brilliant images, thinner and flexible panels and less power consumption. Passive-matrix OLED displays are cost-effective to fabricate and thus a good candidate mainly for small resolutions. Due to their layered structure and small inter-layer distances, they exhibit large pixel capacitances which cumulate within a column affecting each addressed pixel. Conventional driving schemes discharge them during each addressing sequence and thus waste energy. This work presents a novel concept that reuses this capacitively stored charge. It is denoted as state-dependent charge-controlled (SQC) driving scheme. *Natural* discharge is considered and the variable anode states before and after the pixel addressing sequence are predicted. An algorithm computes for each pixel the current injection and post-luminescence duration to meet accurately the nominal luminance. Dissipative discharge is almost entirely avoided. The driving scheme is validated by discrete demonstrators. Still grey-scale images are accurately reproduced, the power saving is 58% for natural images, and 43% for graphics. The robustness is proven by several means. For larger, thinner displays, this rate is expected to be higher. SQC is thus an enabling technology for a larger scale deployment of passive-matrix OLED displays.

Kurzdarstellung

Die Displays moderner mobiler Geräte sind oft *Energiefresser* und verbrauchen über ein Drittel der Systemleistung. Organische Leuchtdioden (OLEDs) bieten bessere Bildqualität, kleinere Abmessungen und verbrauchen weniger Energie. Passivmatrix-OLED-Displays sind günstiger in der Produktion und daher gute Kandidaten vor allem für kleine Auflösungen. Durch ihre mehrlagige Struktur bei geringen Schichtabständen weisen sie hohe Pixelkapazitäten auf, die in einer Spalte kumulieren und jeden adressierten Pixel belasten. Einfache Treiberschemas entladen diese bei jeder Adressierung und vergeuden dabei Energie. Diese Arbeit stellt ein neues Konzept vor, das diese kapazitive Ladung wiederverwertet. Es wird als zustandsabhängiges ladungsgesteuertes (engl. SQC) Treiberschema bezeichnet. Selbstentladung wird berücksichtigt und die variablen Anodenzustände vor und nach der Pixeladressierung werden vorausberechnet. Ein Algorithmus ermittelt pro Pixel die Strominjektions- und Nachleuchtdauer, sodass die Sollhelligkeit eingehalten wird. Dissipatives Entladen wird fast vollständig vermieden. Das Treiberschema wird mittels diskreten Demonstratoren validiert. Graubilder werden präzise abgebildet, die Leistungseinsparung beträgt 58% für Bilder und 43% für Grafiken. Die Robustheit wird auf unterschiedliche Weise nachgewiesen. Für größere und dünnere Displays wird eine höhere Einsparung erwartet. SQC ist daher eine technologische Voraussetzung für die Massenverbreitung von Passivmatrix-OLED-Displays.

Acknowledgements

Whatever we do in life, it is usually centred around our families, friends and colleagues. This long endeavour would have never materialised without their kind contribution. My dear wife Ramona has continuously been supportive and relieving while the laughter of little Livia has been more than energising and motivating. I have further received unconditioned moral and practical support from my parents Lucia and Gheorghe and am also deeply indebted to Heidi and Peter Schumann for their decisive contribution to my education.

Chihao has naturally played an instrumental role since my first day at the Institute of Microelectronics (LME). Without his constructiveness, creativity and open-mind, this work would have never happened. I am very grateful for learning among many other things about the art of *mental simulation* or the role of the *eye as a last instance* in visual testing. My deep gratitude goes also to Andreas Karrenbauer and Prof. Möller who kindly assumed the role of assessors.

I am also very grateful to the rest of the LME team, in particular to Michael Buczek who created valuable and indispensable Matlab code and to Andreas Bender for his laborious simulations. A key role played also the follow-up activity and the thesis of Yassen Dobrev that helped me resuming work after leaving the university. I am also thankful to Daniel for the many cumbersome measurements he made with great patience and accuracy. I would also like to acknowledge (in memoriam) the technical and analytical support of Hans Morgenstern.

To Ian Hodgson and John Magan I am much obliged for linguistic proofreading and the quality check. My good friends Christian and Ionuț have helped me with precious advice and I also partly modelled myself on their achievements.

I also acknowledge the financial support by the German Federal Ministry of Education and Research through the *CARO* project (BMBF-01BD688). Last but not least I am thankful to my hierarchy at the European Commission, in particular to Willy Van Puymbroeck, for his flexibility with respect to my working pattern.

Contents

1	Introduction	1
1.1	Motivation	1
1.2	Objectives	5
1.3	Methodology and Prototyping	5
1.4	Outline	7
2	OLED Displays Fundamentals	8
2.1	Organic Light Emitting Diodes	8
2.1.1	History	8
2.1.2	OLED Structure and Operating Principle	9
2.1.3	OLED Materials	10
2.2	OLED Displays	12
2.3	State of the Art of PMOLED Display Drivers	15
2.3.1	Commercial Drivers	15
2.3.2	Publications and Patents	17
3	Power Consumption in PMOLED Displays	22
3.1	OLED Display Modelling and Characterisation	22
3.1.1	The Diode	24
3.1.2	The Pixel Capacitance	24
3.1.3	The Sensing Amplification Factor k	28
3.2	OLED Luminous Efficiency	30
3.3	Resistive Power Loss	31
3.3.1	Resistive Power Loss in the Anodes	32
3.3.2	Resistive Power Loss in the Cathodes	33
3.4	Capacitive Power Loss	36
3.5	Numerical Example and Conclusions	39

4	The Principle of State-dependent Charge-controlled (SQC) Driving	43
4.1	Conventional Driving Scheme	43
4.1.1	Precharge and Discharge	46
4.2	<i>Natural</i> Discharge and Post-luminescence	49
4.3	The SQC Driving Scheme	50
5	Algorithm, Implementation and Characterisation of Display Parameters	53
5.1	Image Processing for Displays	53
5.1.1	Gamma Correction	53
5.1.2	Linearisation	55
5.1.3	Benchmarking	59
5.2	SQC Algorithms	61
5.2.1	Measurements and Characterisation Setup	63
5.2.2	2D-Look-up Tables	63
5.2.3	The 2D-Algorithm	73
5.2.4	1D-Look-up Tables and Algorithm	78
5.2.5	1D-Display Characterisation	87
6	Prototyping and Visual Validation	90
6.1	SQC Demonstrators	90
6.1.1	The <i>Spartan</i> Demo-board	93
6.1.2	The <i>Vertex</i> Demo-board	95
6.1.3	The PC Interface	97
6.1.4	Generation of Digital Control Signals in VHDL	98
6.2	Measurements and Visual Perception	101
6.3	The Impact on Display Lifetime	107
7	SQC Performance and Robustness Considerations	111
7.1	Investigation Using Matlab	112
7.1.1	Convergence of the State Variable	112
7.1.2	Image Reconstruction	114
7.1.3	Sensitivity Analysis	118
7.2	Circuit Analysis Based on PSpice Simulations	120
7.3	Calculus	122
8	Summary, Future Work and Potential Impact	127
8.1	Summary	127

8.2	Outlook and Future Work	129
8.3	Innovation Potential	130

List of Symbols and Abbreviations

δ	Duty cycle
η_{OLED}	Luminous efficiency
C_p	Parasitic pixel capacitance
C_{eq}	Cumulative parasitic pixel capacitance
f_{frame}	Frame rate
I_0	Constant current amplitude
I_{cap}	Capacitive (displacement) current
I_{inj}	Injection current
I_{Photo}	Photocurrent
Lum	Luminance
N_{col}	Number of columns
N_{row}	Number of rows
P_{cap}	Capacitive power
P_{comh}	Common cathodes power
P_{dis}	Discharge power
P_{inj}	Injection power
P_{lum}	Luminous power (electrical)
P_{res}, P_R	Resistive power
q	Number of bits
Q_{cap}	Capacitive charge
Q_{inj}	Injection charge
Q_{lum}	Recombination charge
R_{fb}	Feedback resistor
R_{ITO}	Anode resistance

R_{row}	Cathode metallic resistance
t_{50}	Display lifetime defined at half luminance
T_{frame}	Frame period
t_{inj}	Injection time
t_{lsb}	Least significant bit time increment
t_{row}	Row addressing time
t_Z	Post-luminescence time
V_i, Q_i	Initial state
V_{col}	Anode voltage
V_{comh}	Common cathodes (idle) high voltage
V_{dis}	Discharge voltage
V_{FD}	Forward voltage
V_{i+1}, Q_{i+1}	Final state
V_{pre}	Precharge voltage
V_{th}	Threshold voltage
<i>AMOLED</i>	Active-matrix Organic Light Emitting Diode
<i>CAE</i>	Computer-aided Engineering
<i>CCFL</i>	Cold Cathode Fluorescent Lamp
<i>CMLA</i>	Consecutive Multiline Addressing
<i>CMOS</i>	Complementary Metal-oxide Semiconductor
<i>CRT</i>	Cathode Ray Tube
<i>EL</i>	Emissive Layer
<i>FPGA</i>	Field Programmable Gate Array
<i>FSLA</i>	Flattened Singleline Addressing
<i>FSM</i>	Finite State Machine
<i>GPS</i>	Global Positioning System
<i>GUI</i>	Graphical User Interface
<i>HOMO</i>	Highest Occupied Molecular Orbit
<i>HTL</i>	Hole Transport Layer
hZ	High-impedance
<i>I/F</i>	Interface

Contents

<i>I/O</i>	Input/Output
<i>IC</i>	Integrated Circuit
<i>ISR</i>	Interrupt Service Routine
<i>ITO</i>	Indium-Tin-Oxide
<i>JPEG</i>	Joint Photographic Experts Group
<i>LCD</i>	Liquid Crystal Display
<i>LME</i>	Lehrstuhl für Mikroelektronik
<i>LUMO</i>	Lowest Unoccupied Molecular Orbit
<i>LUT</i>	Look-up Table
<i>MLA</i>	Multiline Addressing
<i>OLED</i>	Organic Light Emitting Diode
<i>PC</i>	Personal Computer
<i>PCB</i>	Printed Circuit Board
<i>PLED</i>	Polymer OLED
<i>PMOLED</i>	Passive-matrix Organic Light Emitting Diode
<i>PROM</i>	Programmable Read-Only Memory
<i>PWM</i>	Pulse-width Modulation
<i>RAM</i>	Random Access Memory
<i>RGB</i>	Red Green Blue
<i>SLR</i>	Single-lens Reflex
<i>SMOLED</i>	Small-molecules OLED
<i>SQC</i>	State-dependent Charge-controlled
<i>TFT</i>	Thin-film Transistor
<i>TMA</i>	Total Matrix Addressing
<i>UART</i>	Universal Asynchronous Receiver-Transmitter

1 Introduction

1.1 Motivation

Smart mobile devices have changed our lives. Advances in miniaturisation and functional integration led to enabling technologies like mobile communication, mobile internet and the breakthrough of smartphones. Today, a smartphone has more computing power than existed in all of NASA in 1969 [59] and can even be used in satellites [55]. Fast processors, high-resolution displays and cameras, GPS receivers and several radios and sensors turn it into a *smart*, versatile companion, customisable by means of apps. While the cost of technology for one device would have been several million Euro a decade ago, today it can be considered as empowering innovation due to its availability, affordability and spread. High-speed mobile internet and permanent connectivity are laying the cornerstone for cloud computing while further miniaturisation and functionalisation are paving the way towards the Internet of Things.

We expect today high-definition crisp images and videos on displays of any size. The display is usually the main bidirectional human-machine-interface, in particular since it can be equipped with a touch-screen present nowadays in most modern mobile devices.

OLED displays are already a major competitor for LCDs although they are more expensive in manufacturing which is still a major drawback [39]. Nevertheless, they have decisive superior performance in terms of contrast, thinness, lightness, power consumption, response speed and viewing angle which are all quantified in Table 1.1.

OLEDs are taking an increasing share, mainly in the mobile phone, mobile PC (tablet, notebook) and TV market [19]. Furthermore, smart watches and fitness monitors are emerging applications. Figure 1.2 depicts some very recent active-

1 Introduction

	AM OLED	AM LCD
Thickness/weight	Thinner, best is 0.05 mm; lighter	Thicker, best is 0.8 mm; heavier
Diagonal Size	Limited to small and medium sizes; largest demo is 77"	Can be manufactured larger; largest demo is ~100"
Viewing Angle	Up to 180 degrees	Narrower, depends on liquid crystal type
Color Gamut	>100% NTSC (top emission), ~70% NTSC (bottom); high at all gray levels	~70%, up to ~100% NTSC (LED backlight and new color filter); falls at low gray levels
Color Reproduction	Better; gamut independent of view angle	Good; gamut changes with viewing angle
Resolution	Lower; 308 dpi (SM), 202 dpi (polymer)	Higher; best is 498 dpi
Response Time	Faster, nanoseconds. No motion blur, good for 3D	Slower, milliseconds
Contrast Ratio	Higher > 100000	Lower < 10000
Sunlight readability	Better than transmissive LCD, worse than transfective LCD	OK if transfective
Operating Temperature	Range is larger, can operate at low temps like -40°C.	Range is smaller, lowest temp is -10°C.
Power Consumption	Lower at typical video content when ~30% of pixels are on	Higher at typical video content
Lifetime	Shorter, up to 30K hour, but improving	Much longer, above 50K hour
Manufacturing Investment	Lower, but lack of standards keeps the investment only slightly lower	Higher
Production Cost	Expensive; low yield, potential to be low cost	Cheaper than AMOLED

Table 1.1: OLED and LCD display characteristics (adapted from [19])

matrix OLED (AMOLED) products. Commercial screen size and resolution have steadily increased in recent years, now being deployed up to 77 inch 4K (3840 x 2160) screen TVs [72].



Figure 1.2: Recent products with AMOLED displays (not to scale): LG *OLED TV* [46], Samsung *Gear S Smartwatch* [16], Samsung *Tablet S* [62]

Beside AMOLED, passive-matrix OLED (PMOLED) is a promising display technology, in particular for small displays as they are easier and cheaper to fabricate. Due to the limitation in display size - the largest PMOLED display is only 5", and most of them are around 1" to 3" - they have been however mainly commercialised as sub-displays for clamshell phones [50]. A decade ago they dominated AMOLEDs in unit shipments (figure 1.3). Today AMOLED is however the established technology, in particular due to its longer lifetime, better power rating and higher resolution but also as a consequence of more cost-effective manufacturing technologies. OLEDs are also increasingly used in signage and lighting [19].

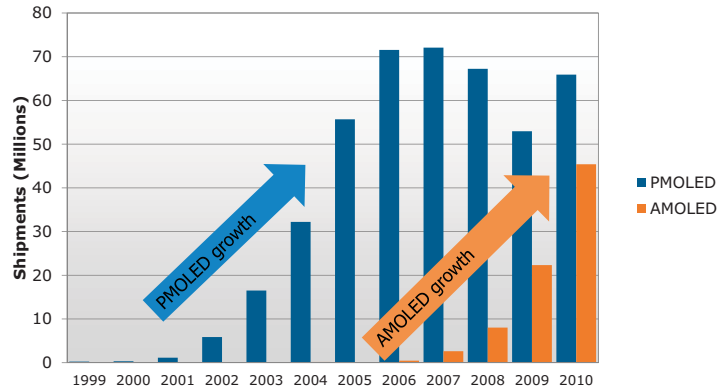


Figure 1.3: PMOLED and AMOLED displays unit shipments [19]

A competitive edge of OLED displays is also their potential transparency and flexibility [50]. In conjunction with the low manufacturing cost of PMOLEDs, this leaves room for several niche applications. Figure 1.4 shows some recent PMOLED products. NB: The Lenovo *S800* mobile phone driver chip uses the in-house (LME) multiline addressing technique [87].

The battery remains a constraint for mobile applications with the display accounting for more than one third of the overall power budget both in LCD based portable PCs and mobile devices with OLED displays (figure 1.5) [71]. Furthermore, zero-power electronics are considered essential for future technological innovations.

The focus of this research was mainly motivated by the much lower manufacturing costs of PMOLED and the commercial balance between PMOLED and AMOLED when the work started. The goal is to improve the performance of PMOLED displays modules by considerably reducing the capacitive power loss. As explained in section 2.3.1, the work was triggered by the accidental discovery of an increase

1 Introduction



Figure 1.4: Recent products with PMOLED displays: Huawei *Talkband* [35], *MD300 C2* Pulse Oximeter [49], Lenovo *S800* mobile phone [45], Sony Ericsson *Live View* watch [70]

in overall luminance when introducing a high-impedance anode driving state.



Figure 1.5: Power consumers in notebooks with CCFL Backlight (left) [71] and in an Android smartphone with an AMOLED display (right) [own screenshot]

1.2 Objectives

The purpose of this work is to reduce the power consumption of PMOLED display modules to allow their large-scale deployment. An early finding was that the main loss is due to the waste of capacitive charge which is proportional to the square of the number of rows. Eliminating this loss would facilitate the use of higher resolutions displays in mobile applications and a faster market penetration. To this end the main objectives are threefold:

- Realisation of an appropriate OLED display model and simulation environment.
- Elaboration of a new power-efficient driving scheme and corresponding algorithms.
- Off-chip hardware implementation and benchmarking.

Once demonstrated, the driving scheme is expected to be assessed in terms of robustness and sensitivity to display parameter variation.

1.3 Methodology and Prototyping

This section gives an overview of the methodology and timing of the present work.

The research and development work was carried out between 2006 and 2009 and started with the elaboration of a PSpice OLED model and the set-up of a simulation environment for a 32 x 24 Polymer OLED (PLED) display. By this means dynamic crosstalk was investigated (figure 1.6) and could be prevented with appropriate cathode driving.

A next step was the development of a demonstrator for PMOLED multiline addressing [87] using a 128 x 64 2.7" Osram PLED display.

Multiline addressing was then demonstrated within an industrial project on a higher resolution colour display using the versatile Xilinx *FF1760* Prototyping Platform [82] and the OKI *ML9362* integrated driver [57]. The unintentional activation of a driver setting allowing high-impedance anode driving (section 2.3.1) revealed a considerable increase in overall display brightness paving the way towards the investigation of the capacitive power loss.

A first attempt to reduce the capacitive power loss by allowing high-impedance

1 Introduction

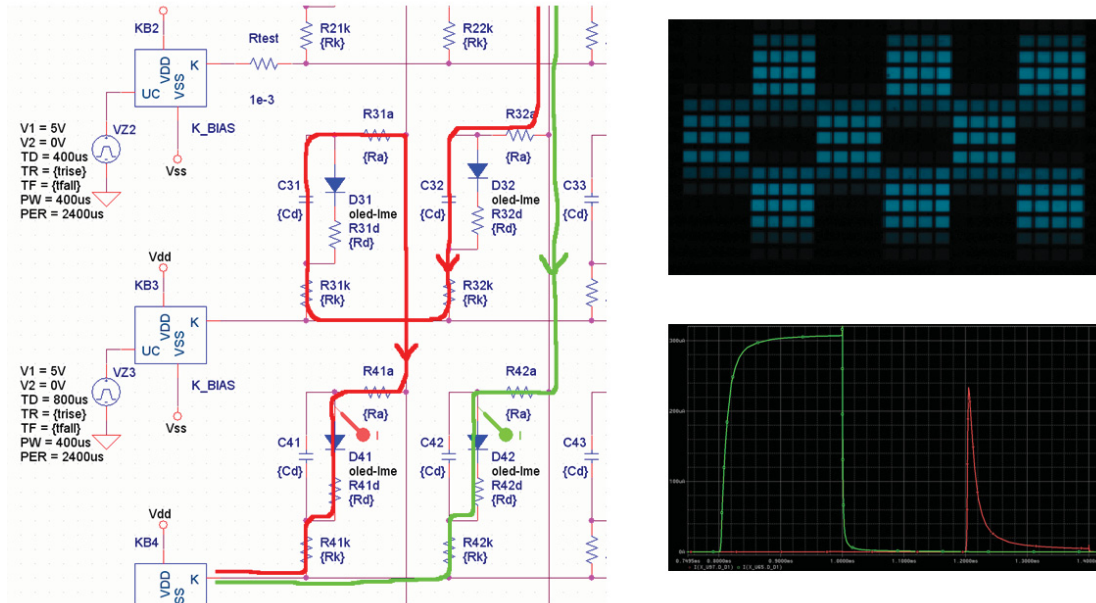


Figure 1.6: Simulation and illustration of dynamic crosstalk

cathode states was made in the framework of a diploma thesis [4], also by employing the SLPS mixed-signal simulation environment for Matlab and PSpice.

The research focussed afterwards on the introduction of high-impedance anode driving and the novel driving scheme SQC [88] which is the core subject of this thesis. A larger demo-board was built (section 6.1.2) and 2D-look-up tables for display characterisation were recorded. The 2D-algorithm (section 5.2.2) was externally realised in Matlab [9] allowing the validation of the SQC concept. It was followed by implementation and hardware validation of the innovative 1D-approach (section 5.2.4). The development and measurement results were then published [17].

The final part of the work was devoted to the assessment and demonstration of SQC robustness and stability.

Within a follow-up activity [24], a concept for an SQC image processor has been realised.

The following CAE tools have been used throughout the present work ([10], [47], [48], [80], [81], [51],[25]):

- Cadence Allegro PSpice

- SLPS
- Matlab
- Modelsim Xilinx Edition-III
- Xilinx ISE Design Suite
- Microsoft Visual C++
- Eagle

1.4 Outline

Chapter 1 has introduced the motivation behind the present work, its objectives and methodology. Chapter 2 presents the fundamentals of OLEDs and OLED displays and the state of the art of PMOLED display drivers. In chapter 3 the power consumption in PMOLED displays is broken down, analysed and compared with a numerical example. Chapter 4 introduces the SQC driving scheme highlighting its benefits with respect to the state of the art. Chapter 5 sets out the core findings of the present work, detailing the development of two SQC algorithms. Chapter 6 shows their implementation in hardware, the realisation of hardware demonstrators including digital FPGA-based design, measurements and visual results as well as lifetime considerations. Chapter 7 demonstrates the robustness and stability of SQC driving by means of simulation, digital image reconstruction and calculus. The final chapter 8 recapitulates the main conclusions and discusses possible further work.

2 OLED Displays Fundamentals

This chapter provides an overview of the structures and working principles of OLEDs and OLED displays. The state of the art of PMOLED display drivers is then presented.

2.1 Organic Light Emitting Diodes

2.1.1 History

Electroluminescence in organic (i.e. carbon based) materials was first observed in the early 50s at Nancy University. Hole and electron injecting electrode contacts which are the basis for charge injection in all modern OLED devices were developed in 1960 at New York University. Electroluminescence from polymer films was first recorded at the National Physical Laboratory in the UK and patented in 1975 [78]. In these early days primitive sample preparation techniques, poor quality electrode contacts, and the low purity of the organic materials were largely responsible for an inferior performance and very high operating voltages needed, typically hundreds of volts [60]. Significant improvements have been made since then in vacuum processing techniques and purification methods for organic dye molecules, resulting in devices with much lower operating voltages. The first modern diode device with separate hole and electron transporting layers was reported at Eastman Kodak in 1987. Recombination and light emission occurring in the middle of the organic layer allowed an operating voltage below 10 V and a higher efficiency. Most modern OLEDs are based on this original design. A ground breaking high efficiency green polymer based device was reported in 1990 at the Cavendish Laboratory in Cambridge. The first OLED display prototype (320 x 240) was produced in 1996 by TDK [78][89] and in 1997 Pioneer Corporation released the first commercial OLED product, a passive-matrix OLED display for

car audio displays. A decade later in 2007 Samsung Mobile Display released the first commercial active-matrix OLED display [60].

2.1.2 OLED Structure and Operating Principle

OLEDs have a multilayer structure depicted schematically in figure 2.1. A glass substrate sustains the transparent anode. This is made usually of Indium-Tin-Oxide (ITO), a material sufficiently conductive and transparent [24] [75]. On top of the anode there are at least two organic layers, the hole transport or conductive layer (HTL) and the emissive layer (EL). Apart from conducting holes induced by the anode, the HTL improves the efficiency by shifting recombination and light generation from the EL-cathode barrier to the inside of the EL [24]. Conventional materials for the HTL are Copper Phtalocyanine (CuPc) or Polyaniline (PAni). The emissive layer, e.g. an organic dye, is the place of charge recombination and determines the wavelength of the emitted light. The top electrode is the metallic cathode. Metals with low work function like Aluminium (Al), Magnesium (Mg) or Calcium (Ca) are used to facilitate the injection of electrons [24]. The cumulative thickness of the organic layers is around 100 nm. Anode and cathode account for about an additional 100 nm each. Nevertheless, all together these layers sum up roughly to only 1/3600 of the substrate thickness [89].

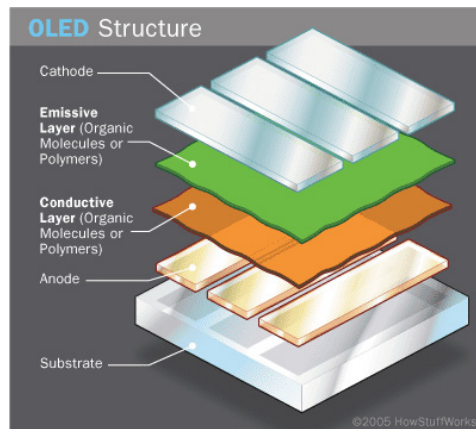


Figure 2.1: The layered structure of an OLED [29]

The organic molecules are electrically conductive as a result of de-localisation of π electrons which can *hop* from molecule to molecule or from polymer to polymer

[89]. The highest occupied and lowest unoccupied molecular orbitals (HOMO and LUMO) of these organic semiconductors correspond to the valence and conduction bands of inorganic semiconductors [78].

During operation, a voltage is applied across the OLED such that the anode is positive with respect to the cathode. Electrons are injected into the LUMO of the emissive layer at the cathode and withdrawn from the HOMO of the conductive layer at the anode, generating holes (figure 2.2). Electrostatic forces bring the electrons and the holes together and they recombine forming a bound state called exciton. This happens closer to the emissive layer because in organic semiconductors holes have generally a higher mobility than electrons. The decay of this excited state results in emission of radiation in the visible spectrum as a function of the band gap of the material, in this case the energy difference between HOMO and LUMO [78].

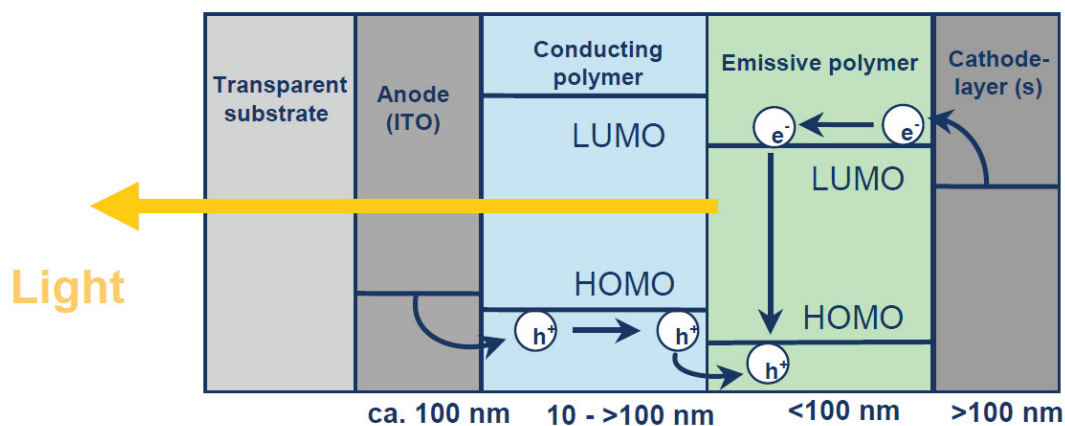


Figure 2.2: OLED energy diagram [1]

2.1.3 OLED Materials

Two processing techniques distinguish small-molecule (SMOLED) from polymer (PLED) OLEDs.

The production of small-molecule devices usually involves thermal evaporation (deposition) in a vacuum which makes the process relatively expensive. However, contrary to polymer-based devices, this enables the formation of well controlled, homogeneous films and the construction of very complex multi-layer, even RGB

structures. Molecules commonly used are organometallic chelates (e.g. Alq₃), fluorescent and phosphorescent dyes and conjugated dendrimers. This high flexibility in layer design enabling additional distinct charge transport and charge blocking layers is the main reason for the high efficiencies of SMOLEDs [78]. Figure 2.3 depicts the cross section of multilayer SMOLEDs and PLED and summarises their properties.

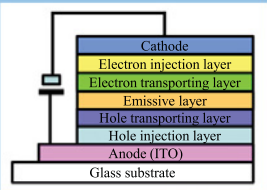
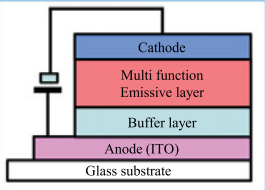
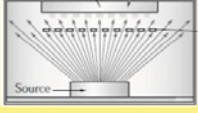
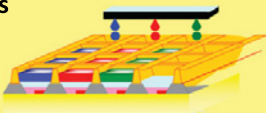
	Small Molecule	Polymer
		
Process	Dry process (Vacuum evaporation) 	Wet process 
Patterning	Shadow mask	Printing (IJ etc.)
Structure	Complex layer structure (5-6) →Complex process	Simple layer structure (2-3) →Simple process, scalable
Material	Separated function	Integrated function
Issue	Layer structure complexity Difficulty in mask patterning	Performance (esp. LT) Patterning technology

Figure 2.3: Small-molecule and polymer OLED layer structure and properties [63]

Vacuum deposition is not a suitable method for forming thin films of polymers as they degrade with the high temperature. Polymers can be processed in solution and deposited in a thin film either by spin coating or ink-jet printing. Spin coating is more suitable to form large-area films than thermal evaporation. However, as the application of subsequent layers tends to dissolve those already present, formation of multilayer structures is cumbersome. Typical polymers used in PLED displays include derivatives of poly(p-phenylene vinylene) (PPV) and polyfluorene (PF).

Figure 2.4 compares SMOLEDs and PLEDs in terms of efficiency and lifetime. In spite of higher production costs, SMOLEDs are more widely spread today due to the higher efficiency (in particular of blue pixels) and lifetime.

Latest PLED performance 2012/Autumn						C D T	
Spin/BE data @1000cd/m2	Red			Green		Blue	
Efficiency [cd/A]	11	21.8	31	56	73	9.4	10.0
Colour (C.I.E. x,y)	x=0.67 y=0.32	x=0.65 y=0.35	x=0.62 y=0.38	x=0.32 y=0.63	x=0.31 y=0.64	x=0.14 y=0.14	x=0.15 y=0.12
T50 lifetime [hrs]	200k	>350k	352k	296k	~100k	20k	13k
Vd [V]	6.0	4.1	4.2	5.1	4.7	4.5	4.2

*Lifetime estimated from acceleration test

Phosphorescent Emitter Material	Luminous Efficiency (Cd/A)	Operating Lifetime in hours (LT 95%)	Operating Lifetime hours (LT 50%)
Deep Red	17	14,000	250,000
Red	30	50,000	900,000
Yellow	81	85,000	1,45,000
Green	85	18,000	400,000
Light Blue	50	700	20,000

All figures are for bottom-emitting structures that have been fabricated with vacuum thermal evaporation technique

Figure 2.4: Performance of polymer (top, [61]) versus small-molecule OLEDs (bottom, [53])

2.2 OLED Displays

There are two types of OLED displays with a specific physical structure requiring different driving methods.

Passive-matrix displays (PMOLED) have two orthogonal electrode arrays (figure 2.5). At each crossover, the organic layer is between an anode and cathode plate forming a pixel. The pixel is lit by connecting the anode to a current source and switching the cathode to ground. A matrix of m rows and n columns thus drives $m \times n$ pixels in total.

The main benefit of PMOLED displays is their cost effective production. At the same time, the need for multiplexed driving with one row active at a time throughout a frame period causes a series of drawbacks. During the addressing time of one line, each active pixel has to produce sufficient light for the human eye to perceive the nominal luminance time averaged over the frame period. Under this constraint, a very high current amplitude is needed causing the pixels to

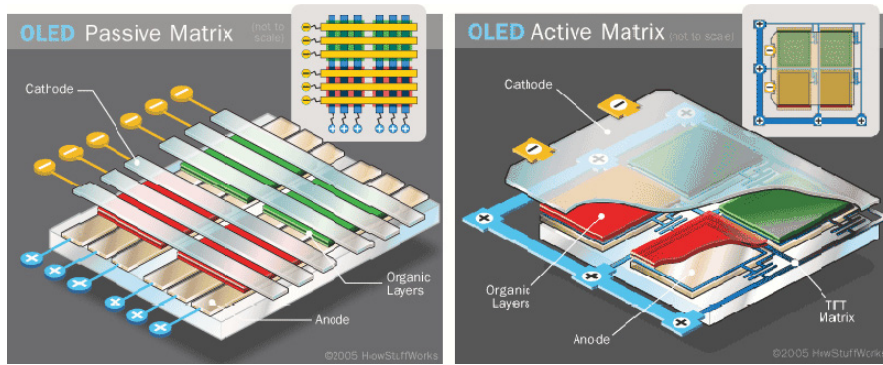


Figure 2.5: PMOLED and AMOLED schematic drawing [29]

degrade quicker. Furthermore, the high current produces heat across the column resistance which in turn also impacts its life. This degradation process has been quantified in [86]. Conventional PMOLED driving is also confronted with a large capacitive power loss, which is the subject of the present work. For these reasons PMOLED displays are limited in size, with diagonals typically up to 3" [50].

AMOLED displays use a TFT-capacitor back-plane to keep each pixel turned on during the frame period, allowing a low driving current and in turn a much larger display size. The main drawback of this technology is cost, provided that the driving transistor is used in analogue control, posing stringent manufacturing constraints and affecting yield. The simplest possible AMOLED display pixel architecture consists of two TFTs and one capacitor in which one TFT is used for selecting and charging the storage capacitor while the second TFT functions as current source to drive the diode [77]. Figure 2.6 shows a topology with independently controllable *Write-Select* and *Drive-Select* lines used to compensate for TFT and/or OLED threshold-voltage drifts. Usually, more complex AMOLED pixel architectures employing further compensation transistors are required. Nevertheless, novel digital driving schemes are promising candidates to lower complexity, cost and power consumption [76].

The intrinsic properties of OLED displays give many advantages over LCDs and have attracted major display players to invest in R&D and manufacturing [54]. The main benefits are:

- Unlike liquid crystal, field emission or plasma displays, which require thin-film processing on two glass plates, OLED can be totally fabricated on one sheet of glass or plastic. This greatly simplifies the manufacturing processes and makes

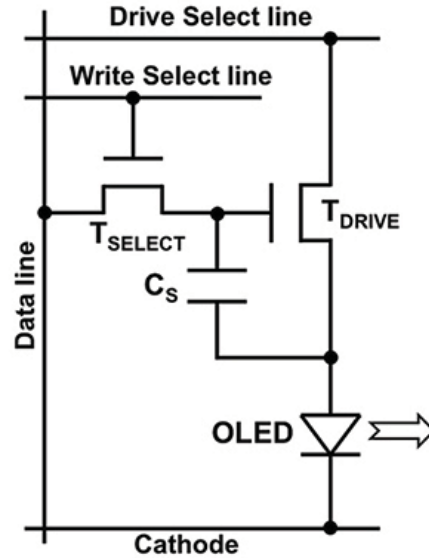


Figure 2.6: AMOLED pixel circuit [77]

them also suitable for flexible or transparent displays as well as for lighting.

- OLED displays are thinner and lighter than competing display technologies [33] and are thus very convenient for small portable applications.
- The charge recombination process causes very little time delay which results in a time-response time about three orders of magnitude faster than LCD [89]. The major response time inhibitor is the parasitic pixel capacitance.
- OLED displays are self-emissive, therefore no backlight is required and the viewing angle can be very large in all directions. Colour filters are also not necessary which improves the light transmission efficiency and reduces power consumption. OLED displays naturally produce sharp, brilliant images.
- The power consumption of an OLED is proportional to its average luminance. Thus, for darker images OLED power consumption is low while for LCDs it is nearly independent of the image content.

At the same time, the following drawbacks hinder a faster OLED display market penetration:

- While the lifetime of red and green OLEDs is sufficiently long, the life of blue pixels is still a major concern (figure 2.3) due to heat dissipation [24] [54] [19]. Pixels addressed more often also degrade faster leading to differential ageing and image sticking.
- Encapsulation is essential as OLEDs degrade through oxidation or moisture.

- The manufacturing cost is still 10-20% higher than for LCDs but it is expected to fall below it in the next few years [31].

PMOLED and AMOLED displays have individual advantages and strengths and are used in their own application fields. In this thesis the focus is on a new efficient driving scheme for PMOLED displays.

2.3 State of the Art of PMOLED Display Drivers

In the present work the display driver is considered to be the electronic component between the digital image controller and the display itself. It generates the electric currents and voltages required to illuminate pixels and produce images.

The object of this work is the elaboration and implementation of a power-efficient driving scheme for PMOLED drivers. For this reason the overview on the state of the art is restricted to PMOLED drivers and driving schemes. It contains brief description of available commercial products and a section on relevant publications and patents.

2.3.1 Commercial Drivers

The Clare Micronix *MXED102* (anode) and *MXED202* (cathode) drivers [15] were the display industry's first off-the-shelf solutions for use with OLED displays. They can drive together 128 rows and 240 columns and the row number can be doubled by applying dual-scan techniques. The driving sequence starts with a voltage precharge followed by a constant current phase. Then the output is switched to ground. The segment driver can source $4\mu A$ to $1mA$ with tight current matching allowing for 6-Bit monochromatic or colour grey-scale user control.

SSD1331 from Solomon Systech is a single-chip CMOS driver with 288 segments and 64 commons output, supporting up to 96RGB x 64 dot-matrix displays [68]. It has programmable frame rate, 256-step contrast, 65K colour and 7-bit pixel brightness control. The segment maximum source current is $200\mu A$. Driving starts with a reset (discharge) phase with the anodes switched to ground. It is followed by a voltage and a current precharge phase with adjustable amplitudes and by a constant current phase. Then the anode is switched to ground.

The OKI *ML9362* is an anode driver with 258 ($86 \times \text{RGB}$) driver outputs [57]. Combined with the cathode driver *ML9372* it can drive a full-dot panel. It features 7-bit adjustable anode output current up to $400 \mu\text{A}$ and 5-bit adjustable pixel luminance. It has a unique output adjustment function to set all outputs *High*, *Low*, or *High-Impedance*. Figure 2.7 depicts a timing diagram showing the anode voltages in high-impedance state once the injection time has elapsed. Moreover, when passing from one row to another the anodes can also be globally left open. This customisation is very close to the requirement of SQC driving (chapter 5). The missing capability to discharge anodes individually and the relatively low grey-scale resolution (5-bit) prevents it from demonstrating this novel driving scheme. Nevertheless, this pair of drivers has been used to demonstrate multiline addressing (chapter 1, section 2.3.2).

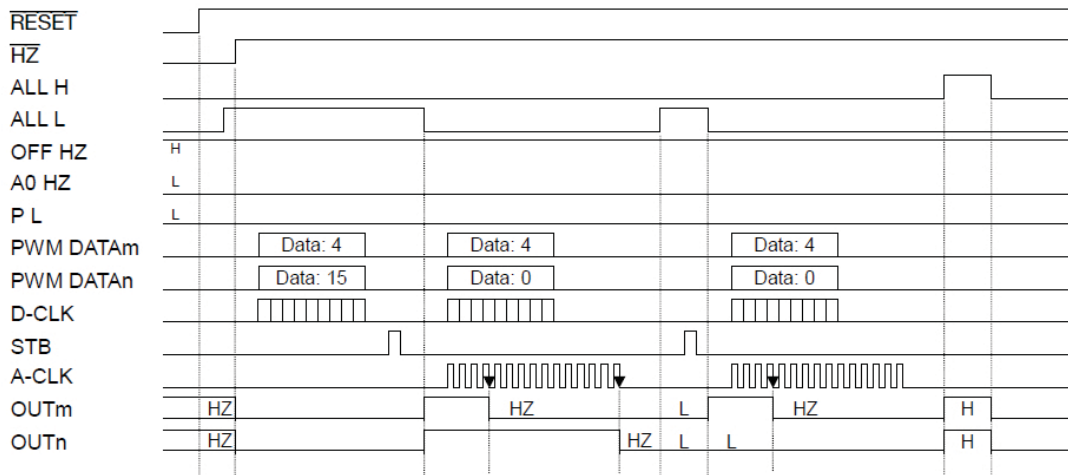


Figure 2.7: Timing of the OKI *ML9362* anode driver with high-impedance anodes [57]

The most recent commercial driver is *DA8620* from Dialog Semiconductor. It supports resolutions up to $240\text{RGB} \times 320$ with 24, 18 or 3-bit colour modes and programmable gamma-curves. The maximum anode driving current is $133 \mu\text{A}$ and the pre-charge current is 8-bit programmable up to $640 \mu\text{A}$. Apart from a very accurate dynamic current matching, it is the only commercial implementation of multiline addressing (section 2.3.2) under the market name *SmartXtend*. The datasheet does not disclose the driving scheme, however the product brief states a considerable reduction of precharge current which accounts for 50% of the power budget [21] which could mean in turn that the driver is using the patented *back-to-back* technology mentioned in section 2.3.2. The chip is assembled in a TDK

transparent PMOLED module and is used in the Lenovo *S800* mobile phone series [45].

2.3.2 Publications and Patents

G. Landsburg highlights in [42] several challenges of PMOLED driving with a particular focus on the capacitive power loss. A numerical example underpins the main findings of the present work in terms of the dominance of capacitive power consumption which is also confirmed in further literature [21] [52]. Landsburg states however that "the parasitic capacitance must be charged and discharged each row cycle", which is now proven to be valid for conventional driving only.

J.-S. Yang et al. present in [91] a method to avoid the pre- and discharge phase every other line. It is implemented by means of so-called end-line and first-line pulse-width modulation (PWM) and is similar to the *back-to-back* technique [69]. In each *end-line* PWM, the start of the precharge and the current injection phase are delayed so that the latter ends with the row addressing time and is followed by a conventional *first-line* PWM. In between, there is an idle phase during which the capacitive charge is kept constant by means of high-impedance anodes (figure 2.8). To implement this driving sequence, grey-scale characterisation is due for both the end-line and the first-line PWM part. In principle this method should allow for ca. 50% of the SQC power saving capability. It has been tested on a prototype driver chip with a reported reduction of injection current of up to 35%.

The application note [54] outlines the necessity of precharge and linearisation. The latter is further discussed in section 5.1.2.

A series of papers and patents deal with optimisation of the precharge phase and current source performance to improve image quality and power consumption:

D. Chaussy et al. present in [12] a driver topology that senses the OLED forward voltage and dynamically adapts the precharge voltage accordingly. It is similar to the invention proposed in [43] and is used to compensate for parasitic effects in the ITO line and for column ageing. Furthermore, the cathode idle voltage V_{comh} and the voltage supplying the anode current sources are minimised in a similar manner in order to reduce the power budget.

J. Kim et al. suggest in [40] a new data output circuit with the aim of addressing the non-uniform brightness of an OLED panel due to IC process parameter vari-

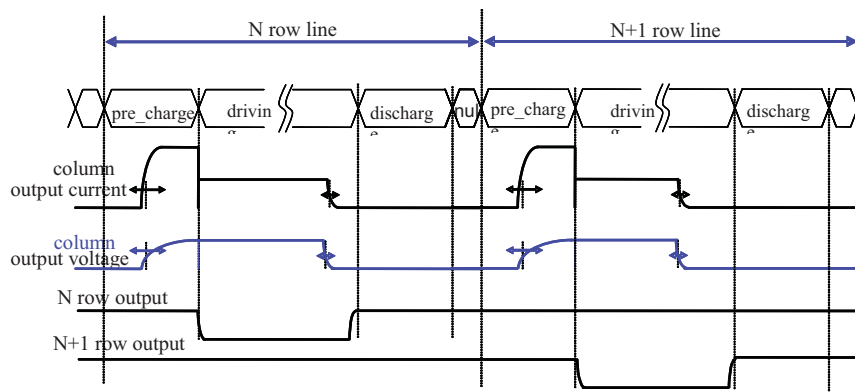


Fig.1 conventional driving sequence

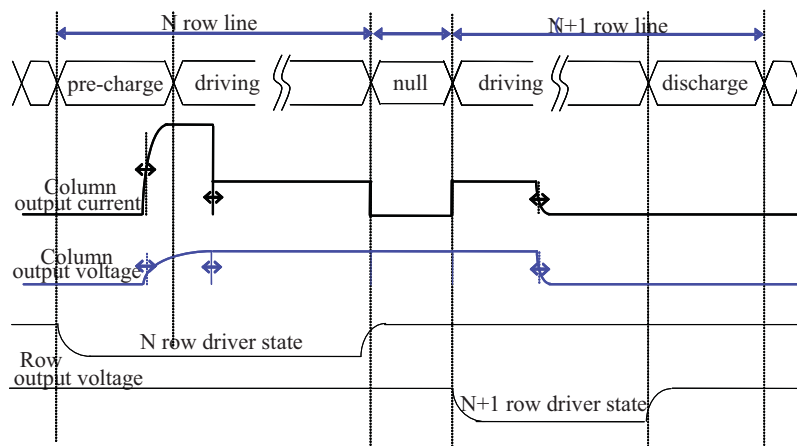


Figure 2.8: Driving sequence with pre- and discharge restricted to every other row [91]

ation. The suggested method connects all the output terminals of the switching transistors via a resistor and an additional transistor per segment to compensate for the threshold voltage differences and allow high precision precharge and current injection.

G. Thanghe et al. present an invention [73] comprising four precharge sub-circuits to realise a nearly rectangular OLED driving waveform.

R. LeChevalier presents in [44] a driving sequence with partially overlapping precharge and constant current phases to avoid an anode voltage drop.

S.-L. Chen has patented a method to compensate by means of conventional PWM for the absence of luminance during low grey-values if no precharge is carried out [14]. The method seems very similar to the linearisation technique presented in

section 5.1.2.

S.-Y. Chen et al. show in [13] a driving sequence to reduce the overall peak current of the anode driver by alternating synchronous PWM starting rows with synchronous PWM ending rows.

A. Somerville et al. present in [69] the *Back to Back Pre-charge Scheme*. As in [91], precharge is avoided every other line by delaying the start of the injection time so that the injection phase ends simultaneously with the row addressing time. The next row injection time can start right away without the need to discharge the anode.

Miller et. al. outline in [52] an invention very similar to SQC. The presented method also avoids pre- and discharge cycles for reducing the power consumption and considers the change in charge (voltage) between the beginning and the end of addressing. It makes use of image information from consecutive rows to adjust the pixel driving time and amplitude, the latter in particular if the next pixel is very dark. The basis for calculation is the current/voltage curve of the OLED and the assumption that during the natural discharge phase when the pixel capacitance is discharged by the light emitting diode, the anode voltage will decay to the threshold voltage. The way of handling the dynamic behaviour, i.e. when the OLED current and voltage do not reach this stationary state is not disclosed. A calculation based on static values may lead to wrong luminances since the row addressing time is very short.

The patent application of J.-P. Dagois [20] bears also a substantial resemblance to SQC. The approach of reusing the intrinsic capacitive charge by converting it into effective luminance is very similar. The charge stored in the cumulative parasitic capacitance is however made available to the active pixel at the beginning of the row addressing time employing the same principle of a floating (high-impedance) anode state. By means of look-up-tables (LUTs), the invention claims to estimate the charge yielded to the active pixel as a function of the available capacitive charge and the *pre-luminescence* duration. The processor is thus looking for the appropriate duration of this phase, so that in conjunction with the subsequent current injection time, the nominal luminance charge is met. This approach comprises however two questionable assumptions which cast its accurateness into doubt and the two are to some extent related. On one hand, the anode voltage is considered constant during the constant current injection

phase and is not reflecting the OLED circuit behaviour given the considerable trace resistances and OLED capacitances. This has been confirmed by calculus, simulations and measurements. On the other hand, a more critical assumption concerns the so-called *overlapping* case, when the appropriate combination of pre-luminescence and constant current injection has to be determined. In this situation the luminance charge is considered proportional to the injection time. In reality, this quantity also depends on the initial charge and moreover, the pixel current is not constant as the injection current is shared with the cumulative parasitic capacitance as well. These inconsistencies would lead to an inaccurate reproduction of the nominal pixel luminance. As SQC considers the variable initial and final pixel charge and reuses almost entirely the capacitive energy, its novelty remains valid.

Multiline addressing is a method to drive several rows simultaneously. By this means, the frame period is minimised as the rows are scanned in a shorter time. In consequence, the frame period can be extended to the initial value and the constant current amplitude can be reduced proportionally, extending the display lifetime and reducing the power consumption. This can be accomplished by means of a variable row addressing time which corresponds to the brightest pixel in the row. The key challenge in multiline addressing is the decomposition of the original image matrix into sub-frames corresponding to the number of rows driven simultaneously. Xu et al. and E.C. Smith present two methods in [87] and [64] respectively. While the former method (CMLA) makes use of lossless decomposition techniques based on addition and subtraction, the latter (TMA) employs non-negative matrix factorisation which is not lossless and may cause artefacts. The development of an MLA demonstrator [87] was a preliminary activity preceding the current work. Figure 2.9 shows an example for CMLA image matrix decomposition. Dialog Semiconductor has implemented this method in a driver IC under the market name *SmartXtend* [21]. The chip is being used by Lenovo in the *S800* mobile phone.

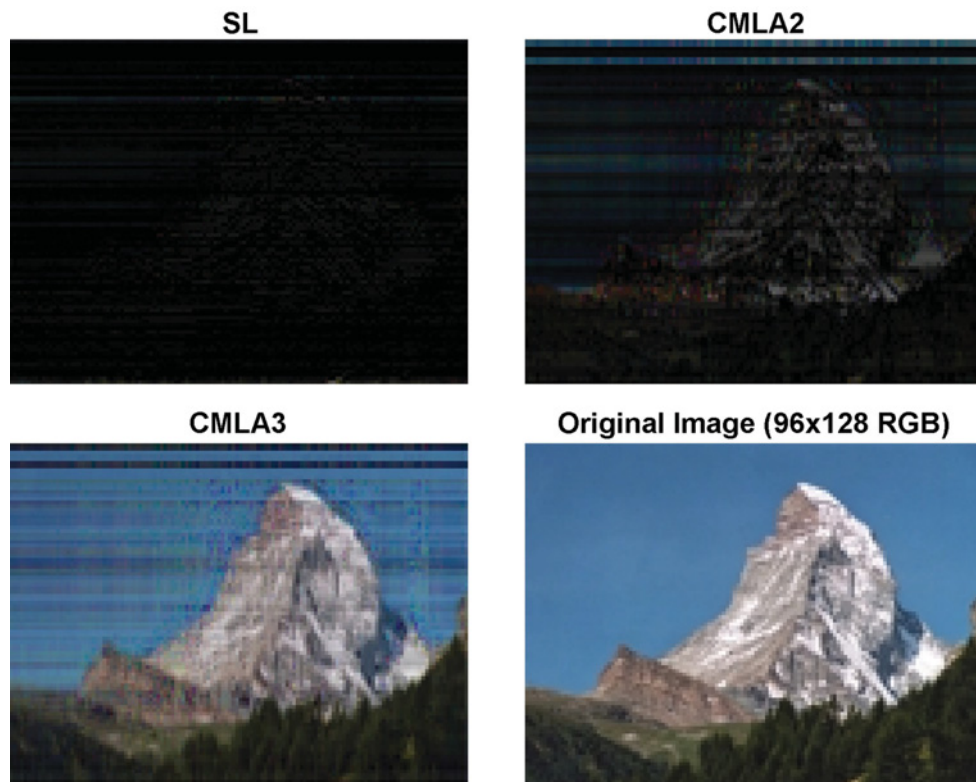


Figure 2.9: Matrix decomposition for Consecutive Multiline Addressing (CMLA)
[87]

3 Power Consumption in PMOLED Displays

The objective of this thesis is the considerable reduction of the capacitive power loss which in turn would translate into a substantial reduction of the total power consumption of PMOLED display modules. This chapter introduces a section on modelling and parameter extraction to identify the different root causes for power dissipation. The oled luminous efficiency, the resistive and capacitive power losses are assessed quantitatively and compared numerically. Finally, the new driving scheme is described in detail.

3.1 OLED Display Modelling and Characterisation

A concept for OLED electrical modelling via SPICE is presented in [3] and is based on experimental data. In principle, three individual OLED organic layers - hole injection (HI), hole transport (HT) and electron transport (ET) - are modelled as a capacitor shunted by a diode and a series resistor (figure 3.1b). The capacitance is a function of the thickness of the corresponding layer and the dielectric constant of the material. The relatively large series resistor is the consequence of the low mobility of the organic materials. A resistor in series to this stacked model accounts for the sheet resistance of the ITO anode. The relatively small cathode resistor is neglected. The layered capacitors, resistors and diodes can be combined into a simplified model with one part per component, as depicted in figure 3.1c. In spite of some limitations of the traditional silicon-based PSpice diode model, experience shows that this simplified model is sufficiently accurate to allow for matching experimental and simulation results and has been used for the purpose of this work.

The electrical parameters per pixel of the available OSRAM 128 x 64 greyscale

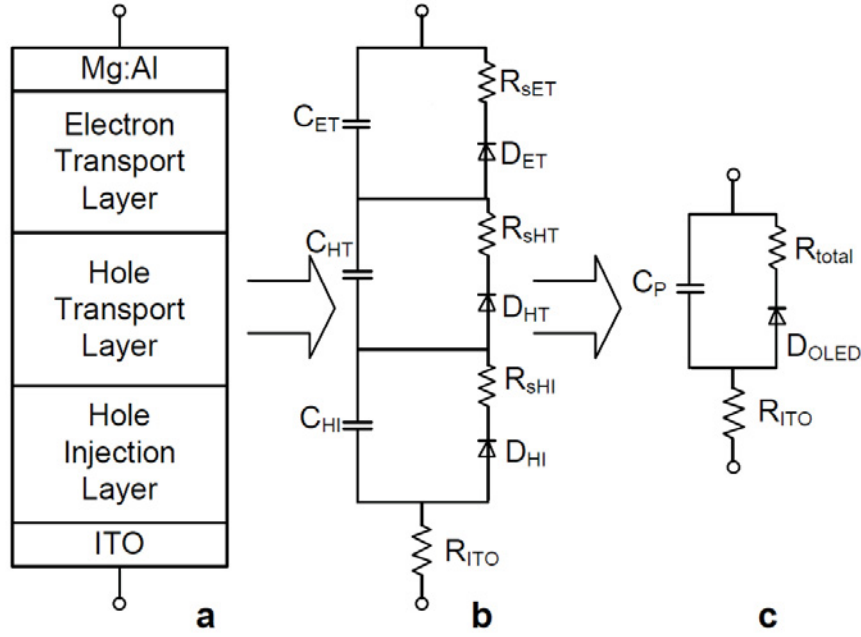


Figure 3.1: Simplified OLED model (adapted from [3] and [24])

polymer OLED display were all determined in a specific manner depending on their nature.

For the sheet resistance of the ITO anode and metallic cathode, values obtained in a preceding work were used [32]. They were determined by measuring the resistance of an entire row and column and dividing them by the number of columns and rows respectively. This operation was most likely carried out in an invasive manner. The anode resistance per pixel is set at $R_{ITO} \approx 100 \Omega$ and the row resistance at $R_{row} \approx 50 m\Omega$.

If the sheet thickness is known, generic values from literature could be used [36]. Given the square shape of the pixels, the anode resistance per pixel is given directly by $R_{ITO,\square}$. The cathode sheet resistance $R_{metal,\square}$ can be obtained by dividing the bulk resistance ρ_{metal} by the sheet thickness.

The diode coefficients and the bulk series resistance on one hand and the parallel pixel capacitance on the other were extracted from characterisation measurements using different methods.

3.1.1 The Diode

To characterise the diode, an arbitrary pixel was stimulated with DC voltages (V_{drive}) from 0 V to 7 V in increments of 0.1 V and the diode current was recorded. To this end the tool ICCAP was used with wafer-probes connected to one anode and one cathode respectively. With this setup, the cumulative anode ITO resistance and cathode metal resistance are part of the measurement path and thus bias to some extent the result. Given the fact that their value is some orders of magnitude smaller than the diode series resistance, this bias is considered negligible.

The Matlab curve fitting tool *cftool* was then used to produce the diode equation coefficients and the value of the series resistance using the least square fitting method. The conventional diode current-voltage relation

$$i_D = i_s \cdot (e^{\frac{V_D}{N \cdot V_T}} - 1) \quad (3.1)$$

with $V_T \approx 25.8 \text{ mV}$ at 25°C , was solved for V_D and together with the voltage drop over the series resistance led to the custom equation to fit

$$V_{drive} = i_{d,meas} \cdot R_s + N \cdot 0.025 \cdot \ln\left(\frac{i_{d,meas}}{i_s} + 1\right) \quad (3.2)$$

The outcome of the fitting process are: saturation current $i_s = 4.934 \text{ nA}$, emission coefficient $N = 17.83$, serial resistance $R_s = 5111 \Omega$. Figure 3.2 shows the fitting output menu including the fit goodness and a plot with the measured response versus the fitted one. The result has been considered sufficiently precise for the purpose of this work and the parameters have been transferred to the PSpice model as described further.

3.1.2 The Pixel Capacitance

Three methods have been used to determine the pixel capacitance.

A simple and straight-forward way is to use a conventional multimeter or a C-V meter to measure the capacitance between shorted anodes and shorted cathodes and divide it by the number of pixels. The obtained value is $C_{p,multimeter} \approx 78 \text{ pF}$.

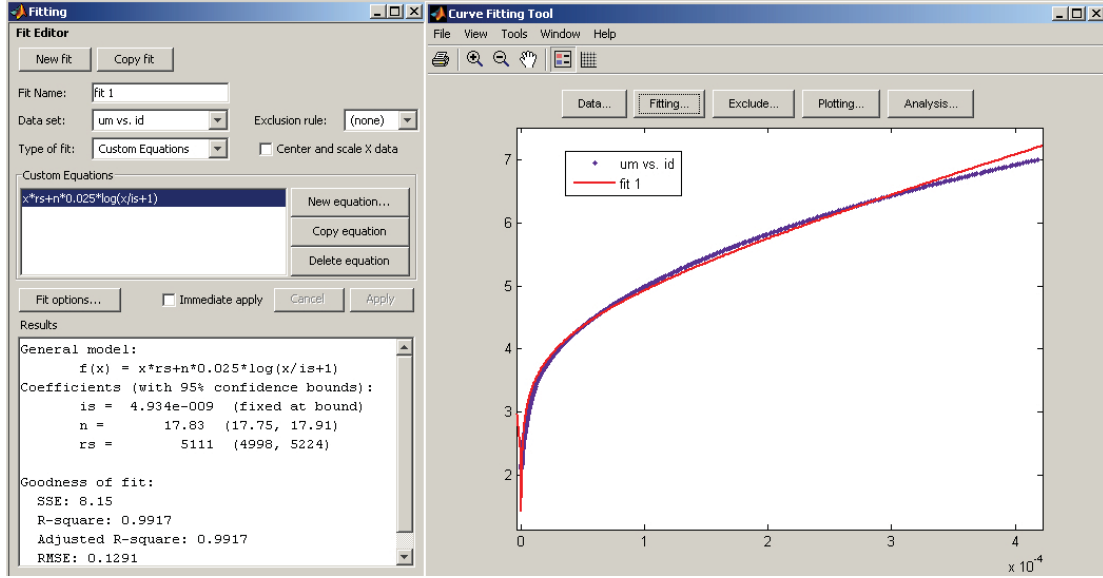


Figure 3.2: Curve fitting in Matlab to determine OLED (diode) coefficients. Fitting settings and fitted response (red) vs. measurements (blue)

A further method makes use of the fundamental SQC equation (4.13) describing the state dependence discussed in detail in section 4.3. It is used in conjunction with the characterisation measurements described in section 5.2.2 and outlined in table 5.1. The measured parameters are the luminance current of the photodiode, the final voltage at the end of the row addressing time, the peak voltage at the end of the injection phase, the cumulative supply current of the constant current sources and the cumulative discharge current, taken for all combinations of injection times (bit-values from 0 to 31) and initial voltages in several discrete steps from 0 V to 7.5 V. In this context the relevant measurements have the initial voltage set at $V_{col,i} = 0 V$ and run through lower bit-values when no light is produced, i.e. $I_{photo} = 0 nA$. It means that the cumulative capacitance is charged below the threshold voltage level of the OLEDs. Equation 4.13 is then simplified and solved for the pixel capacitance:

$$C_p = \frac{I_{inj} \cdot t_{inj}}{N_{row} \cdot V_{col,i+1}} \quad (3.3)$$

Once the sensing amplification factor k is determined (section 3.1.3), the above mentioned method can be extended to the generic case of light producing pixels. Solving the equation for C leads to:

$$C_p = \frac{I_{inj} \cdot t_{inj} - k \cdot I_{Lum}}{N_{row} \cdot (V_{col,i+1} - V_{col,i})} \quad (3.4)$$

Both the simplified and the generic case are yielding a pixel capacitance value of $C_{p,SQC} \approx 72 \text{ pF}$.

The last method accounts for the fact that the capacitive power dissipation is reflected in the discharge current (section 3.4). In consequence, the relation between the pixel voltage at the end of the row addressing time and the initial voltage of the next pixel $V_{set} = V_{dis}$ can be described as:

$$N_{row} \cdot C_p \cdot (V_{col,i+1} - V_{dis}) = \frac{I_{dis} \cdot t_{row}}{N_{col}} \quad (3.5)$$

This can be solved for the capacitance as all other parameters are measured. The method produces a pixel capacitance $C_{p,SQC,dis} \approx 80 \text{ pF}$.

All these methods deliver similar pixel capacitance values. The simplified SQC equation-based method is supported by the highest number of data points, therefore the value of $C_p \approx 72 \text{ pF}$ is employed in the OLED model.

The extracted diode coefficients (i_s and N) are transferred to the generic PSpice diode model and all remaining parameters are left at default value. The bulk series resistance R_s and the parallel pixel capacitance $C_d = C_p$ were added as separate model parts, as depicted in figure 3.3. This shows the lower level model and the upper level four-terminal symbol that allows matrix-wise embedding. The shunt resistance R_{ak} is used for current probing only and has no physical meaning.

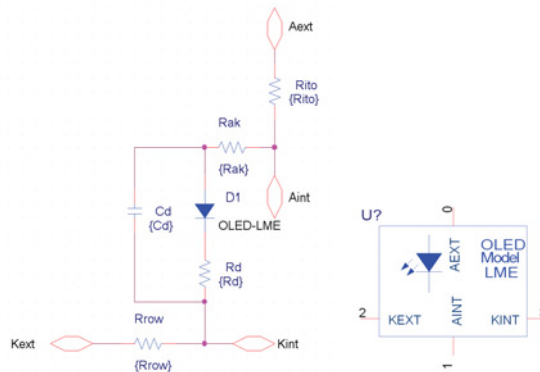


Figure 3.3: OLED model and symbol in PSpice

3.1 OLED Display Modelling and Characterisation

Figure 3.4 shows a generic schematic of an OLED display using the models described above. Figure 3.5 shows a 4 x 4 display example modelled in PSpice.

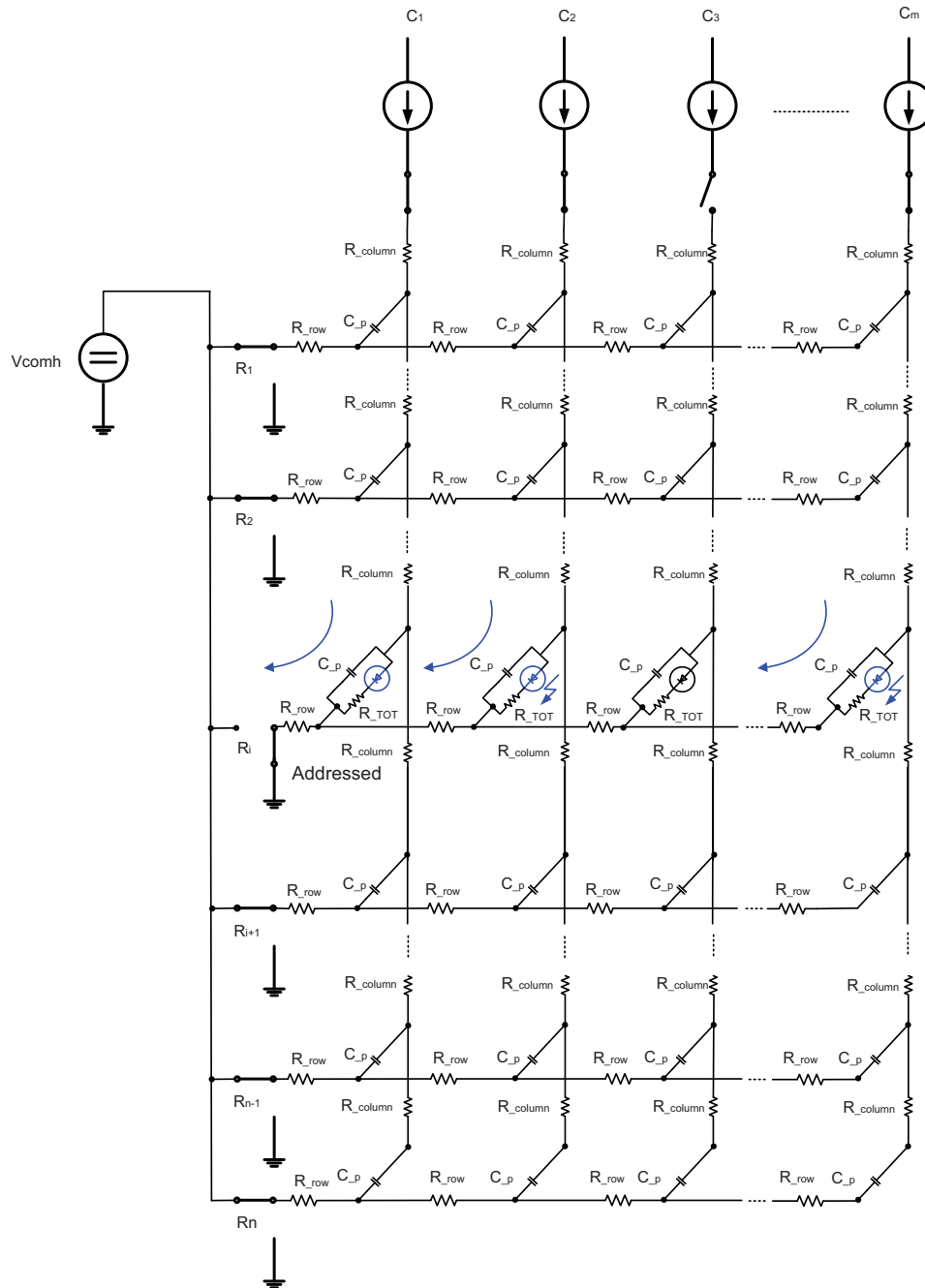


Figure 3.4: Generic OLED display schematic

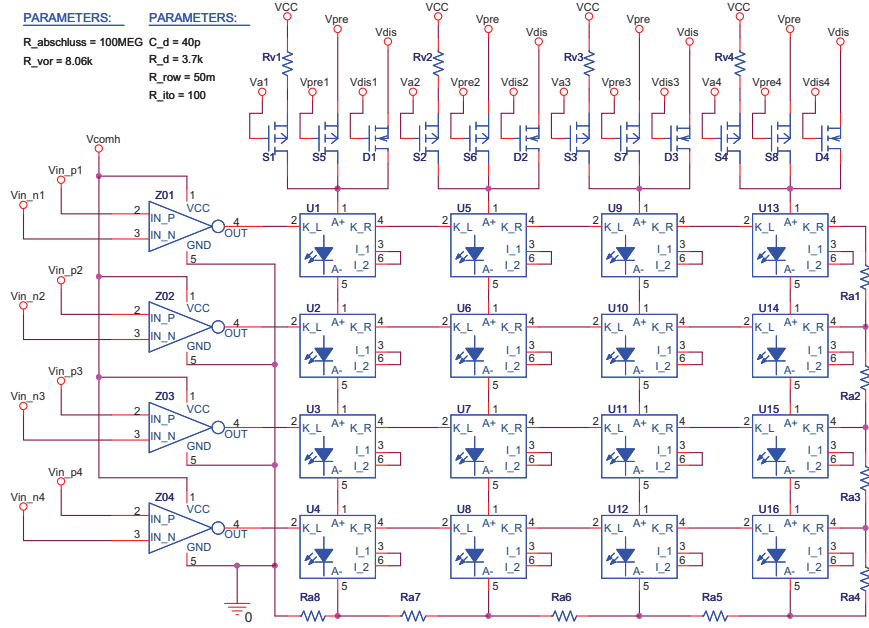


Figure 3.5: 4 x 4 OLED display schematic in PSpice (adapted from [4])

3.1.3 The Sensing Amplification Factor k

Another parameter of relevance in the SQC implementation is the amplification factor k present in equation 3.4 and later on in equation 4.13. It describes the ratio between the electrical charge converted into light by the OLED pixel and the luminance sensed with the measurement equipment consisting of a photodetector (figure 3.6) and an averaging picoammeter during the display characterisation process.

k is defined as:

$$k \left[\frac{1}{s} \right] = \frac{I_{Photo} [A]}{Q_{inj} [A \cdot s]} = \frac{I_{Photo} [A]}{I_{inj} [A] \cdot t_{inj} [s]} \quad (3.6)$$

k can be broken down into different components:

$$k = N_{pixels} \cdot \eta_{OLED} \cdot k_{Photo} \quad (3.7)$$

For characterisation measurements all pixels have been driven with the same waveform to ensure a proper measurable photocurrent and to even out potential

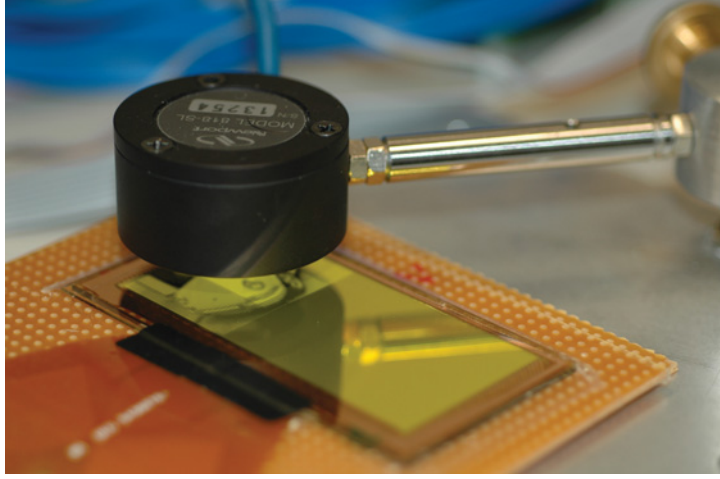


Figure 3.6: Photodiode and the OLED display under test

inhomogeneities. N_{pixels} is the number of pixels captured and physically covered by the photodetector. η_{OLED} is the OLED luminous efficiency described in section 3.2 and k_{Photo} is the amplification factor of the photodetector itself which produces an output current proportional to the incident light. η_{OLED} is constant due to the constant injection current used in all presented experiments. The photodetector has been always placed over the same display area, thus N_{pixels} is also constant. The photocurrent is a linear function of the optical power [56], thus k_{Photo} is also constant. In conclusion, k is expected to be constant. This fact has been confirmed by experiments with a constant frame rate. Nevertheless, as the picoammeter displays the average photocurrent in a similar manner to the human eye, this amplification factor is frame rate dependent. The following relation has been derived:

$$\frac{1}{k_{f_{frame}}} \approx \frac{1}{k_{f_{frame,ref}}} \cdot \frac{f_{frame,ref}}{f_{frame}} \quad (3.8)$$

As an example, $\frac{1}{k_{100\text{ Hz}}} \approx 1.5\text{ ms}$ and $\frac{1}{k_{25\text{ Hz}}} \approx 6\text{ ms}$.

A method to determine the amplification factor is to perform characterisation measurements without discharging the cumulative capacitance and to record the photocurrent for different injection times, i.e. bit-values. The consequence is that for each pixel, the initial state equals the final state, i.e. $V_{col,i} = V_{col,i+1}$ and k can be computed using equation 4.13 as:

$$k = \frac{I_{Photo}}{I_{inj} \cdot t_{inj}} \quad (3.9)$$

If the pixel capacitance is known upfront, i.e. by measuring it with a multimeter as described above, k can be also extracted from the generic characterisation measurements (table 5.1) using the formula:

$$k = \frac{I_{Photo}}{N_{row} \cdot C_p \cdot (V_{col,i} - V_{col,i+1}) + I_{inj} \cdot t_{inj}} \quad (3.10)$$

3.2 OLED Luminous Efficiency

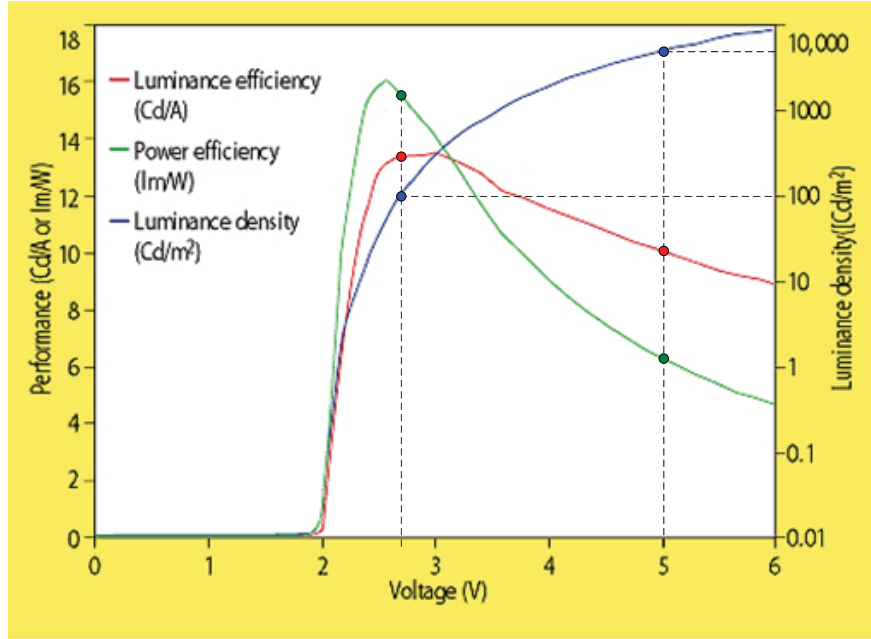
One of the key measures of OLED performance is the luminous efficiency [27]. It can be measured in candelas per ampere (cd/A), often denoted as luminance efficiency reflecting the light output for a given current, or in lumen per watt (lm/W), denoted as power efficiency which quantifies the light output per power input as used in lighting.

The luminous efficiency of OLEDs is not constant. It is a function of the driving voltage and in turn of the OLED recombination current. Figure 3.7 depicts an example from literature that shows the luminance and power efficiency decay as a function of the driving voltage.

This dependency is particularly relevant for passive-matrix OLED displays as they are driven in a time-multiplexed manner. The nominal frame luminance perceived by the human eye by means of time-averaging (integration) needs multiplication by the number of rows to define the nominal physical luminance per pixel.

As an example with data from figure 3.7, if a 50-row display needs to produce per frame a given luminance density of 100 cd/m^2 , the individual pixel needs to deliver 5000 cd/m^2 . As illustrated in figure 3.7, this implies in turn a decay of luminous efficiency of about 25% and of power efficiency of about 60%.

This effect gives a strong incentive to reduce the amplitude of the OLED injection current. It can be accomplished by means of flattened singleline addressing (FSLA), multiline addressing (MLA) (section 2.3.2) or discharge at threshold voltage level (section 4.1.1). In the present work a PWM control method with constant current is applied. For this reason, the luminous efficiency is not affected.



1. Representative OLED luminescent-current-voltage (LIV) characteristics depict typical display performance. The luminance efficiency and the power efficiency are optimized at slightly below 3 V. (Courtesy of Germany's Covion Organic Semiconductors GmbH)

Figure 3.7: OLED luminous efficiency (adapted from [27])

3.3 Resistive Power Loss

The resistive power loss in OLED displays has been investigated in [6] and an algorithm has been developed to extensively reduce the resistive power dissipation in the conducting cathodes. The innovative principle is to spread the cathode current load over the row addressing time to flatten the current profile and reduce the peak amplitudes. The resistive power loss is thus diminished as it is a square function of the current.

The average power dissipated in a resistor during the frame period T_{frame} is

$$P_{res} = \frac{\int_{t_1}^{t_2} U(t) \cdot I(t)}{T_{frame}} = \frac{\int_{t_1}^{t_2} I^2(t) \cdot R}{T_{frame}} \quad (3.11)$$

With a constant current of amplitude I_0 and $\Delta t = t_2 - t_1$, equation 3.11 becomes

$$P_{res} = I_0^2 \cdot R \cdot \frac{\Delta t}{T_{frame}} \quad (3.12)$$

3 Power Consumption in PMOLED Displays

For each pixel, the duration of the constant current injection phase is a product of its digital grey-value $A(i, j)$ and the time increment t_{lsb} .

$$t_{inj}(i, j) = A(i, j) \cdot t_{lsb} \quad (3.13)$$

For this reason, the time resolution of the following approach is $\Delta t = t_{lsb}$. The ratio $\frac{t_{lsb}}{T_{frame}}$ becomes thus a constant in the following equations.

The sheet resistors responsible for power dissipation are the unit anode ITO resistance R_{ITO} and the cathode metallic resistance R_{row} that are part of each pixel (figure 3.4). For this reason the resistive power loss is composed of two parts, one generated by the currents flowing into the OLEDs through the anode trace resistance and one by the currents coming out of the OLEDs that sum up in the active row and flow to ground:

$$P_{res} = P_{res,anodes} + P_{res,cathodes} \quad (3.14)$$

The quantitative assessment of the two components needs to be carried out separately. The series resistance of the diode is not comprised in this model as it is considered part of the diode itself. It is expected to be reflected in the luminous efficiency.

3.3.1 Resistive Power Loss in the Anodes

The current flowing into each pixel passes through all preceding ITO resistors within the addressed anode (figure 3.4). In consequence, its share in the resistive power loss is multiplied by the row number. The cumulative anode resistive power loss becomes:

$$P_{res,anodes} = I_0^2 \cdot R_{ITO} \cdot \frac{t_{lsb}}{T_{frame}} \cdot \sum_{j=1}^{N_{col}} \cdot \sum_{i=1}^{N_{row}} A(i, j) \cdot i \quad (3.15)$$

It is proportional to the overall luminance of the image displayed.

3.3.2 Resistive Power Loss in the Cathodes

Quantifying the cathode resistive power loss is more difficult due to the fact that in each node of a cathode, the current is varying during the row addressing time, depending on how many constant current sources are active at a given moment. This is illustrated in figure 3.8 by the current waveforms of various widths, partially overlapping in time.

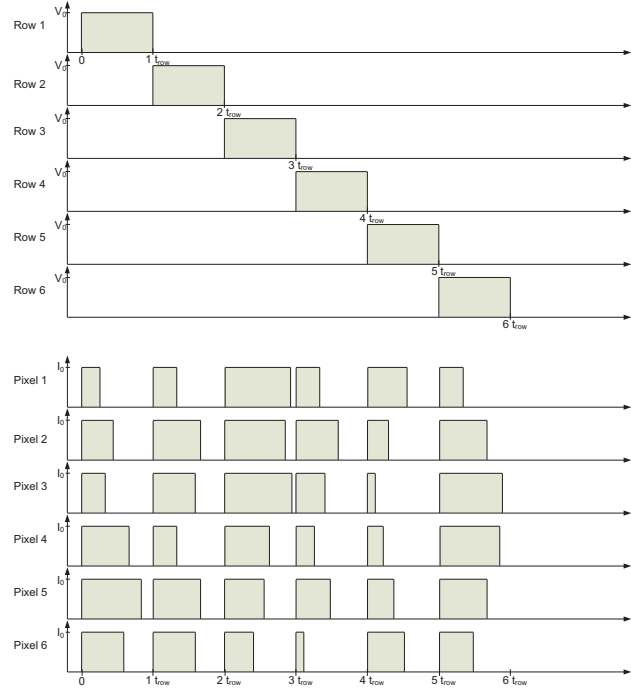


Figure 3.8: OLED conventional driving example (adapted from [6])

The sequence of different cathode current amplitudes during the row addressing time is depicted in figure 3.9 for three pixels in a row of a 3-bit system having the grey-values of 4, 7 and 2.

Time slot	Pixel 1	Pixel 2	Pixel 3
$0..2 t_{lsb}$	2	2	2
$2..4 t_{lsb}$	2	2	0
$4..7 t_{lsb}$	0	3	0
<i>Total</i>	4	7	2

Table 3.1: Time slots corresponding to the driving sequence depicted in figure 3.9

3 Power Consumption in PMOLED Displays

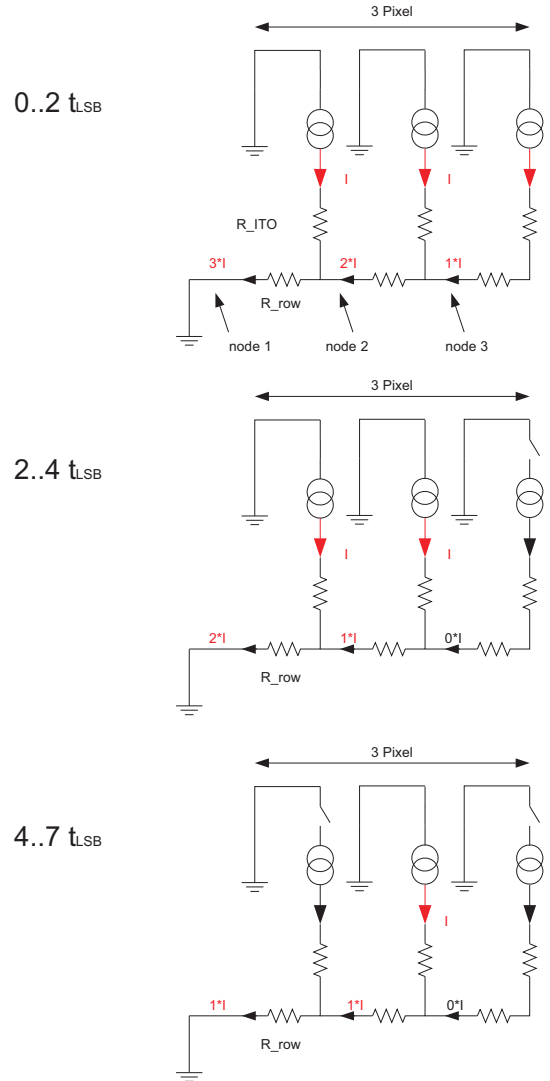


Figure 3.9: Example of cathode currents within one row during the row addressing sequence (adapted from [6])

To illustrate the timing decomposition made to quantify the resistive power loss, table 3.1 captures the three consecutive time slots in the addressing of each pixel. The individual t_{lsb} multipliers represent the active time.

As the power loss is proportional to the square of the current amplitude, the share of each resistor cannot contribute linearly to the cumulative power loss. Instead, each individual I_{row}^2 -component needs to be added separately. To formalise this approach, the power loss needs bitwise quantification. It is computed for each t_{lsb} increment, as follows:

For each row i a bit matrix M_i is constructed from the grey-value matrix $A(i, j)$, with $0 < A(i, j) < 2^q - 1$. It indicates the active anodes for each bitwise time increment.

$$M_i(\text{bit}, j) = \begin{cases} 1 & \text{if } A(i, j) \geq \text{bit} \\ \text{else } 0 & \end{cases} \quad (3.16)$$

$$\text{bit} = 1 \dots (2^q - 1)$$

$$j = 1 \dots N_{col}$$

For the above example, matrix M is shown in table 3.2.

Out of matrix M_i , the sum-matrix S_i is constructed so that for each position in a row the sum of all bits to its right, including itself, is calculated:

$$S_i(\text{bit}, j) = \sum_{k=j}^{N_{col}} M_i(\text{bit}, k) \quad (3.17)$$

At last, the matrix S_i^2 is computed, in which each element is the square of the equivalent in S_i :

$$S_i^2(\text{bit}, j) = (S_i(\text{bit}, j))^2 \quad (3.18)$$

For the above example, the matrices S_i and S_i^2 are also shown in table 3.2.

M	4	7	2	S	4	7	2	S^2	4	7	2
1	1	1	1	1	3	2	1	1	9	4	1
2	1	1	1	2	3	2	1	2	9	4	1
3	1	1	0	3	2	1	0	3	4	1	0
4	1	1	0	4	2	1	0	4	4	1	0
5	0	1	0	5	1	1	0	5	1	1	0
6	0	1	0	6	1	1	0	6	1	1	0
7	0	1	0	7	1	1	0	7	1	1	0

Table 3.2: Bit-matrices M , S and S^2 for a three-pixel example

The cumulative cathode resistive power loss becomes:

$$P_{res,cathodes} = I_0^2 \cdot R_{row} \cdot \frac{t_{lsb}}{T_{frame}} \cdot \sum_{i=1}^{N_{row}} \sum_{bit=1}^{2^q-1} \sum_{j=1}^{N_{col}} S_i^2(bit, j) \quad (3.19)$$

In the given example, this sums up for one row to

$$P_{res,cathodes,example} = 44 \cdot I_0^2 \cdot R_{row} \cdot \frac{t_{lsb}}{T_{frame}} \quad (3.20)$$

The above reasoning relies on the assumption that the OLED current is constant and flows only through the activated diodes and the selected row. However, as described in the next sections, the OLED current may have an injection and a capacitive component. The latter is a displacement current that flows through the parasitic pixel capacitances and the idle rows. This induces a certain systematic error in the above calculation, in particular as the current has a quadratic contribution to the resistive power loss and its components cannot be simply added together.

The driving scheme developed as part of this thesis mainly aims to reduce the capacitive power loss. Nevertheless, it is expected to reduce the resistive power loss as well as the average current flowing into the PMOLED display gets lower.

3.4 Capacitive Power Loss

A conventional driving sequence consists of three phases: precharge, constant current and discharge [57] - [68] (section 2.3). The OLED capacitances are precharged - usually by applying a constant voltage slightly below the forward voltage of the diodes - to allow for an immediate emission of light once the constant drive current is applied. As soon as the desired luminance is reached, the current source is deactivated and the anode is switched to ground. Any parallel OLED capacitance is thus discharged and the OLED stops emitting light. The light emission is nearly proportional to the activation time of the current source. This duration can be easily and accurately controlled in hardware by means of pulse-width modulation.

The common cathodes are consecutively scanned. The addressed row is grounded and the idle rows are switched to a common voltage V_{comh} to avoid crosstalk. This fact provides the basis for simplifying the equivalent circuit as follows:

3 Power Consumption in PMOLED Displays

sponding to the OLED current converted into light is referred as P_{lum} . Power is dissipated in the discharge switch and is denoted as P_{dis} . The power balance over a certain period, e.g. the frame period, can be thus expressed as:

$$P_{inj} + P_{comh} = P_{lum} + P_{dis} \quad (3.22)$$

During the constant current driving phase, the injected current is shared between the cumulative capacitance of the idle rows C_{eq} and the addressed OLED pixel (figure 3.10).

$$I_{inj}(t) = I_{cap}(t) + I_{OLED}(t) \quad (3.23)$$

The capacitive current initially flows from the current injection source into the common voltage source V_{comh} , lifting the anode potential from ground to a value V_{col} less or equal to the forward voltage of the OLED. This starts emitting light as soon as the anode potential exceeds the value of its threshold voltage V_{th} . During the discharge phase, the capacitive current flows back from the common source V_{comh} to ground and the anode potential is abruptly dropped (figure 3.11):

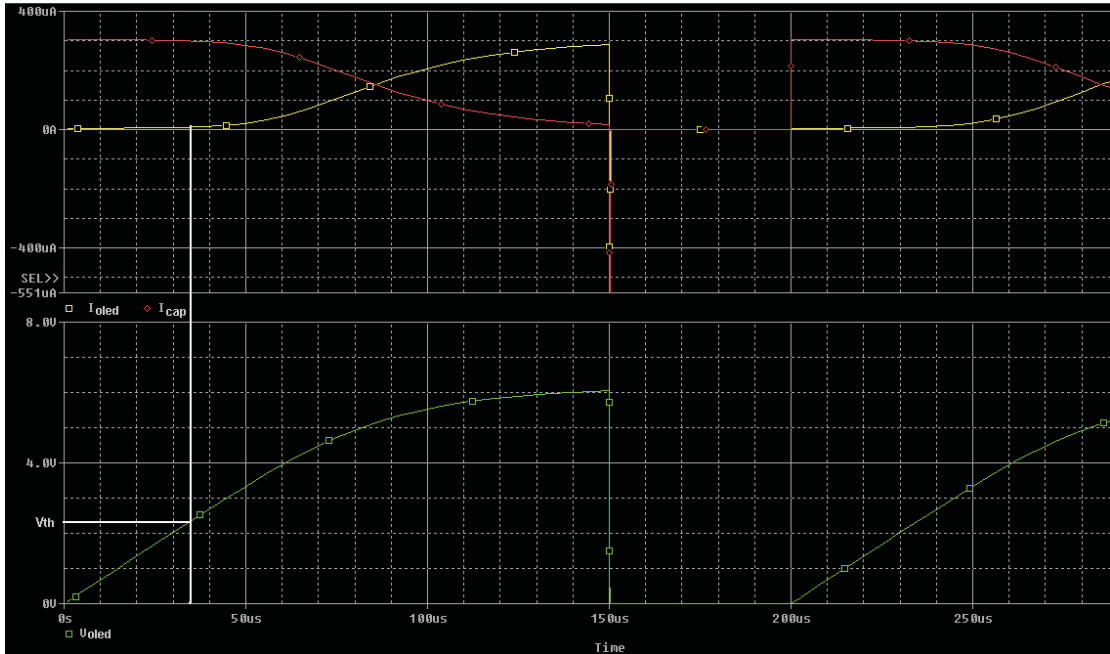


Figure 3.11: OLED pixel current and voltage waveforms

The energy wasted during the discharge phase is supplied by the constant current source and is only buffered by V_{comh} . Power is drawn from V_{comh} only when the next addressed pixel (row) is switched to ground. This capacitive power loss P_{comh} is due to a single pixel capacitance C_p and is thus negligible compared to the discharge power loss P_{comh} caused by the cumulative pixel capacitance C_{eq} . Hence, equation 3.22 can be simplified to:

$$P_{inj} \approx P_{lum} + P_{dis} \quad (3.24)$$

According to equation 3.24, the capacitive power loss in a PMOLED display matrix is P_{dis} : the power actively injected into the cumulative capacitance of the idle rows C_{eq} and dissipated by the discharge switch. It is also further denoted as P_{cap} .

The average power dissipation of one pixel $P_{dis_{ij}}$ is proportional to the charge ΔQ_{cap} that flows into the idle capacitance during the row addressing time t_{row} :

$$P_{dis_{ij}} \sim \int_0^{t_{row}} I_{cap}(t) \cdot dt = \Delta Q_{cap} \quad (3.25)$$

$$\Delta Q_{cap} = C_{eq} \cdot V_{col} \quad (3.26)$$

The overall power dissipation is thus a square function of the number of rows - at a constant frame rate and a constant pixel size.

$$P_{cap} = P_{dis} \sim \sum_{i=1}^{N_{row}} \sum_{j=1}^{N_{col}} N_{row} \cdot C_p \cdot V_{col_{ij}} \quad (3.27)$$

$$P_{cap} \sim N_{row}^2 \quad (3.28)$$

Due to this square dependency and the fact that C_p increases with newer technologies, as the OLED layers are getting thinner, the capacitive power loss dominates the power consumption of large PMOLED displays.

3.5 Numerical Example and Conclusions

To find out the order of magnitude and compare the different sources of power loss in an OLED display, a numerical example is given for several displays of the same kind but with different resolutions. The reference is the available 128 x 64 polymer

3 Power Consumption in PMOLED Displays

OLED display with extracted parameters as described in section 3.1. To observe the impact of the display size, the resolution is then artificially increased to 160 x 120, 320 x 240 and 640 x 480. The power consumption is image dependent. To simplify the application of the derived formulas, a uniform reference test pattern with all pixels at half-scale brightness is used. When determining the resistive power loss, ideal rectangular current waveforms are considered.

The set parameters are:

$$I_0 = 310 \mu A$$

$$V_{col} = 7 V$$

$$f_{frame} = 100 Hz$$

$$T_{frame} = 10 ms$$

$$t_{inj} = \frac{t_{row}}{2}$$

$$R_{ITO} = 100 \Omega$$

$$R_{row} = 50 m\Omega$$

$$C_p = 72 pF$$

$$C_{eq} = N_{row} \cdot C_p$$

With $\frac{t_{inj}}{T_{frame}} = \frac{1}{2 \cdot N_{row}}$, the following simplified formulas can be used:

$$P_{lum,ex} = \sum_j^{N_{col}} \sum_i^{N_{row}} I_0 \cdot V_{col} \cdot \frac{t_{inj}}{T_{frame}} = I_0 \cdot V_{col} \cdot \frac{N_{col}}{2} \quad (3.29)$$

$$P_{res,anodes,ex} = I_0^2 \cdot R_{ITO} \cdot \frac{t_{inj}}{T_{frame}} \cdot \sum_j^{N_{col}} \sum_i^{N_{row}} i = I_0^2 \cdot R_{ITO} \cdot \frac{N_{col} \cdot (N_{row} + 1)}{4} \quad (3.30)$$

$$P_{res,cathodes,ex} = I_0^2 \cdot R_{col} \cdot \frac{t_{inj}}{T_{frame}} \cdot \sum_i^{N_{row}} \sum_j^{N_{col}} j^2 = I_0^2 \cdot R_{row} \cdot \frac{N_{col} \cdot (N_{col} + 1) \cdot (2 \cdot N_{col} + 1)}{12} \quad (3.31)$$

$$P_{cap,ex} = \sum_j^{N_{col}} \sum_i^{N_{row}} \frac{N_{row} \cdot C_p \cdot V_{col}^2}{2 \cdot T_{frame}} = N_{col} \cdot N_{row}^2 \cdot C_p \cdot V_{col}^2 \cdot \frac{1}{2 \cdot T_{frame}} \quad (3.32)$$

N_{col}	N_{row}	$P_{lum}(mW)$	$P_{R,col}(mW)$	$P_{R,row}(mW)$	$P_{cap}(mW)$	$P_{tot}(mW)$	$P_{cap}(\%)$
96	64	104	15	0.7	69	189	37
160	120	174	47	3	406	630	65
320	240	347	185	26	3251	3810	85
640	480	694	740	210	26011	27656	94

Table 3.3: Power budget simulation for different display resolutions

The computation results for the four resolutions are recorded in table 3.3. They demonstrate the very large share of capacitive power loss in the overall power budget of the display and that this is dominant at higher resolutions.

G. Landsburg quantifies and confirms in [42] the contribution of the capacitive power loss to the overall power budget of a PMOLED display. Figure 3.12 shows his numerical example for a 120 x 240 display considering also the consumption of the driver itself. It can also be seen that 8% of the power is used by the driver logic and 26% by the constant current sources.

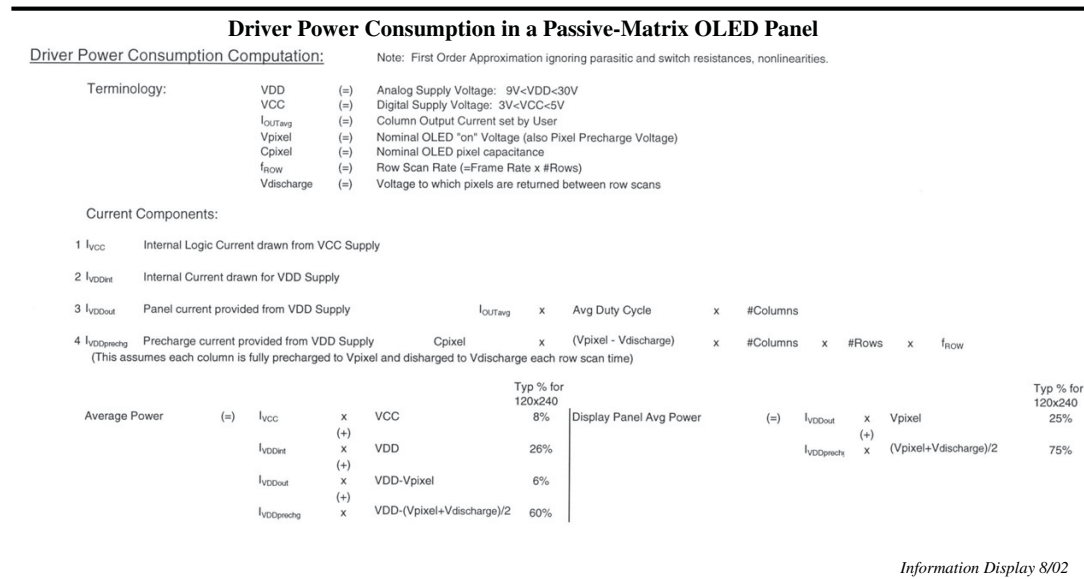


Figure 3.12: Power consumption in a PMOLED display module [[42]]

In conclusion, it has been shown that the capacitive power loss dominates the power consumption of large PMOLED displays and grows rapidly with the number of rows. Even though capacitors only store energy and do not consume or dissipate any power, energy is lost during charging and discharging the OLED capacitive

3 Power Consumption in PMOLED Displays

matrix and is dissipated in the control transistors of the current sources and the discharge switches. If the discharging process could be avoided, e.g. by reusing the stored charge, this capacitive power loss could be avoided or significantly reduced. For this reason the purpose of this thesis is to drastically reduce the capacitive power loss. To this end, a new driving method is introduced in the next chapter.

4 The Principle of State-dependent Charge-controlled (SQC) Driving

This chapter describes the basic principle of the state-dependent charge-controlled (SQC) driving concept. It is conceived to reduce considerably the power consumption of PMOLED display modules by nearly eliminating the capacitive power loss. The theory is preceded by a short description of conventional driving and the introduction of post-luminescence as consequence of high-impedance driving, one of the principles behind SQC.

4.1 Conventional Driving Scheme

Conventional PMOLED driving has been already briefly illustrated in chapter 2 and 3. Figure 4.1 depicts the schematic of a PMOLED display with m rows (cathodes) and n columns (anodes). Each of the cathodes is connected to a cathode driver that lifts it to a constant positive voltage or switches it to ground acting as a current sink. Each anode is connected to a current source and can be either in constant current mode or floating (high-impedance). If it is connected to a constant voltage source it can also be switched to ground.

The cathodes are sequentially scanned, i.e. one at a time is switched to ground. The active anode sources are injecting current all at once during the row addressing time. The eye integrates the emitted light in each pixel and a still, averaged image can be perceived provided that the rows are scanned sufficiently fast. The human visual system can record 10-12 images per second. It perceives everything displayed with a higher frame frequency as a motion image (video) or a still image if the frame content does not change. Even though movies have been traditionally projected at 24 frames per second, flicker may be observed at even higher frame rates, especially if the image content changes abruptly. For this reason displays

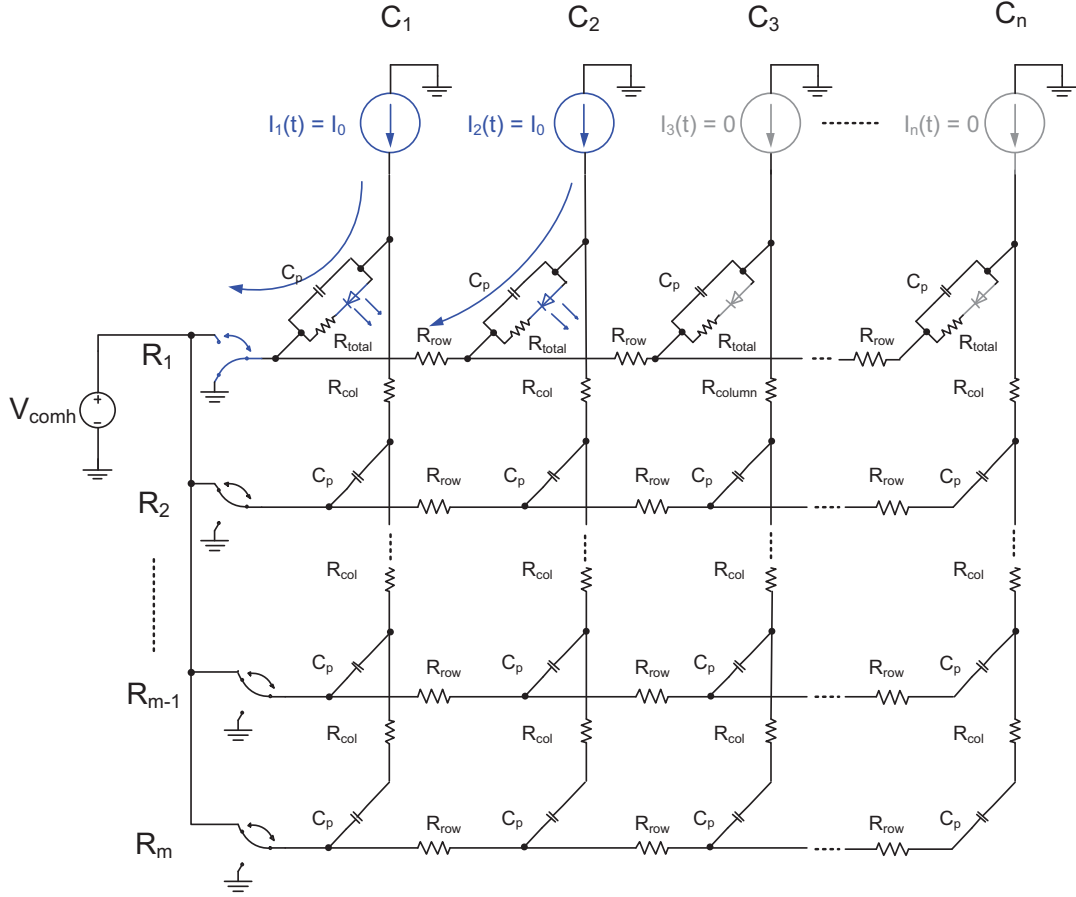


Figure 4.1: PMOLED display schematic (adapted from [88], [6], [24])

often use in practice a frame rate around 100 Hz . The duration of each frame is then:

$$t_{frame} = \frac{1}{100\text{ Hz}} = 10\text{ ms} \quad (4.1)$$

When driving a display with 64 rows, the row addressing time is:

$$t_{row} = \frac{10\text{ ms}}{64} \approx 156\text{ }\mu\text{s} \quad (4.2)$$

These parameters are used as reference in this work for the implementation of driving schemes. Each pixel brightness (grey-value) needs to be reflected during the row addressing time and the charge converted into light must be large enough to produce the desired average luminance over a frame period.

In figure 4.1 the first two pixels of the first row are driven to emit light. During the row addressing time, the cathodes of the selected OLED pixels are switched to ground and the current flowing into the anodes produces light. The light amplitude is nearly proportional to the current amplitude and the injection time of the corresponding current source.

$$Lum = k \cdot Q_{lum} = k \cdot \int_0^{t_{row}} I_{OLED}(t) \cdot dt \approx k \cdot I_{OLED} \cdot t_{inj} \quad (4.3)$$

The remaining cathodes are lifted to a common potential V_{comh} which is slightly below the forward voltage of the diodes. In this way all inactive diodes are reverse biased and do not emit light. Equation 4.3 provides the basis for controlling the light emission of pixels. The intensity is set by adjusting the current amplitude or the duration of each pulse. Adjustable and sufficiently precise current sources are expensive and difficult to realise in hardware. The convenient method is pulse-width modulation with a constant current amplitude as the duration of the current injection is easily programmable. A grey-value i with $0 < i < 2^{q-1}$ can be realised by adjusting the duty cycle of the constant current source, with 0 corresponding to the lower limit (black) and 2^{q-1} to the upper one (white):

$$Lum \sim duty\ cycle = \frac{t_{inj}}{t_{row}} = \frac{i \cdot t_{lsb}}{t_{row}} \quad (4.4)$$

t_{inj} is the duration of the constant current phase (injection time) and t_{lsb} is the time increment needed to modify the pixel brightness by one grey unit:

$$t_{lsb} = \frac{t_{row}}{2^{q-1}} \quad (4.5)$$

Figure 4.2 exemplifies the addressing sequence corresponding to a simple 2 x 2 luminance matrix (4.2a). The visual result is depicted in 4.2b. The cathode driver signals are shown in 4.2c and the anodes driver signals in 4.2d [24]. A logic *high* means constant current mode for the driven anode and ground potential for the addressed cathode respectively.

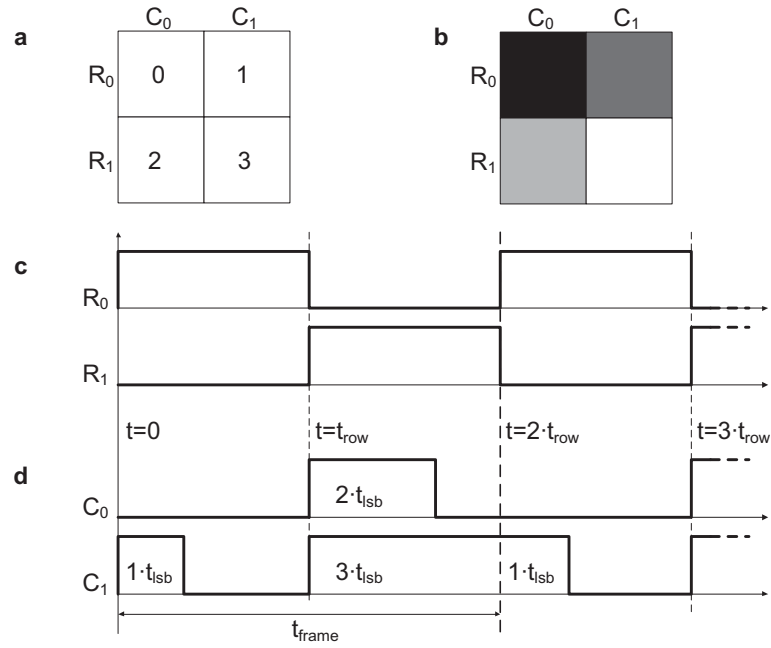


Figure 4.2: OLED conventional addressing (adapted from [24])

4.1.1 Precharge and Discharge

Ideally, the OLED pixel current waveform is rectangular in shape, following the control signals depicted in 4.2d and allowing for an adjustment of the duty cycle according to equation 4.3 and 4.4. Figure 3.11 shows however that both the rising and falling current edges are not abrupt. The reason is the non-negligible cumulative column capacitance C_{eq} that demands a share of the injection current and can deliver the stored charge to an OLED when this is not supplied by a constant current source.

The simulation depicted in figure 3.11 shows that the diode is practically not conducting for the time corresponding to $V_{OLED} < V_{th}$ and is thus not emitting light. To shorten this idle period a precharge phase is introduced in conventional drivers (section 2.3). The precharge source can be a current source with a higher amplitude activated until the anode potential rises to the forward voltage level or a constant voltage source $V_{pre} = V_{th}$ that lifts the anode potential abruptly depending on its current sourcing capability. Voltage or current precharge allows for an immediate emission of light once the precharge phase is completed.

At the end of the constant current injection time, the cumulative capacitance would supply further current to the active pixel and the anode voltage would

drop as shown in figure 5.3b). At the end of this *parasitic* light emission, the anode potential would drop to an unknown value which would become the initial voltage for the next row in the addressing sequence. In conventional driving, this undefined state is eliminated by switching the anode to ground once the injection phase is completed. Using this discharge phase, the falling current edge is abrupt and the anode voltage is de-facto reset. The light emitted during the discharge phase is zero and the duration of the the precharge and discharge phases is small with respect to the injection time. Thus the pixel luminance is nearly linear to the activation time of the current source and the grey-value can be easily met with sufficient precision. The image quality is assured, however at the cost of energy dissipation, as illustrated in section 3.4.

A first effective approach to reduce this capacitive power loss is to discharge the anodes to a higher potential slightly below the threshold voltage of the diodes ($V_{dis} \approx V_{th}$) instead of ground. By doing this, less energy is wasted in the discharge switch and the anodes are also to some extent implicitly precharged for the next row addressing sequence. As the OLEDs start emitting light faster when implicitly precharged, for the same injection time more light is produced than in conventional driving with $V_{dis} = 0V$. Figure 4.3 shows the two transfer curves $Lum = f(t_{inj})$ for conventional driving with discharge at $0V$, and with discharge at a threshold voltage level $V_{dis} = 2.5V$.

To compare quantitatively the two cases, the picture brightness is kept constant and the current consumption is measured. For the comparison to be consistent when using the same row addressing time, the constant current amplitude needs to be increased in this example from $330\mu A$ when discharging at $2.5V$ to $415\mu A$ when discharging at $0V$. In this manner the full-scale injection time generates the same brightness. Figure 4.3 shows the transfer curve for the two cases and illustrates the shorter injection time for the same brightness if discharge is performed at threshold voltage level. Furthermore, figure 4.4 shows the power saving percentage for the entire luminance scale which in fact represents nominal grey-values.

For benchmarking, a linearisation technique is used as described in section 5.1.2. The 7-bit values of the linearisation vectors are then multiplied with the grey-values of the set of test images. Accounting for both the shorter injection times and the smaller current amplitude needed with discharging at threshold voltage level, this method allows for power savings around 25%. The importance of the threshold

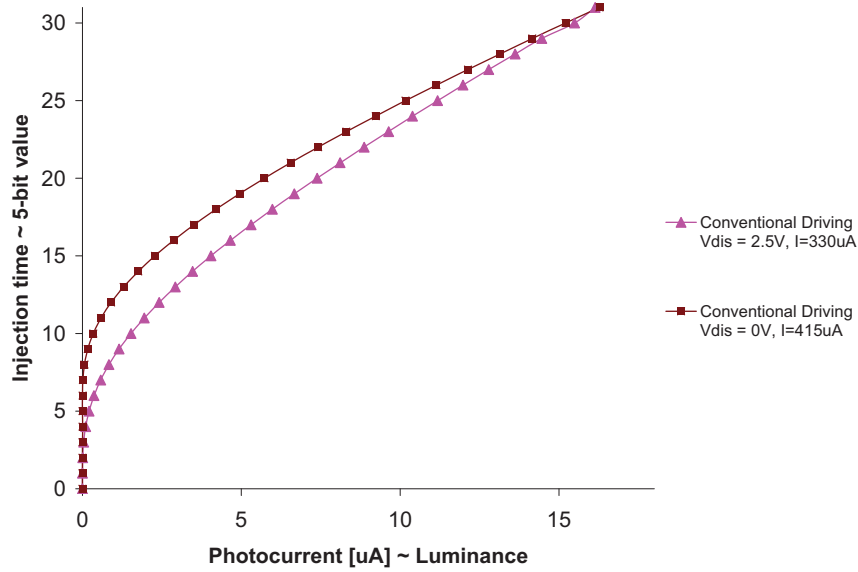


Figure 4.3: Luminance transfer curves with discharge at 0 V and at $V_{th} = 2.5 V$

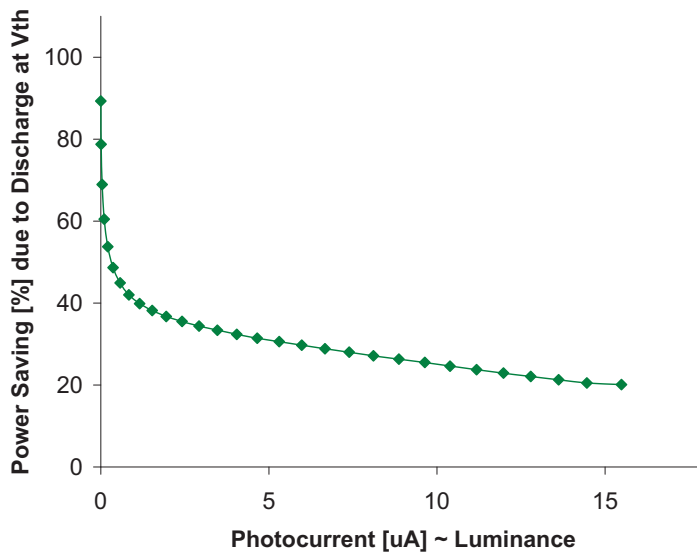


Figure 4.4: Power saving percentage due to discharge at threshold voltage level

voltage in this context has already been described qualitatively in literature [20], so it is neither part of the core findings of this work, nor it is considered as added value with respect to the elaborated power saving method. For the sake of consistency, discharge is however carried out further on at threshold voltage level in the implementation and comparison of conventional and SQC driving.

4.2 Natural Discharge and Post-luminescence

A first preliminary power-optimised driving scheme is based on the principle that the charge (energy) stored in the capacitance of the OLED pixels does not need to be artificially discharged (dissipated), but can be reused [88]. The challenge is to ensure that the nominal grey-value is precisely met.

After the current injection time, a high-impedance (hZ) state is introduced and the column side is left floating. During this period, the charge stored in C_{eq} flows through the addressed OLED and is converted into light. This phenomenon is referred as post-luminescence (figure 4.5). Consequently, the injection time, which is linked to the power consumption of the display module, is reduced for the same effective luminance. This new driving scheme is referred further on as hZ . An issue in this context is the fact that the light generated during postluminescence is not constant. It depends on the anode voltage V_{col} at the end of the injection phase and the duration of post-luminescence.

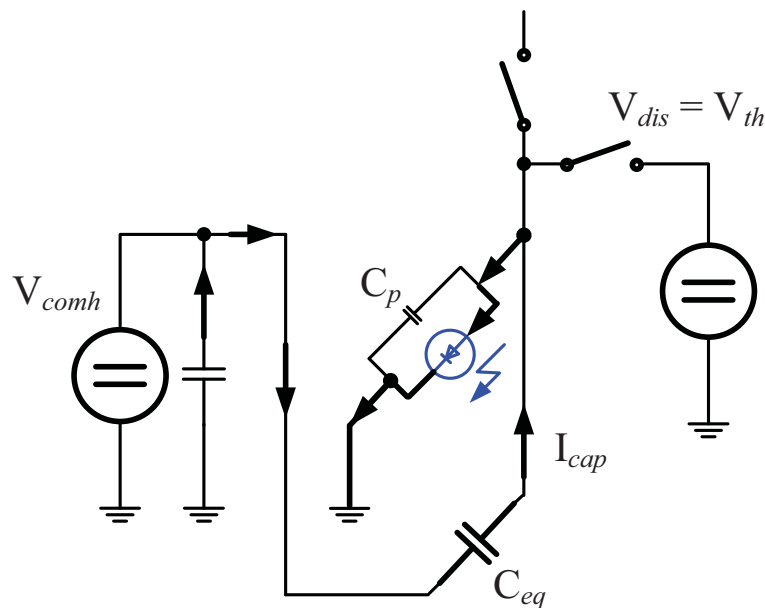


Figure 4.5: OLED post-luminescence and the discharge circuitry

The photon current emitted by an OLED is proportional to the electrical current through the diode. Thus, the light intensity Lum perceived by the human eye by means of integration (time-averaging) is proportional to the electrical charge Q_{lum}

used.

$$Lum = k \cdot Q_{lum} = k \cdot \int_0^{t_{row}} I_{OLED}(t) \cdot dt \quad (4.6)$$

The amplification factor k has been broken down and analysed in detail in section 3.1.3.

The row addressing time t_{row} is shared between an active injection period t_{inj} and a high-impedance (open) state t_Z of the column driver output.

$$t_{row} = t_{inj} + t_Z \quad (4.7)$$

The pixel luminance is thus regarded as a sum of two components (figure 5.3):

$$Q_{lum} = Q_{lum_{inj}} + Q_{lum_Z} \quad (4.8)$$

The main difference with respect to standard driving is that discharge is carried out only and always at the end of the row addressing time. This allows for a defined starting point (state) of the next pixel/row in the addressing sequence. In order to assess and implement this driving scheme, the linearisation of the input-output function based on appropriate display characterisation is mandatory. This is presented in detail in section 5.1.3.

4.3 The SQC Driving Scheme

A novel innovative driving scheme has been elaborated to further reduce the power consumption of PMOLED display modules by nearly eliminating the capacitive losses described in 3.4. It is the core development of the present work.

The driving scheme relies on the following principles:

- The remaining charge at the end of each row addressing time (after post-luminescence) is *shifted* to the next pixel of the column to be addressed. By this means, the discharge phase is usually avoided and the capacitive energy is reused. Moreover, the next pixel is implicitly precharged so that no precharge time is needed.
- There is one exceptional case when this does not apply, i.e. if the addressed pixel is very bright and the remaining charge is high while the next pixel is very dark. The shifted charge would produce more post-luminescence than

desired. In this case C_{eq} needs to be discharged ($D_{ij} = 1$ in equation (4.9)) to the level of the threshold voltage V_{th} of the OLEDs. Furthermore, as V_{col} has been reduced due to post-luminescence, the power loss caused by discharge is minimal. This case is rare, so that by applying this driving scheme the charge stored in the OLED capacitances is reused and the capacitive power loss is substantially reduced. It can be expressed as follows:

$$P_{disSQC} \sim \sum_{i=1}^{N_{rows}} \sum_{j=1}^{N_{col}} D_{ij} \cdot N_{rows} \cdot C_p \cdot (V_{col,ij} - V_{th}) \quad (4.9)$$

$$D_{ij} = 0 \text{ or } 1$$

The scheme is validated further on with a set of 36 test images (section 6.2). In this demonstrative case, discharge is needed on average for 4.28% of the pixels of natural images and 41% for graphics. The high figure for graphics results from the fact that this statistical value takes into account also the very frequent zero luminance (black) pixels that are discharged by default regardless of the available (preceding) charge.

As C_p is constant, the anode voltage V_{col} is an indicator of the stored electrical charge Q_{cap} (equation 4.10). As discharge is avoided, the voltage at the end of each row addressing is variable. This also means that the initial state $Q_{cap,i}$ (or $V_{col,i}$) of each row addressing sequence is variable.

The charge stored in the parasitic capacitance C_{eq} at the (anode) voltage $V_{col,i}$ is determined by the following formula while i denotes the row number:

$$Q_{cap,i} = C_{eq} \cdot V_{col,i} \quad (4.10)$$

As C_{eq} is constant, the so-called *state* can be represented either by the capacitive charge Q_{cap} or the anode voltage V_{col} . Both terms are used throughout this thesis and are interchangeable.

The implementation of the driving scheme relies on the principle of light generation by means of charge recombination (equation 6.1) and the physical law of charge conservation expressed as follows:

$$Q_{in,j} + Q_{cap,i} = Q_{lum} + Q_{cap,i+1} \quad (4.11)$$

4 The Principle of State-dependent Charge-controlled (SQC) Driving

The sum of the initial charge $Q_{cap,i}$ and the charge injected by the driver Q_{inj} equals the sum of the charge converted by the OLED into light Q_{lum} and the remaining charge $Q_{cap,i+1}$ (equation 4.11). For this reason, the control of this driving scheme is state-dependent and based on charge balance. The scheme is therefore referred as state-dependent and charge-controlled (SQC).

Q_{inj} is the charge injected by the constant current source and equals:

$$Q_{inj} = I_0 \cdot t_{inj} \quad (4.12)$$

By means of equation 4.6, 4.10 and 4.12, equation 4.11 can be extended to:

$$I_0 \cdot t_{inj} + C_{eq} \cdot V_{col,i} = \frac{Lum}{k} + C_{eq} \cdot V_{col,i+1} \quad (4.13)$$

All parameters in equation 4.13 are either controllable or measurable which is fundamental for the SQC algorithms described in detail in chapter 5.

With equation 4.7 and 4.8, the desired pixel luminance Q_{lum} can be expressed as a function of the charge inherited from the previous pixel, the injection current amplitude, the duration of injection and the duration of the high-impedance state.

$$Q_{lum} = f(Q_{cap,i}, I_0, t_{inj}, t_Z) \quad (4.14)$$

Equation 4.14 provides the basis for the state-dependent calculation of t_{inj} and t_Z for each pixel.

Since the OLED current is a nonlinear function of the voltage, equation 4.14 is non-linear and can be employed by means of pre-characterised look-up tables as described in section 5.2. The state-variable $Q_{cap,i}$ is discretised and the next state $Q_{cap,i+1}$ is calculated by means of equation 4.11.

The implementation and corresponding algorithms are detailed in section 5.2.

Concerns have been raised regarding potential error accumulation, for instance due to state discretisation which may impact image quality and stability. In this context, the robustness of the scheme and the visual quality are analysed and demonstrated in chapter 7.

5 Algorithm, Implementation and Characterisation of Display Parameters

5.1 Image Processing for Displays

So far, the relation between the injection time and the produced pixel luminance has been considered linear (figure 4.2). This is valid however only as long as the OLED current is constant (equation 4.6). Given its capacitive component and specific waveform (figure 3.11), linearity is no longer provided by default. Linear dependency is important for two reasons: to assess and compare different driving schemes and to reproduce any source image as accurately as possible. To this end, a linearisation technique is presented in section 5.1.2. Prior to that, the concept of *gamma correction* is briefly discussed as the two are to some extent related. This explanation should avoid confusion.

5.1.1 Gamma Correction

The root phenomenon behind gamma correction in image processing is the fact that human perception of light intensity is non-linear. The human eye is more sensitive to intensity changes in low light than in bright conditions. However, at the same time the output of image sensors, i.e. the RAW data, is in the physical domain and thus linear. This digitised value is usually compressed (encoded) to a lower resolution for storage and efficient transmission purpose. If coding were linear, fine differences between darker pixels would be lost, even though the eye is able to distinguish them. At the same time, the resolution allocated to the brighter pixels would be wasted, as in that range the eye is less capable to differentiate.

This difference is depicted in figure 5.1 in which the sensor and the eye response to incoming light are qualitatively compared so that a half-scale brightness level in an 8-bit system would generate a sensor response of 127 and a human eye response of 186 [5]. Linear encoding would lead in practice to a very dark image reproduction as illustrated in figure 5.2 for $\gamma = 1$.

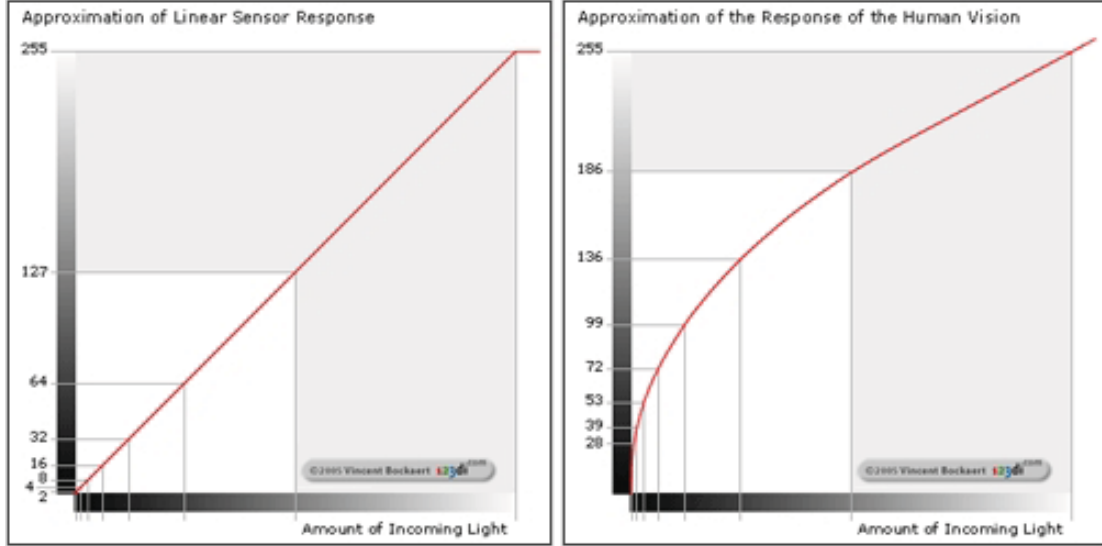


Figure 5.1: Generic sensor and eye response [5]

The straight-forward solution to this problem is the application of non-linear data compression (encoding) upon image recording and the inverse data expansion (decoding) before image reproduction. These operations are referred as gamma correction. In most common cases, gamma correction is defined by the following power-law expression [79], with $V_{in}, V_{out} \in [0, 1]$ and $\gamma < 1$ for compression (encoding) and $\gamma > 1$ for expansion (decoding):

$$V_{out} = V_{in}^{\gamma} \quad (5.1)$$

To compensate for the non-linear human eye response, a gamma of 0.45 ($1/2.2$) is commonly used for encoding. Historically, this value has been accidentally a good match for the natural non-linear response of CRT displays, which have themselves a transfer function with $\gamma_{CRT} = 2.2$ so that decoding was implicit. Both functions are depicted in figure 5.2. The image processor of modern displays or other image reproducing devices like printers or projectors is usually supposed to decode the image data applying an inverse gamma of 2.2 before passing it to the driver, provided that the latter has a linear transfer function.

In practice, gamma encoding or even additional tonal curves [5] are applied for two further reasons: to compensate for the low dynamic range of image reproducing devices and also to produce a final image more pleasant to the eye, even though it may be no longer a linear map of the initial image sensor read-out. For instance, JPEG still images are explicitly encoded while the commonly used sRGB colour space uses custom tailored gamma decoding [79]. In consequence, this makes the precise comparison and benchmarking of different devices or driving schemes rather difficult. An example image with different gamma encoding values is shown in figure 5.2. Gamma correction is thus a good compromise between a high contrast and the reproduction of dark details.

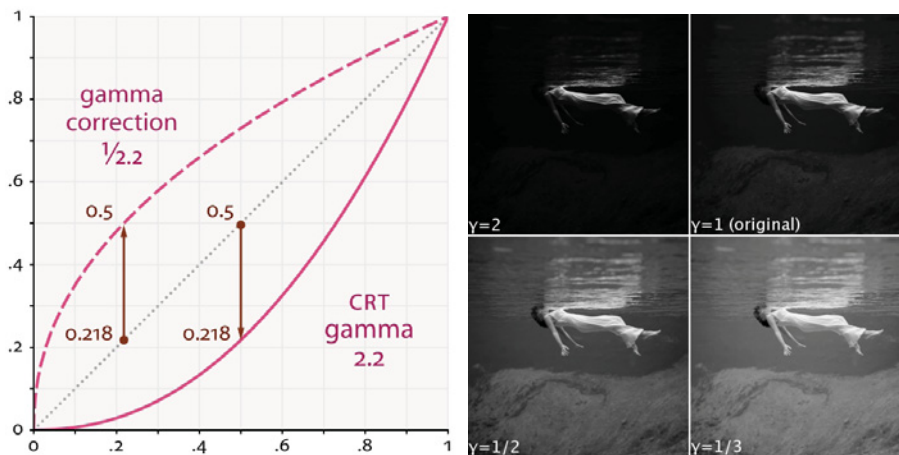


Figure 5.2: Gamma transfer functions and the impact of their variation [79]

5.1.2 Linearisation

The main rationale behind the need for linearisation in the implementation and benchmarking of SQC driving is the fact that it is based on a physical model. The impact of the capacitive current on the transfer characteristics $Lum = f(\text{grey-value}) = f(t)$ on the analysed driving schemes needs to be considered accurately.

Figure 5.3 shows qualitative pixel current and voltage curves for the three driving schemes described in chapter 4, i.e. conventional driving, hZ and SQC, all for the same current injection time. The generated light is proportional to the area of the current waveform while the power consumed is proportional to the duration of the injection phase t_{inj} . It is obvious that the new driving schemes hZ and SQC are more efficient.

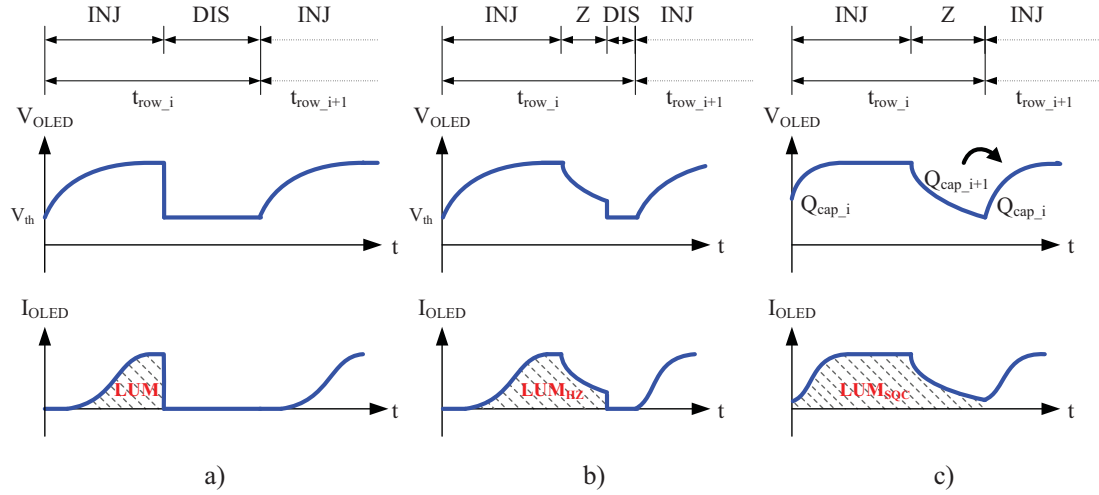


Figure 5.3: Qualitative comparison of the efficiency of driving schemes:

- a) Conventional driving with immediate discharge at V_{th}
- b) hZ with post-luminescence and discharge at V_{th}
- c) SQC with no discharge

In a first instance, when testing standard or hZ driving, the generated images were very dark, providing only a coarse reproduction of their sources. This is reflected in the non-linear transfer functions, depicted in figure 5.4. The lower bit values are suppressed, image information is lost and the output is darker than the original. As charge is also supplied to the OLED capacitance, the injected charge is not fully converted into light. The relationship between luminance and injection time is not linear, but to a certain extent similar to a decoding gamma curve. The native transfer function resembles thus the gamma decompression or decoding as described above, however not with a constant gamma exponent but with values ranging from $\gamma[2] = 0.36$ to $\gamma[30] = 0.80$ for standard 5-bit driving with discharge at threshold voltage level.

To facilitate a precise reproduction of test images but also for a fair comparison of driving schemes, the grey-values need pre-processing to ensure a linear transfer function. Given the resemblance to gamma processing, this step is often described as *gamma correction* [17], however here it will be referred to as linearisation. The basic principle is depicted in figure 5.5. The maximum luminance is divided by the number of resolution steps (31 in this example) to compute ΔLum , i.e. the desired linear light increment. All 31 values are then mapped to the native transfer function and the result is then recorded into a linearisation-vector of

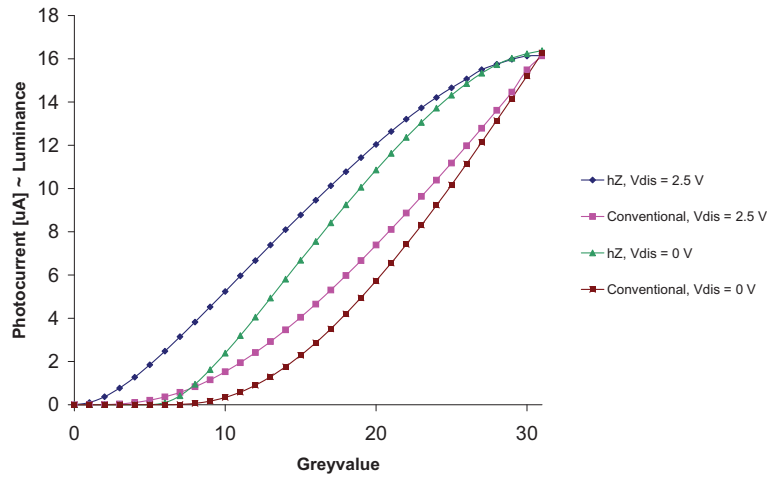


Figure 5.4: Measured luminance as a function of current injection duration

higher resolution, e.g. 7-bit. Whenever a bit value is to be displayed, the injection time will be set according to the corresponding value from the linearisation-vector, thus ensuring a linear reproduction.

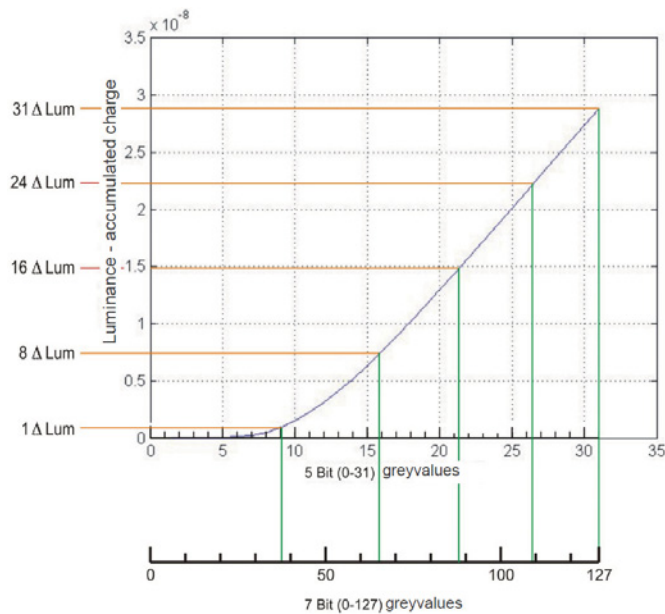


Figure 5.5: Linearisation example (adapted from [4])

Figure 5.6 shows the difference between native and linearised driving. Without linearisation, the output is excessively dark and many details are lost, e.g. the eyes of the subject. With upfront linearisation, the output is more true to the original.



Figure 5.6: Test image (centre) displayed conventionally with linearisation (right) and without (left)

For the purpose of this thesis, grey-scale JPEG source images have been used to test the different driving schemes. The Matlab function *imread* was used to import the files and convert them subsequently into 5-bit matrices. Their content is a linear representation of the subject as sRGB decoding occurs before the extraction of the grey-values in Matlab. In any case, the described linearisation happens in the physical domain and allows for consistency in the implementation and comparison of driving schemes, regardless of the nature of the source image.

Figure 5.7 is an overview of the common gamma processing steps, i.e. compression and decoding, undergone by an image from recording by a camera or scanner, to reproduction on a display, beamer or printer. It also contains the linearisation step carried out in the SQC preparation and the subsequent reproduction of SQC generated images. One purpose is to clarify the link between gamma processing and the presented linearisation technique. In addition, it shows that the comparison of a reproduction with its source is not trivial given the many processing steps that bias the image content. In practice, a test image is assessed visually at runtime or it is recorded with a camera and assessed subsequently on a monitor by comparing it with the source image. Due to the different upfront processing steps, recording and reproduction devices, this comparison is not entirely bias-free. Ideally, the best comparison would be between the image perceived at runtime on the display under test and the subject itself (marked with an asterisk in figure 5.7).

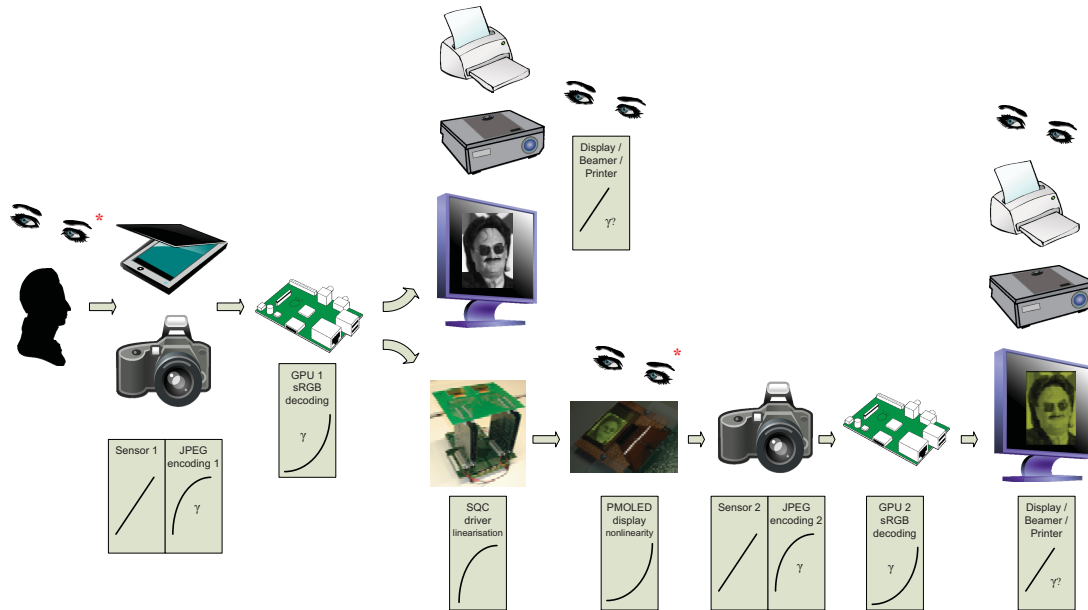


Figure 5.7: Image processing flow: gamma coding and OLED driver linearisation

5.1.3 Benchmarking

The described linearisation has a further advantage. It allows the efficiency gains of the elaborated driving schemes, i.e. hZ and SQC, to be benchmarked against conventional driving. As the injected power is proportional to the row injection time, the linearisation vectors and the distribution of grey-values over a certain set of test images are sufficient to compute the mean energy needed to display them. The power injected for each pixel is reflected by the product of the corresponding linearisation value and the grey-value. Once the linearisation vectors are given, this computation can be made offline for any given set of images.

While the linearisation vector can be easily obtained for conventional and hZ driving following the procedure described above, it is not straightforward in the case of SQC. A workaround is provided by an analytical hypothesis: if SQC is nearly lossless in terms of capacitive power, the capacitive current share is negligible and the native transfer function $Lum = f(\text{grey-value}) = f(t)$ must be a straight line with a slope proportional to the injection current amplitude. This slope is already reflected in the linear part of the transfer function for standard driving which no longer has a capacitive component. By shifting (transposing)

this line segment to the origin (figure 5.8) and setting an upper limit at the maximum luminance ($Lum_{max} = 31 \cdot \Delta Lum$), the capacitive current flow is virtually eliminated and driving would be ideal. At the same time, the light conversion characteristics of the display would be maintained making benchmarking possible. The theoretical transfer function could be then expressed as $Lum = k \cdot I_{inj} \cdot t$, with the proportionality factor k accounting for the OLED physical characteristics and the amplification of the measurement equipment (section 6.2). The shifted curve has much lower injection times for the same luminances. The linearisation vector can then be determined in the same manner as described in section 5.1.2.

The native transfer functions for conventional, hZ driving and the SQC equivalent are depicted in figure 5.8.

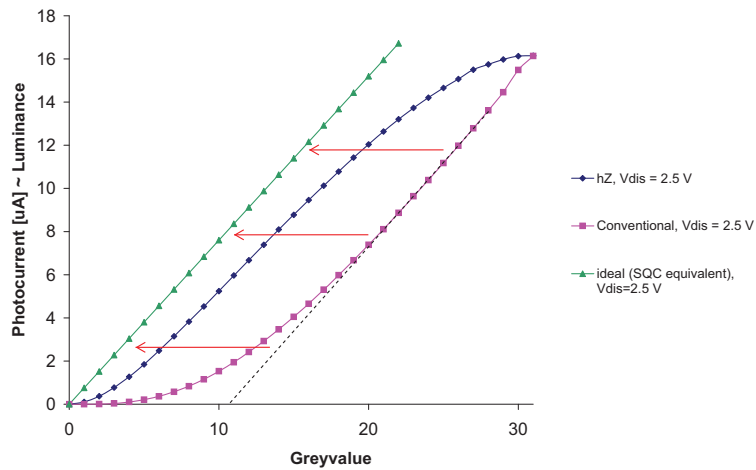


Figure 5.8: Transfer functions for conventional, hZ and SQC equivalent driving

Figure 5.9 is a plot of the three linearisation vectors, which are used to estimate the efficiency gains for hZ and SQC with respect to conventional driving. A mixed set of 36 greyscale 5-bit 96 x 64 natural pictures and graphics are used. As the overall density of grey-values, i.e. the cumulative histogram, impacts the efficiency gain, it is depicted in figure 5.10. The two outliers in the case of fully black or white pixels are explained by the considerable number of graphics used. They are all depicted later on in figure 6.6.

Using this analytical method, hZ driving results in 20% energy saving and SQC in 43%, with respect to conventional driving. This outcome is then tested in practice and the measurement results are described in section 6.2.

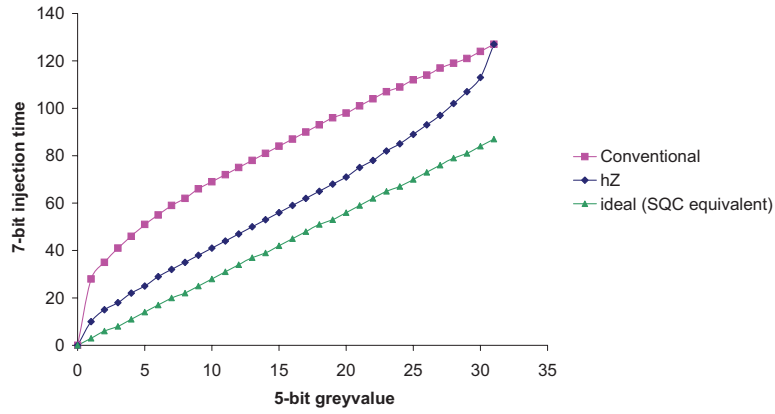


Figure 5.9: Linearisation vectors

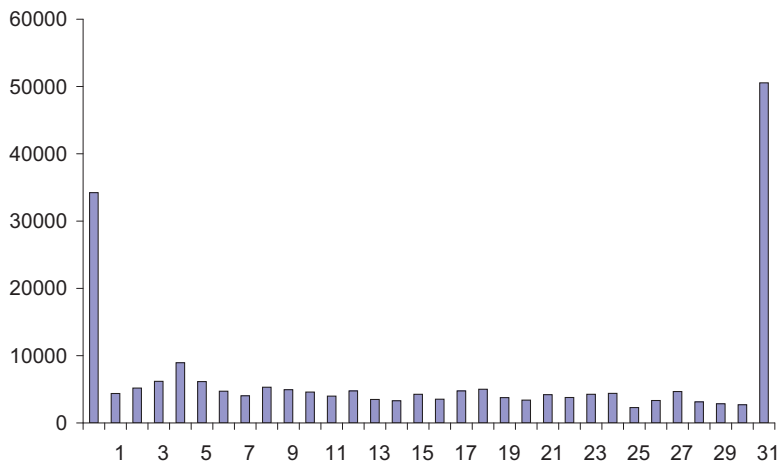


Figure 5.10: Histogram of a set of 36 test images (cumulative)

5.2 SQC Algorithms

This section describes the two algorithms used to determine the control signals (injection time and discharge bit) for demonstrating and evaluating the SQC driving scheme. They are developed and executed off-chip in Matlab. The output is used to generate SQC images with the drivers described in section 6.1. The basic principle of the algorithms is depicted in Figure 5.11. As the columns of a PMOLED display are decoupled (section 3.4) and the driving scheme is elaborated accordingly, the algorithms run sequentially for each pixel in a column following the addressing direction (usually top-down). Thus, for each pixel, the input data consists at run-time of the nominal luminance or grey-value (Lum), the available capacitive charge specified by the initial anode voltage ($V_{col,i}$) and a set of look-up

tables characterising the display. The OLED capacitance C_{eq} and the amplification factor k are also considered. The output to be generated is the injection time, the discharge bit and the remaining charge at the end of the row addressing time. The latter is the state variable and is used in processing the next pixel.

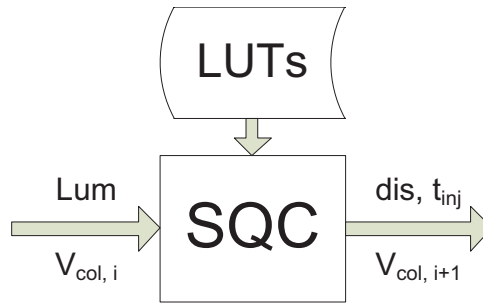


Figure 5.11: SQC algorithm principle [24]

The two algorithms differ in terms of complexity and on-chip applicability. The main difference is given by the size and dimensions of the required look-up tables which impact the characterisation method and effort. For this reason one is referred as 2D- and the other as 1D-algorithm.

The 2D-algorithm was elaborated in a first instance as a proof of concept. It was used to produce and display SQC test images to validate the concept in terms of efficiency gains and visual quality. It is straightforward but requires a cumbersome hardware realisation with practically poor perspectives of integration or industrialisation. 2D refers to the dependency of each LUT characterisation datapoint on two variables, i.e. injection duration and initial state.

The 1D-algorithm was conceived in [90]. It substantially simplifies the display characterisation process and relaxes the computation requirements by means of a sophisticated algorithm such that only 1D-LUTs are needed. It produces the same visual results and efficiency performance as the 2D-method while offering perspectives for chip integration into an image processing unit since the hardware cost for 1D-LUTs is much lower than for 2D-LUTs. The 1D-algorithm has been used further in the development of a pipeline-processor [24].

The Matlab code was mainly realised in collaboration [9]. Guidance was provided to assure a focussed methodology and consistence of data and interfaces.

5.2.1 Measurements and Characterisation Setup

The outcome of display characterisation is the generation of look-up tables needed to implement the SQC algorithms. This step and the benchmarking of driving schemes (section 6.2) is carried out using a measurement setup consisting of a photodiode Newport *818 SL-L* [56], a piccoamperemeter Keithley 6485 [38] and an oscilloscope Agilent *InfiniiVision 5000* [2]. The photodiode (figure 3.6) is attached to the display using a fixture so that its entire sensing area is over the display surface. The light emitted by all covered pixels is thus sensed by the photodiode and converted into electrical current. The piccoamperemeter is used to measure the average photodiode current in the μA range. The oscilloscope is used to measure the anode voltage. By triggering it with one row activation signal and by sampling always the same anode, the voltage at the same pixel can be consistently measured which is equivalent to the state variable used by the SQC driving scheme.

To characterise the display, different waveforms must be driven depending on the implemented algorithm. Furthermore, several parameters like the initial voltage or the PWM duration need to be varied to populate the LUTs. Nevertheless, in order to consider the setup constraints and obtain a measurable photocurrent, all pixels of the display are driven simultaneously with the same current waveform. The readout of the amperemeter is thus proportional to the light produced by one pixel, as all pixels under the sensing area of the photodiode are driven identically. Apart from signal amplification and measurability, this method assures also a homogenisation of the pixel properties. The amplification factor k used in the fundamental SQC equation 4.13 is described in section 3.1.3.

5.2.2 2D-Look-up Tables

The 2D-algorithm uses many data-points to cover the whole range of initial conditions (i.e. voltages) at the beginning of the pixel addressing time, combined with variations of the injection time. The row addressing time is constant and is composed of an injection part and a high-impedance (post-luminescence) part.

The x-axis of the 2D-measurement is thus the discrete injection time and the time unit mostly used in further statements is t_{lsb} . In this particular case the implementation has used a 5-bit system so that the injection time can range from $0 \cdot t_{lsb}$ to $31 \cdot t_{lsb}$. $3 \cdot t_{lsb}$ are reserved at the end of each row addressing sequence

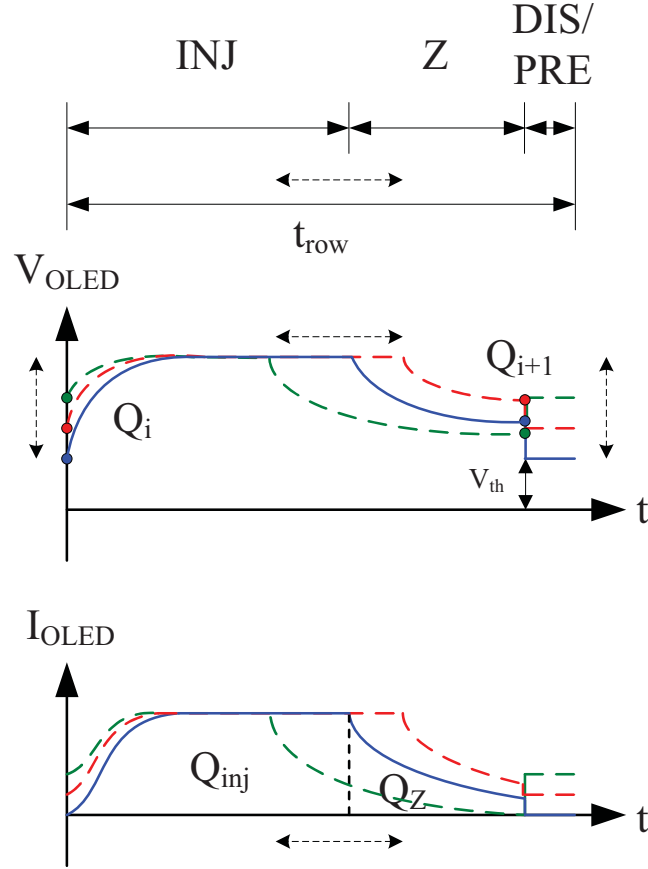


Figure 5.12: 2D-characterisation waveforms (qualitative)

to carry out discharge. Therefore the row addressing time de-facto consists of $31+3=34$ time units t_{lsb} . For the sake of development simplicity, the t_{lsb} duration of $5 \mu s$ has been kept. This leads to a row addressing time

$$t_{row} = 5 \mu s \cdot 34 = 170 \mu s \quad (5.2)$$

Driving a display with 64 rows, the frame period is

$$T_{frame} = 170 \mu s \cdot 64 \approx 11 ms \quad (5.3)$$

Hence the nominal demonstration frame frequency is approximately $90 Hz$.

The y-axis of the 2D-LUTs is the initial state defined by the charge available in the row capacitance, reflected by the anode voltage. This initial state can be varied

by means of an external voltage source. A concrete example for a precharge and discharge circuit is described in section 6.1.1.

The lower limit of the initial state is set to 2.5 V . This value is empirically determined as the threshold voltage of the OLEDs under test, i.e. the highest forward voltage level for which light emission is no longer perceived.

The upper limit is set to 7.5 V . This value was determined by the fact that the maximal pixel luminance is defined with an initial voltage of 2.5 V an injection current of $I_{inj} = 330\text{ }\mu\text{A}$ and the maximum injection time $t_{inj} = 31 \cdot t_{lsb}$. Under these circumstances, the measured forward voltage of the pixel OLED is $V_{FD} \approx 7.25\text{ V}$. Any other possible final state will be less which justifies the choice of 7.5 V as the upper limit.

The higher the resolution of the initial state, the more accurate is the algorithm. There is however a trade-off in terms of measurement efforts and size of the LUTs resulting in a limited number of characterised states (initial voltages) with 10 values considered as a good compromise. At the same time, the human vision response to brightness is not linear (section 5.1.1) with the eye being more sensitive to changes at low light. In addition, the value of the initial voltage could be a rough indication if the pixel to be addressed is rather dark or bright. For this reason, the chosen initial voltage increments are not constant. They are smaller in the lower range and larger in the higher range. Measurements have been thus taken with the following initial states: 2.5 V , 2.75 V , 3 V , 3.25 V , 3.5 V , 4 V , 4.5 V , 5.5 V , 6.5 V and 7.5 V . Such a set of discrete steps better accounts for the non-linearity at the lower end of the curves as illustrated in figure 5.4. It is a good compromise between accuracy and hardware cost. Measurements with 0 V initial state are performed as well, even though the anodes never reach this value at runtime, with forced discharge always at $V_{th} = 2.5\text{ V}$ and natural discharge at higher values. This is done to allow the algorithm to exceptionally run also slightly beyond the physical limitation.

The initial voltage is set during an empirically determined duration of $3 \cdot t_{lsb} \approx 15\text{ }\mu\text{s}$ to allow sufficient precharge time. As during this state some current flows inevitably also through the OLED itself, the luminance is recorded with an offset. This needs to be singled out for each characterised initial state with a precharge-only waveform and subtracted from all luminance measurements accordingly.

The measurements are recorded in table 5.1 .

$Q_i(V)$	0		2.5		2.75		...		7.5	
$t_{inj}(bit)$	$I_{Ph}(\mu A)$	$Q_{i+1}(V)$	$I_{Ph}(\mu A)$	$Q_{i+1}(V)$	$I_{Ph}(\mu A)$	$Q_{i+1}(V)$	$I_{Ph}(\mu A)$	$Q_{i+1}(V)$
0	0	0	0	2.36	0	2.56	9.7	3.83
1	0	0.3	0.11	2.67	0.27	2.82			10.63	3.88
2	0	0.63	0.38	2.88	0.64	3			11.49	3.91
...
30	11.21	6.2	17.5	6.4	18.2	6.46			30.6	6.63
31	11.3	6.55	17.6	6.78	18.3	6.86			30.7	7.01

Table 5.1: 2D-characterisation measurements (excerpt)

For each pair of data points, i.e. luminance and final state in function of the initial state and the injection time, the fundamental SQC equation 4.13 holds. To reflect the above naming of parameters, it can be rewritten to equation 5.4. This set of measurements represent a first practical validation of the SQC principle.

$$I_{inj} \cdot bitvalue \cdot t_{lsb} + C_{eq} \cdot Q_i = \frac{I_{Photo}}{k} + C_{eq} \cdot Q_{i+1} \quad (5.4)$$

Provided that $I_{inj} = 330 \mu A$, $t_{lsb} = 5 \mu s$, $C_{eq} = 64 \cdot 78 pF$, $\frac{1}{k} = 1.6 ms$, the equation can be verified for example for the data-point expressed by $Q_i = 2.75 V$, $bitvalue = 30$, $Q_{i+1} = 6.46 V$, $I_{Photo} = 18.2 \mu A$. Any inaccuracy is due to systemic measurement and modelling errors.

The plots in figure 5.13 illustrate the two-dimensional nature of the measurements. Each z-axis value, be it the luminance or the final state, is a function of two parameters, i.e. the injection time and the initial state.

The characterisation process to populate these 2D-LUTs is cumbersome. Nevertheless, in addition to the required data-points, i.e. luminance and final state, additional parameters are measured for all input combinations of injection time and initial state. Measuring the supply current, the discharge current and the peak diode voltage at the end of the injection phase facilitated the extraction of display parameters described in section 3.1.

A finite number of data-points, each defined by an initial state and injection time, can be recorded. The algorithm needs however to process pixels with an arbitrary initial state and generate the necessary injection time required to produce the set pixel luminance. To this end, linear interpolation is applied. This interpolation method is chosen for its simplicity and ease of implementation. The objective is to deliver the injection time, the discharge bit value and the next state for a given grey-value and initial state.

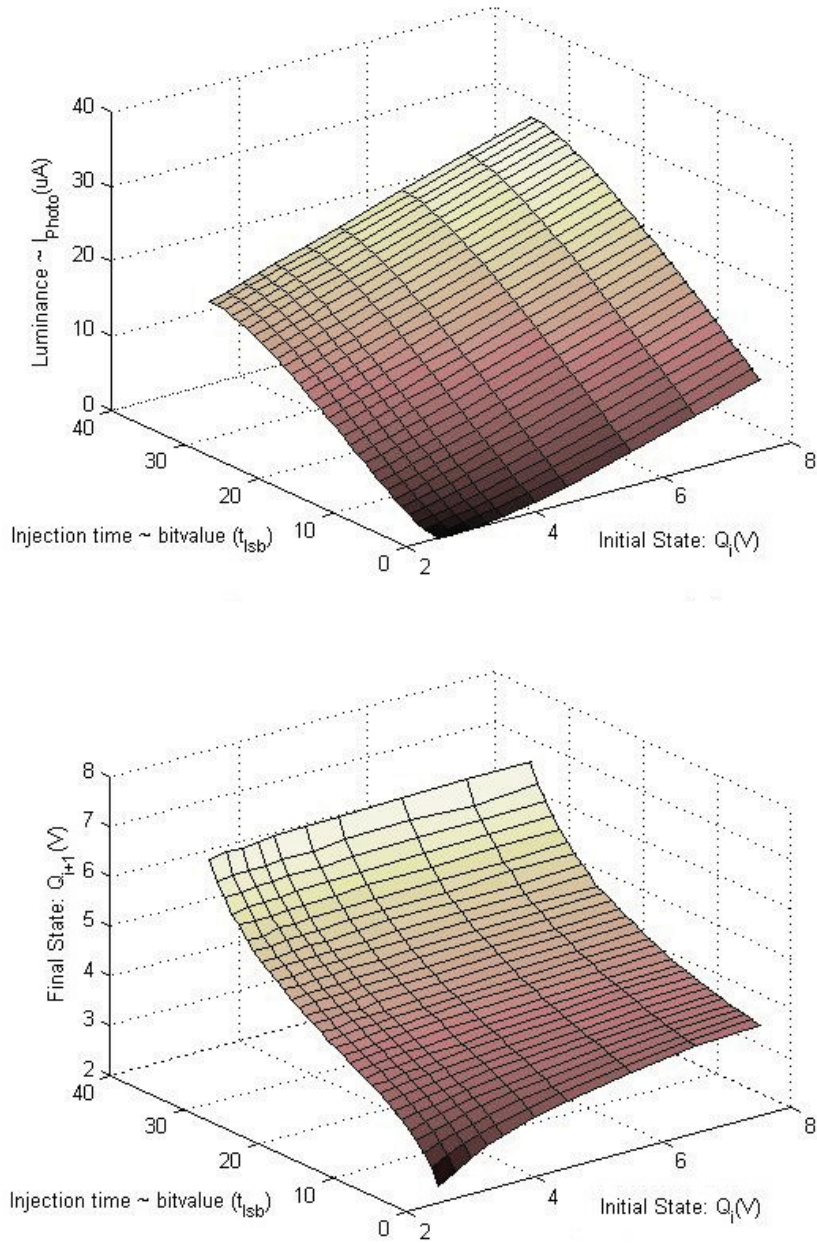


Figure 5.13: Plots reflecting the two-dimensional nature of the characterisation look-up table for the 2D-algorithm. Luminance (top) and final state (bottom), both as function of initial state and injection time

The principle of linear interpolation is outlined in figure 5.14. Any intermediate value Y_{IP} between two consecutive data-points Y_{left} and Y_{right} of a discrete function $y[n] = f(x[n])$, is approximated by assuming it is on the straight line

connecting these two points. Its position is given by the relative position of the x-coordinate X_{set} in the interval $[X_{left}, X_{right}]$.

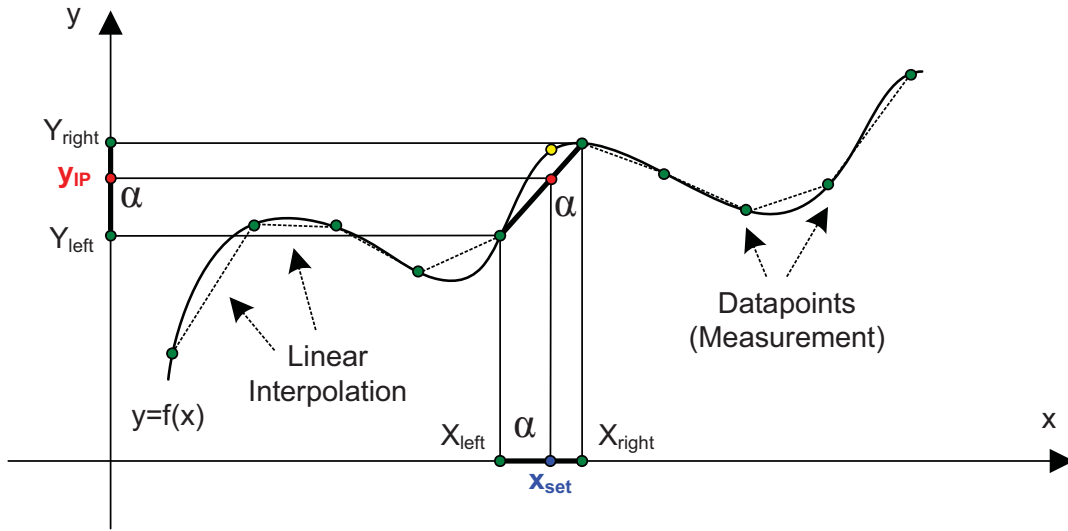


Figure 5.14: Principle of linear interpolation

For a monotonically increasing interval, the interpolated value Y_{IP} is thus obtained with the formula:

$$Y_{IP} = f(X_{set}, X_{left}, X_{right}, Y_{left}, Y_{right}) \quad (5.5)$$

$$Y_{IP} = Y_{left} + \frac{X_{set} - X_{left}}{X_{right} - X_{left}} \cdot (Y_{right} - Y_{left}) \quad (5.6)$$

with

$$X_{left} \leq X_{set} < X_{right}$$

and

$$Y_{left} < Y_{right}$$

The same technique can be applied to the inverse function $x[n] = f^{-1}(y[n])$ by inverting x and y in equation 5.7.

The linearity of the function between the two data points determines the interpolation error. For this reason, in the characterisation process shorter intervals have been chosen between consecutive data points where the functions are less linear, usually at lower x-coordinates.

The discharge phase adds some complexity to processing and display characterisation. To recall, discharge is needed in the rare case of a very bright pixel followed by a very dark one in the same column. The most convenient way of implementing this function is to reserve a discharge time slot at the end of the row addressing sequence, immediately after the post-luminescence phase. It is then the role of the algorithm to decide if discharge needs to be performed or not for each processed pixel. Alternatively, discharge can be carried out at the beginning of the addressing time. The principle for determining the discharge bit and injection time remains unaltered.

A duration of $t_{dis} = 3 \cdot t_{lsb} \approx 15 \mu s$ was empirically determined as the minimum value to assure proper discharge of the column capacitances and reset at $V_{dis} = V_{th} = 2.5 V$. This duration depends on the current sinking capability of the discharge voltage source, parasitic discharge path resistances and the size of the cumulative capacitance. If discharge needs to be executed, the measurements described above are sufficient for the algorithm to determine for each pixel the injection time and final state (figure 5.11). Given however the typical case when discharge is not needed, the post-luminescence phase is prolonged by the duration of the reserved discharge time slot of $3 \cdot t_{lsb}$ to preserve the row addressing time. Hence, the anode voltage falls below the interpolated value and the pixel emits additional light. To characterise this situation, an additional one-time 1D-measurement is required. To this end, the same characterisation setting is employed. However, the driving scheme is simplified to capture only the $3 \cdot t_{lsb}$ discharge phenomenon at various initial states. The same initial states are manually adjusted with the display driven only in *hZ*-mode and a high impedance duration of $3 \cdot t_{lsb}$. For the sake of consistency, the same frame frequency needed to be assured while the rest of the addressing time is idle with each pixel discharged at $V_{th} = 2.5 V$ and no further light emission. The characterisation driving pattern is depicted in figure 5.15. Applying a global adjustable initial voltage and discharging each pixel to the threshold voltage was possible using simultaneously the precharge and discharge circuitry of the *Spartan* demonstrator (section 6.1.1).

For this characterisation only the voltage drop for the ten pre-defined data points was captured (figure 5.16).

The values are then used by the algorithm to determine by means of interpolation any $3 \cdot t_{lsb}$ -voltage drop for all final states V_{i+1} characterised in table 5.1. Once

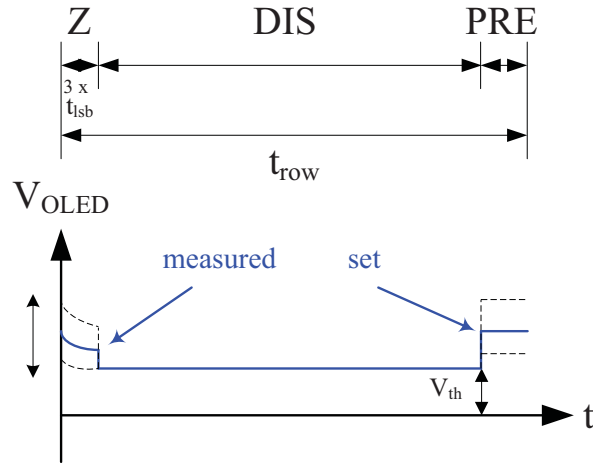
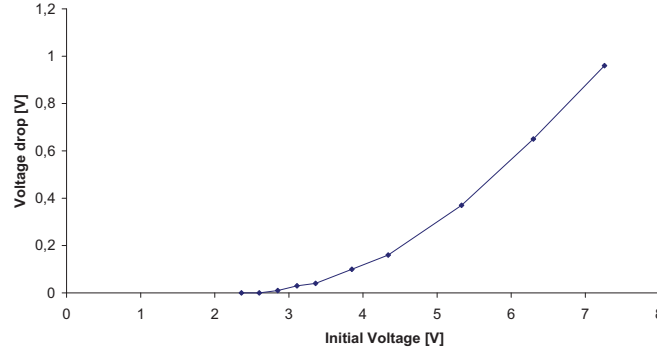


Figure 5.15: Discharge characterisation


 Figure 5.16: $3 \cdot t_{lsb}$ voltage drop

the interpolation interval is set by determining the two boundary values $V_{left} \leq V_{i+1} < V_{right}$, formula 5.7 is applied:

$$\Delta V_{i+1} = \Delta V_{left} + \frac{V_{i+1} - V_{left}}{V_{right} - V_{left}} \cdot (\Delta V_{right} - \Delta V_{left}) \quad (5.7)$$

To determine for each data-point the light emitted during the additional $3 \cdot t_{lsb}$ post-luminescence phase, equation 4.13 is used as follows:

$$Lum = k \cdot (I_0 \cdot t_{inj} + C_{eq} \cdot (V_{col,i} - V_{col,i+1})) \quad (5.8)$$

The 2D-LUT is thus extended with the $3 \cdot t_{lsb}$ voltage drop and the additional luminance produced accordingly for each data point. This represents the usual case when forced discharge is not required. An algorithm is developed to carry out this series of interpolations and generate the extended LUT.

Four consecutive interpolations are carried out to determine the injection time t_{inj} and final state V_{i+1} for a given set pixel luminance Lum_{set} and the initial state V_i using the extended 2D-LUT. A simplified flowchart is provided in figure 5.17. They are illustrated using the outline of the characterisation LUT in figure 5.18.

The extended LUT covers now the two possible situations, i.e. with or without forced discharge at the end of the row addressing sequence. There are two possibilities to proceed. One is to compute in a first run the parameters for the case without forced discharge using the values extended with the additional $3 \cdot t_{lsb}$ post luminescence, perform the discharge test at the end, and repeat in a second run the whole sequence with the native LUT data for the seldom case when forced discharge is needed. This option is described in listing 5.1. For the sake of programming convenience, a further possibility is to perform all operations in parallel with both the native and extended LUT data, perform the discharge test at the end and pick the appropriate solution. As this algorithm is used as a proof of concept only, there was no need to assess which option yields a better performance. Most likely the first option described above would represent a more efficient use of computing resources.

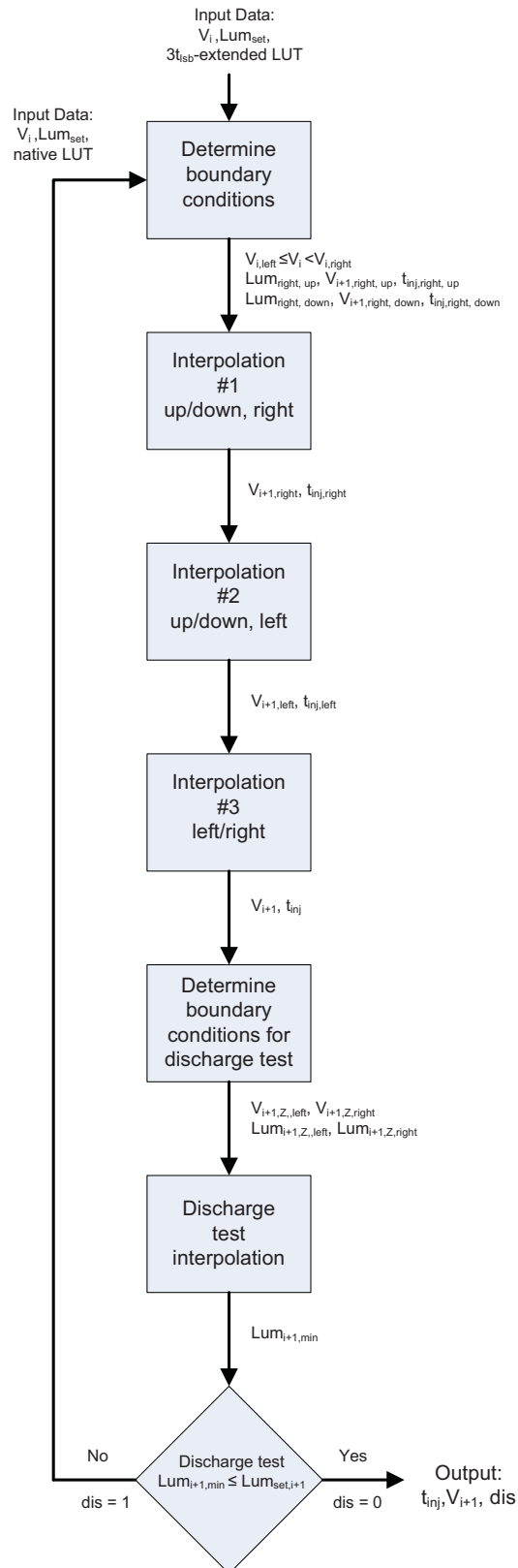


Figure 5.17: 2D-algorithm flowchart

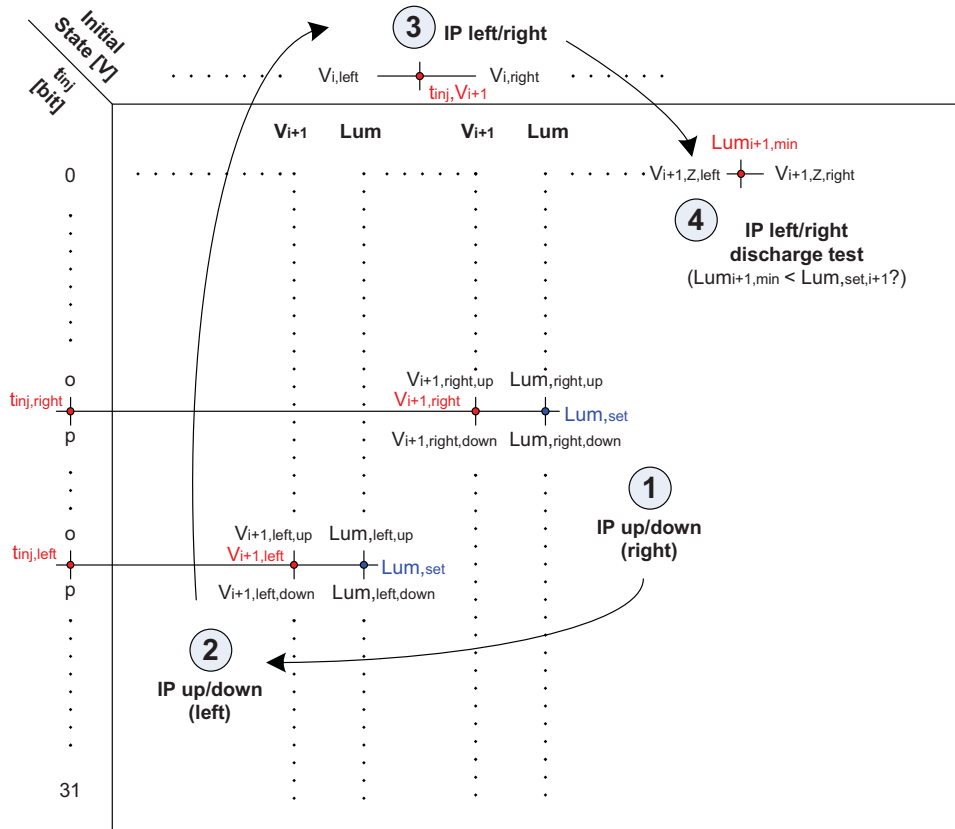


Figure 5.18: 2D-algorithm interpolations

5.2.3 The 2D-Algorithm

The algorithm performs as follows: At first, the two boundary values $V_{i,left}$ and $V_{i,right}$ from the set of characterised initial states are determined, such that $V_{i,left} \leq V_i < V_{i,right}$. The final state and luminance values from the two corresponding columns are then used in the subsequent processing for the first three interpolations.

The first two interpolations are equivalent. The set parameter is the pixel luminance. For each of the two boundary columns, the boundary parameters Lum_{up} and Lum_{down} are identified such that $Lum_{up} \leq Lum_{set} < Lum_{down}$. The injection times $t_{inj,left}$ and $t_{inj,right}$ needed to theoretically generate the same set luminance and the corresponding final states $V_{i+1,left}$ and $V_{i+1,right}$ are then interpolated. This process is depicted in figure 5.19.

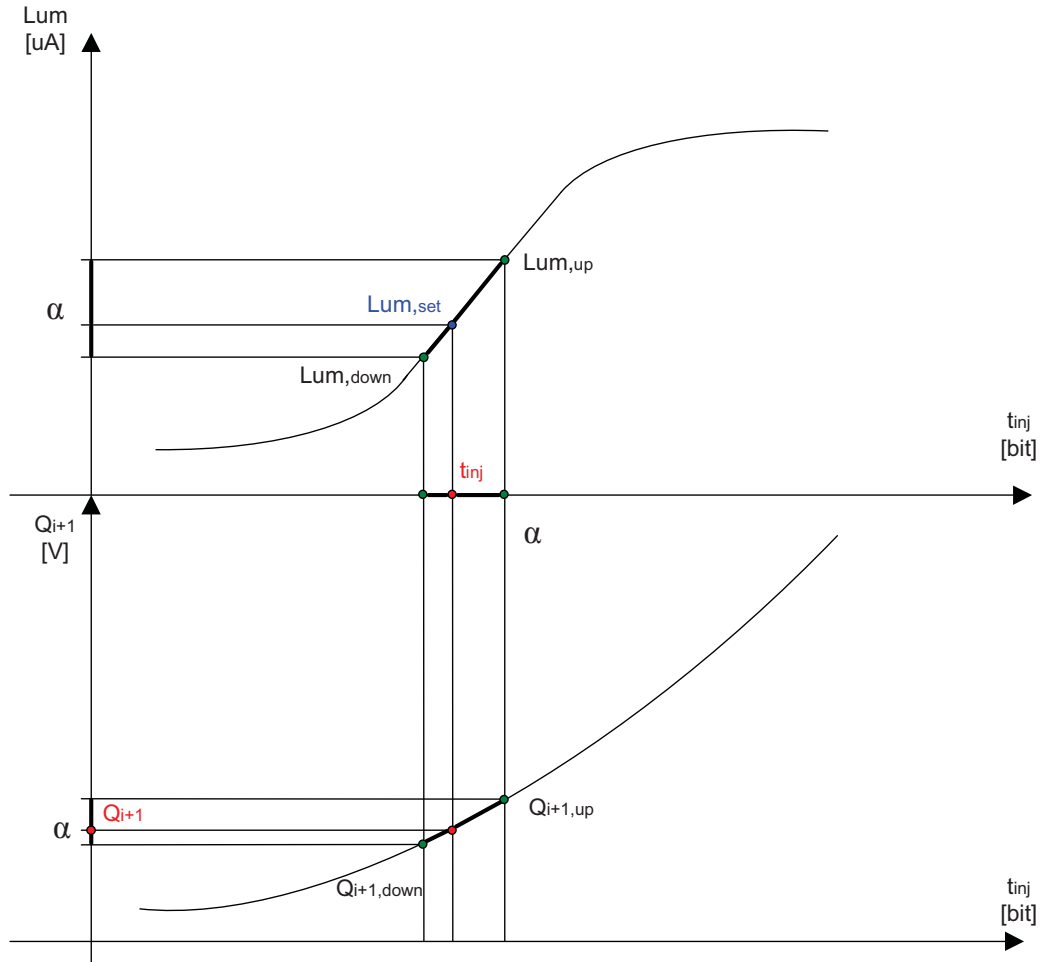
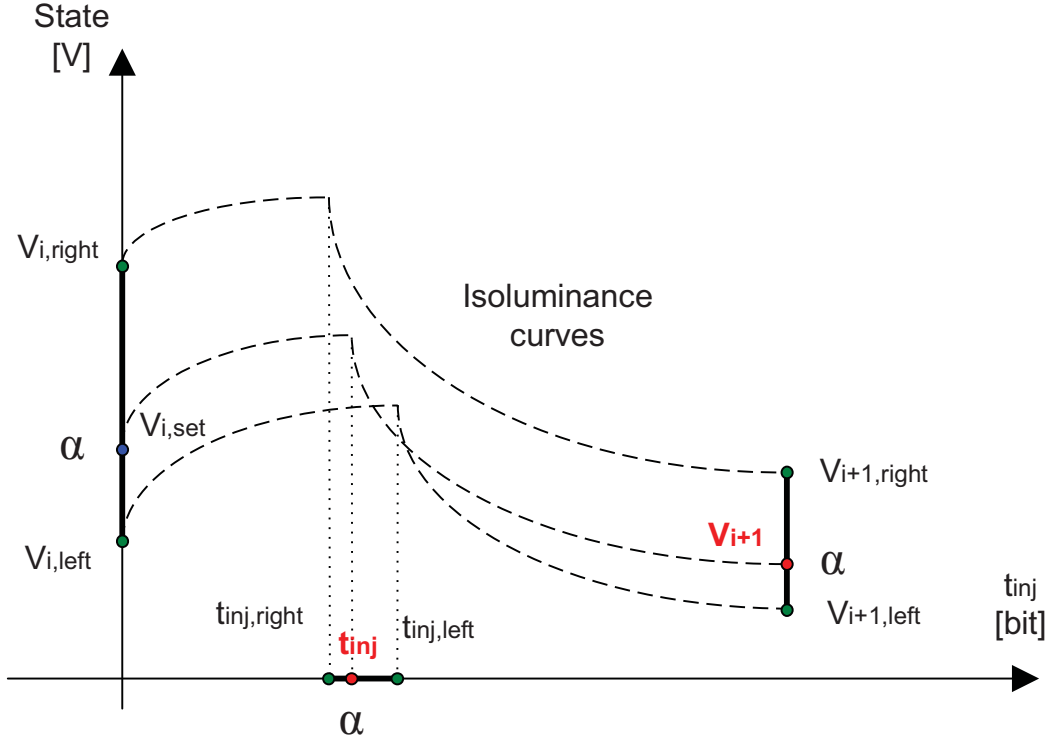


Figure 5.19: Interpolation *up-down*

The third interpolation uses as set parameter the initial state V_i and as boundary parameters $V_{i,left}$ and $V_{i,right}$. The injection time and final state are interpolated using the result of the interpolation 1 and 2. The main assumption made here is that for a given initial state the injection time situated similarly between two time boundary parameters will generate the same luminance and a final state situated similarly between two state boundary parameters. This approach is depicted in figure 5.20. The three virtual voltage waveforms can thus be considered as isoluminance curves.

Once the injection time and final state are determined, a so-called discharge test needs to be carried out. The final state thus becomes the initial state of the next

Figure 5.20: Interpolation *left-right*

pixel to be addressed. The luminance generated through natural discharge without current injection is then the minimum acceptable nominal luminance of the next pixel. Should this pixel be darker, the current pixel needs forced discharge during the reserved $3 \cdot t_{lsb}$ period at the end of its addressing sequence.

The discharge test is carried out using an interpolation settled in the first line, i.e. $0\text{-bit-}t_{lsb}$ of the 2D-LUT. For the sake of simplicity the extended 2D-LUT is used. The set parameter is the previously computed final state V_{i+1} . At first, the two boundary values $V_{i,left} \leq V_{i+1} < V_{i,right}$ are determined. The minimum luminance $Lum_{min,i+1}$ that can be potentially generated under these conditions, i.e. without injection, is then interpolated using the equation:

$$Lum_{min,i+1} = Lum_{left} + \frac{V_{i+1} - V_{i,left}}{V_{i,right} - V_{i,left}} \cdot (Lum_{right} - Lum_{left}) \quad (5.9)$$

This interpolation is graphically illustrated in figure 5.21.

If under these circumstances of no forced discharge at the end of row addressing, the minimal possible luminance of the next pixel $Lum_{min,i+1}$ is smaller than its

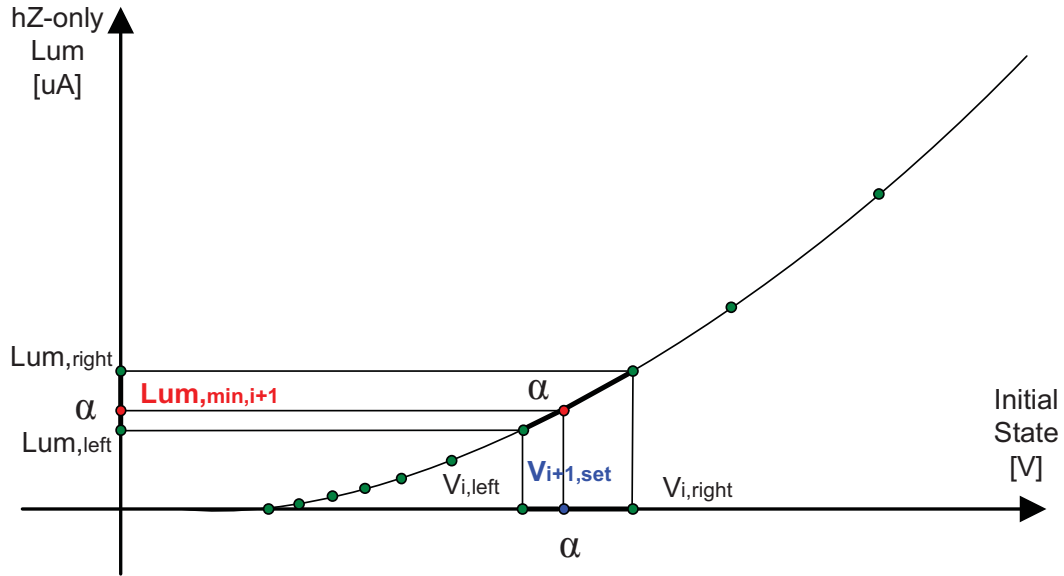


Figure 5.21: Discharge test interpolation

nominal luminance $Lum_{set,i+1}$, the algorithm stops. The resulting injection time is then used to drive the current source and the final state is taken into account for the next iteration for the subsequent pixel. If the condition is not met it means that the final voltage is too high to allow the very small nominal luminance of the next pixel by natural discharge only. In this case the first three interpolations of the algorithm are repeated using the native 2D-LUT data without the $3 \cdot t_{l_{sb}}$ extension. The new resulting injection time is used to drive the pixel, the new final state is the initial voltage of the subsequent pixel and the discharge bit for the currently processed pixel is set. The driver electronics then accordingly performs discharge at the end of the addressing sequence.

Most of the time, forced discharge is needed when the next pixel to be addressed is fully black, i.e. $Lum_{set,i+1} = 0$. Consequently, the discharge test and its consequence can often be avoided by always forcing discharge for the pixels preceding the black ones of the same column.

A pseudo-code for the 2D-algorithm is provided in listing 5.1. The next section outlines the innovative 1D-algorithm which should allow a more efficient SQC implementation.

Listing 5.1: 2D-algorithm pseudo-code

```

1 While  $V_i[index] < V_i$  Do  $index++$ 
2  $V_{i,right} = V_i[index]$ 
3  $V_{i,left} = V_i[index - 1]$ 
4
5 While  $Lum_{right}[index] < Lum_{set}$  Do  $index++$ 
6
7  $Lum_{right,up} = Lum_{right}[index]$ 
8  $V_{i+1,right,up} = V_{i+1,right}[index]$ 
9  $t_{inj,right,up} = t_{inj,right}[index]$ 
10
11  $Lum_{right,down} = Lum_{right}[index - 1]$ 
12  $V_{i+1,right,down} = V_{i+1,right}[index - 1]$ 
13  $t_{inj,right,down} = t_{inj,right}[index - 1]$ 
14
15 Interpolation #1
16  $V_{i+1,right} = \text{Interpolation}(Lum_{set}, Lum_{right,up}, Lum_{right,down}, V_{i+1,right,up}, V_{i+1,right,down})$ 
17  $t_{inj,right} = \text{Interpolation}(Lum_{set}, Lum_{right,up}, Lum_{right,down}, t_{inj,right,up}, t_{inj,right,down})$ 
18
19 Interpolation #2
20 Idem Interpolation 1 to determine  $V_{i+1,left}$  and  $t_{inj,left}$ 
21
22 Interpolation #3
23  $V_{i+1} = \text{Interpolation}(V_i, V_{i,right}, V_{i,left}, V_{i+1,right}, V_{i+1,left})$ 
24  $t_{inj} = \text{Interpolation}(V_i, V_{i,right}, V_{i,left}, t_{inj,left}, t_{inj,right})$ 
25
26 While  $V_{i+1,Z}[index] < V_{i+1}$  Do  $index++$ 
27  $V_{i+1,Z,right} = V_{i+1,Z}[index]$ 
28  $V_{i+1,Z,left} = V_{i+1,Z}[index - 1]$ 
29  $Lum_{i+1,Z,right} = Lum_{i+1,Z}[index]$ 
30  $Lum_{i+1,Z,left} = Lum_{i+1,Z}[index - 1]$ 
31
32 Interpolation #4 – discharge check
33  $Lum_{i+1,min} = \text{Interpolation}(V_{i+1}, V_{i+1,Z,right}, V_{i+1,Z,left}, Lum_{i+1,Z,right}, Lum_{i+1,Z,left})$ 
34
35 If  $Lum_{i+1,min} < Lum_{set,i+1}$  Then Break
36 Else Repeat Interpolations 1, 2 and 3 with native LUTs
37 (i.e. with no  $3 \cdot t_{lsb}$  extension)
38 End If

```

5.2.4 1D-Look-up Tables and Algorithm

The 1D-algorithm is a different implementation of the SQC driving scheme. While the 2D-algorithm was used for the proof of concept, this alternative is more innovative allowing for a simplified display characterisation and hardware implementation. The concept has been elaborated in [90] and the algorithm has been co-developed [9] and implemented in a first instance for the scope of the present work. Subsequently it has also been described, implemented and evaluated in [24]. The following description is based to a large extent on the results of that work. Nevertheless, the measurements and visual validation have been carried out upfront independently as part of this work.

In the following, the algorithm will be described first, followed by a description of the corresponding method for display characterisation.

The main scope of the 1D-algorithm is to simplify the characterisation of the display and make use of 1D-LUTs only. The fundamental principle is to decouple the injection and post-luminescence phases with one single pair of voltage and luminance curves for each. The input of both 1D-LUT pairs is time. The two phases are thus characterised and treated separately in contrast to the 2D version.

Figure 5.22 shows the four measurements required for this SQC implementation and the snapshot of one algorithm iteration [24]. The measurements are:

- $State_Inj(t)$ - the column voltage luminance during the current injection phase.
- $Lum_Inj(t)$ - the pixel luminance during the current injection phase.
- $State_Post(t)$ - the column voltage luminance during post-luminescence.
- $Lum_Post(t)$ - the pixel luminance during during post-luminescence.

The principle depicted in figure 5.11 remains valid. Based on the set luminance Lum_{set} and the initial state described by the column voltage $V_{1,i}$, the algorithm makes use of the recorded curves in figure 5.22 to compute the injection time t_{inj} and the final state, i.e. the column voltage $V_{1,i+1}$ used to process the next pixel. At the same time, the algorithm decides if there is the need to discharge the pixel or not ($dis = 1$ or $dis = 0$). One difference from the previous implementation is that the pixel luminance is processed as the sum of two parts, i.e. injection and post-luminescence:

$$Lum_{set} = Lum_{inj} + Lum_{post} \quad (5.10)$$

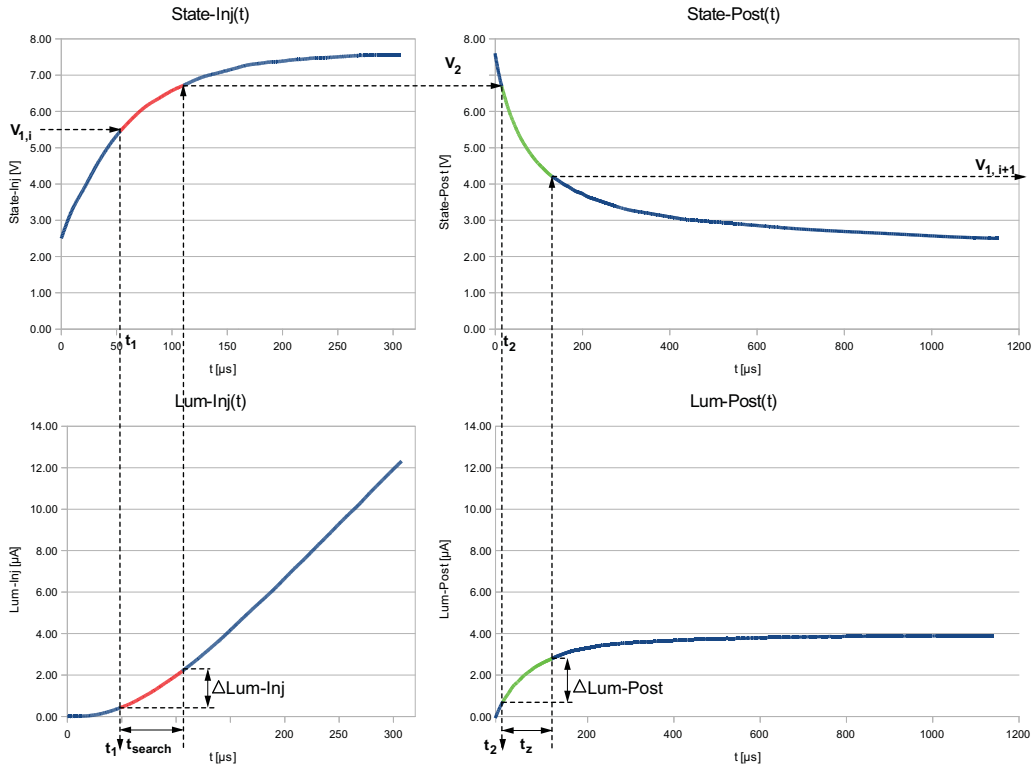


Figure 5.22: Basic principle of the 1D-algorithm and illustration of the 1D-LUTs [24]

The four 1D-LUTs are all resolved by the common variable time. The objective is to find out the injection time corresponding to a grey-value. To this end, the binary search method is applied since the four curves are all monotonic as figure 5.22 shows. Each pixel can be processed iteratively by means of binary search. It is a fast method to find an element inside a sorted array. Should the value not exist, the method delivers the closest match in the array. Figure 5.23 depicts the binary search principle. In this example the search element is located using very few iterations. In each iteration the search element is compared with the mid value of the current search range. At start, the search range is the full array interval. Depending on the result, the algorithm stops if there is a match, or shrinks the search interval to the lower or upper half of the current one and starts a new iteration. The algorithm stops at the latest when the whole search range has been passed. In this case the output is the element with the smallest deviation from the search value. The method is suitable for the 1D-algorithm implementation as both the *Lum_Inj* and the *Lum_Post* LUTs are de-facto monotonically increasing

one-dimensional arrays given the nature of the generated light (equation 4.6). The maximum number of iterations is the number of bits of the injection time or the row addressing time.

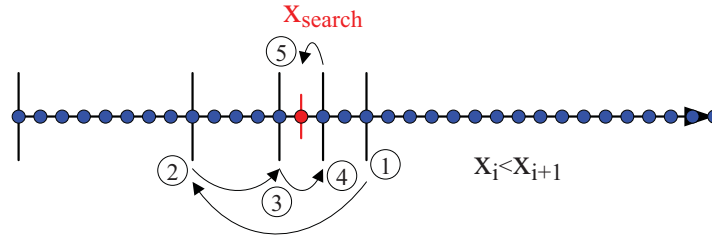


Figure 5.23: Binary search illustration

The unit of the x-axis in figure 5.22 is time. The algorithm starts by determining t_1 , which is the time that would have been needed by the anode potential to rise from a theoretical reset, i.e. the threshold voltage V_{th} to the initial state of the processed pixel $V_{1,i}$. When processing the injection time t_{search} , the starting point t_1 becomes de-facto an offset reflecting the initial state or the initial charge accumulated in the parasitic column capacitance at the beginning of the row addressing sequence. In other words, the variable initial state $V_{1,i}$ is now mapped by the time t_1 .

Only the absolute value of the state variable, i.e. the anode voltage is relevant in this SQC implementation. As addressing starts with an arbitrary initial state, i.e $V_{1,i}$ at the time-stamp t_1 in the *State_Inj* curve, it is obvious that injection spans the time axis for a duration corresponding to t_{search} and starting at t_1 . In an analogue manner, the same is true for the intermediate state V_2 and the time variables t_2 and t_z in *State_Post* accordingly.

For the recorded luminance this approach is no longer self-evident. The curve *Lum_Inj* describes the intensity of the emitted light for different injection times reflected in the measured luminance. As the photon emission is a consequence of charge recombination which is in turn proportional to the time-integral of the injection current, the curve is the time-integral of the OLED current multiplied by a proportionality factor (equation 4.6). The shape of the curve is determined by the shape of the injection current. This is obvious for the nearly linear part where the OLED pixel current is nearly constant, while at the beginning it reflects the influence of the capacitive current flow. In any case, the luminance curve is proportional to the time-integral of the injection current and the second fundamen-

tal theorem of calculus applies. This allows the computation of definite integrals, needed in this particular case to determine the quantity of light generated starting with the time offset t_1 for the duration of t_{search} . This translates into a difference of recorded values, easy to implement in hardware:

$$\begin{aligned} Lum_{inj} &= \Delta Lum_{inj} = k \cdot Q_{lum,inj} = \\ &= \int_{t_1}^{t_1+t_{search}} I_{OLED,inj}(t) \cdot dt = Lum(t_1 + t_{search}) - Lum(t_1). \end{aligned} \quad (5.11)$$

The same applies in a similar manner to ΔLum_{post} .

Starting at the initial voltage $V_{1,i}$ the green section of the state and luminance injection curves are covered during the injection time t_{search} , generating the injection luminance ΔLum_{inj} . The anode reaches at the end of the injection phase the intermediate peak voltage V_2 . Similarly, starting at the intermediate voltage V_2 reflected by the offset t_2 , the red section is covered during the duration t_z of post-luminescence. The additional luminance ΔLum_{post} is generated and the anode voltage reaches its final state $V_{1,i+1}$.

The pseudo-code of the 1D-algorithm is provided in listing 5.2. A flowchart is depicted in figure 5.24.

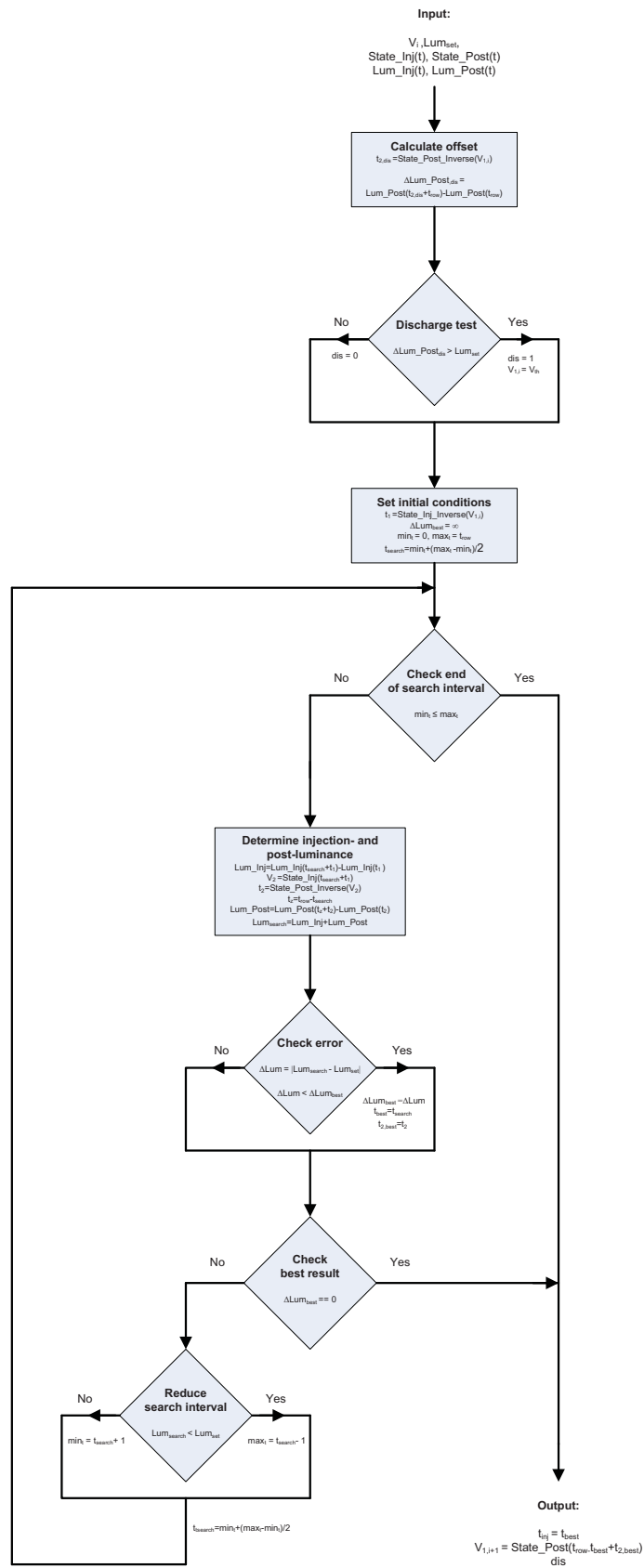


Figure 5.24: 1D-algorithm flowchart (derived from [24])

For each pixel, the algorithm determines at start if discharge is required, i.e. if the initial charge is so high, that even without current injection the post-luminescence would be higher than the set luminance. The forced discharge has been traditionally regarded as an action at the end of the addressing sequence (figure 3.11). This has added complexity to the 2D-LUT SQC implementation (section 5.2.2). Here the check is performed more intuitively at the beginning of the pixel addressing. It is important that the discharge bit is assigned properly by the driving algorithm, i.e. to the previous pixel if discharge is still performed at the end or to the current pixel if discharge is the first state of the addressing sequence.

The discharge check (line 1 to 7 in listing 5.2) is carried out by determining first the time $t_{2,dis}$ corresponding to the initial voltage $V_{1,i}$ on the $State_Post(t)$ curve. This operation is not depicted in figure 5.22 but is similar to the calculation of t_2 :

$$t_{2,dis} = State_Post_Inverse(V_{1,i}) \quad (5.12)$$

The inverse function is actually a search function inside the 1D-LUT.

By means of this initial offset $t_{2,dis}$, the algorithm determines the post-luminescence generated through natural discharge from the initial voltage $V_{1,i}$ during the row addressing time t_{row} . This is not depicted in figure 5.22 but is similar to the calculation of ΔLum_Post (equation 5.11):

$$\Delta Lum_Post_{dis} = Lum_Post(t_{2,dis} + t_{row}) - Lum_Post(t_{2,dis}) \quad (5.13)$$

If the minimal luminance ΔLum_Post_{dis} is larger then the set luminance Lum_{set} , discharge is required. The discharge bit is then set ($dis = 1$) and the initial state is reset to threshold voltage value ($V_{1,i} = V_{th}$). If not, the discharge bit is reset ($dis = 0$) and the initial voltage $V_{1,i}$ is not changed.

t_1 is determined by means of the inverse $State_Inj(t)$ LUT as a function of the initial voltage $V_{1,i}$ (line 9 in listing 5.2, figure 5.22):

$$t_1 = State_Inj_Inverse(V_{1,i}) \quad (5.14)$$

The initial values for the iteration are set (line 10 to 13 in listing 5.2) and the iteration is started (line 15 to 38).

t_{search} is being adjusted iteratively such that the corresponding luminance Lum_{search} equals or is as close as possible to the set luminance Lum_{set} . At the beginning

of each iteration it is placed in the middle of an interval and the corresponding luminance is determined Lum_{search} . At the end of the iteration this interval is adapted accordingly, i.e. it is replaced with its upper or lower half, or the sequence is stopped if Lum_{search} has reached the desired value. The initial interval is the full range from zero to t_{row} . The division by two (line 13 in listing 5.2) is easy to implement in hardware by means of a bit-shift.

At first, the luminance values corresponding to t_{search} and $t_1 + t_{search}$ are determined. The difference

$$\Delta Lum_Inj = Lum_Inj(t_1 + t_{search}) - Lum_Inj(t_1) \quad (5.15)$$

is the luminance produced during the current injection phase for the duration of t_{search} (equation 5.11). The intermediate state V_2 that settles at the end of the injection phase is determined:

$$V_2 = State_Inj(t_1 + t_{search}) \quad (5.16)$$

V_2 is then the initial state of the post-luminescence phase. t_2 is then determined similarly to equation 5.14:

$$t_2 = State_Post_Inverse(V_2) \quad (5.17)$$

In each iteration, the duration t_z of the post-luminescence phase is the difference between the constant row addressing time t_{row} and t_{search} :

$$t_z = t_{row} - t_{search} \quad (5.18)$$

With t_2 and t_z the luminance produced during the post-luminescence phase is computed similar to equation 5.15:

$$\Delta Lum_Post = Lum_Post(t_2 + t_z) - Lum_Post(t_2) \quad (5.19)$$

The luminance Lum_{search} is then the sum of the two components determined in equation 5.15 and 5.19:

$$Lum_{search} = \Delta Lum_Inj + \Delta Lum_Post \quad (5.20)$$

At the end of each iteration the absolute error of the determined luminance, i.e. the difference from the set value is computed:

$$\Delta Lum = |Lum_{search} - Lum| \quad (5.21)$$

This is then compared to the best previous result, i.e. the smallest error ΔLum_{best} from all previous iterations (line 23 to 28 in listing 5.2). If the value is smaller, the temporary best solution described by $t_{search,best}$, $t_{2,best}$ and ΔLum_{best} is overwritten by the outcome of the current iteration.

The outcome Lum_{search} is then compared to the set luminance Lum_{set} (line 30 to 37 in listing 5.2). Three cases can thus occur:

- $Lum_{search} = Lum_{set}$: the computed luminance equals the set luminance and the iteration is stopped (line 31 in listing 5.2).
- $Lum_{search} > Lum_{set}$: the computed luminance is greater than the set luminance. The variable t_{search} has to be decreased according to binary search to the mid value of the lower half of the current interval. This is realised by modifying the upper limit of the interval (line 33 in listing 5.2) and keeping t_{search} always in its middle.
- $Lum_{search} < Lum_{set}$: the computed luminance is smaller than the set luminance. The variable t_{search} has to be increased according to binary search to the mid value of the upper half of the current interval. This is realised by modifying the lower limit of the interval (line 35 in listing 5.2) and keeping t_{search} always in its middle.

Should the nominal luminance value Lum_{set} never be exactly met, the algorithm stops once the entire search interval is exhausted (line 15 in listing 5.2). The nearest value t_{best} corresponding to the smallest absolute error is then considered as solution.

The last step of this pixel processing sequence consists in retrieving the final state $V_{1,i+1}$ as a function of the determined injection time (line 41 in listing 5.2) using the *State_Post* LUT. These two values are the outcome of the computation. t_{inj} is used to drive the current pixel and $V_{1,i+1}$ in the processing of the subsequent one.

In conclusion, instead of complex 2D-LUTs, four 1D-LUTs are sufficient for determining the proper control signals by applying this algorithm.

Listing 5.2: 1D-algorithm pseudo-code (adapted from [24])

```

1   $t_{2,dis} = State\_Post\_Inverse(V_{1,i})$ 
2  If ( $Lum\_Post(t_{2,dis} + t_{row}) - Lum\_Post(t_{2,dis}) > Lum_{set}$ ) Then
3       $dis = 1$ 
4       $V_{1,i} = V_{dis}$ 
5  Else
6       $dis = 0$ 
7  End If
8
9   $t_1 = State\_Inj\_Inverse(V_{1,i})$ 
10  $\Delta_{Lum,best} = \infty$ , in practice  $\Delta_{Lum,best} =$  the highest value of the used datatype.
11  $min_t = 0$ 
12  $max_t = t_{row}$ 
13  $t_{search} = min_t + (max_t - min_t)/2$ 
14
15 While  $min_t \leq max_t$  Do
16      $Lum\_Inj = Lum\_Inj(t_{search} + t_1) - Lum\_Inj(t_1)$ 
17      $V_2 = State\_Inj(t_{search} + t_1)$ 
18      $t_2 = State\_Post\_Inverse(V_2)$ 
19      $t_z = t_{row} - t_{search}$ 
20      $Lum\_Post = Lum\_Post(t_z + t_2) - Lum\_Post(t_2)$ 
21      $Lum_{search} = Lum\_Inj + Lum\_Post$ 
22
23      $\Delta_{Lum} = |Lum_{search} - Lum_{set}|$ 
24     If  $\Delta_{Lum} < \Delta_{Lum,best}$  Then
25          $\Delta_{Lum,best} = \Delta_{Lum}$ 
26          $t_{best} = t_{search}$ 
27          $t_{2,best} = t_2$ 
28     End If
29
30     If  $\Delta_{Lum,best} == 0$  Then
31         Break
32     Else If  $Lum_{search} < Lum_{set}$  Then
33          $max_t = t_{search} - 1$ 
34     Else
35          $min_t = t_{search} + 1$ 
36     End If
37      $t_{search} = min_t + (max_t - min_t)/2$ 
38 End While
39
40  $t_{inj} = t_{best}$ 
41  $V_{1,i+1} = State\_Post(t_{row} - t_{best} + t_{2,best})$ 

```

5.2.5 1D-Display Characterisation

The measurements needed to characterise the display for the 1D-algorithm implementation are carried out using the same set-up as for the 2D-implementation (section 5.2.2). *All-on* driving of the entire display is used so that the photodiode captures a measurable signal and any variation of pixel properties is averaged out.

Two different driving sequences are used to characterise the injection and the post-luminescence phases. For each of them, the anode voltage and the luminance are recorded for different injection and post-luminescence duration respectively. They are both depicted in figure 5.25.

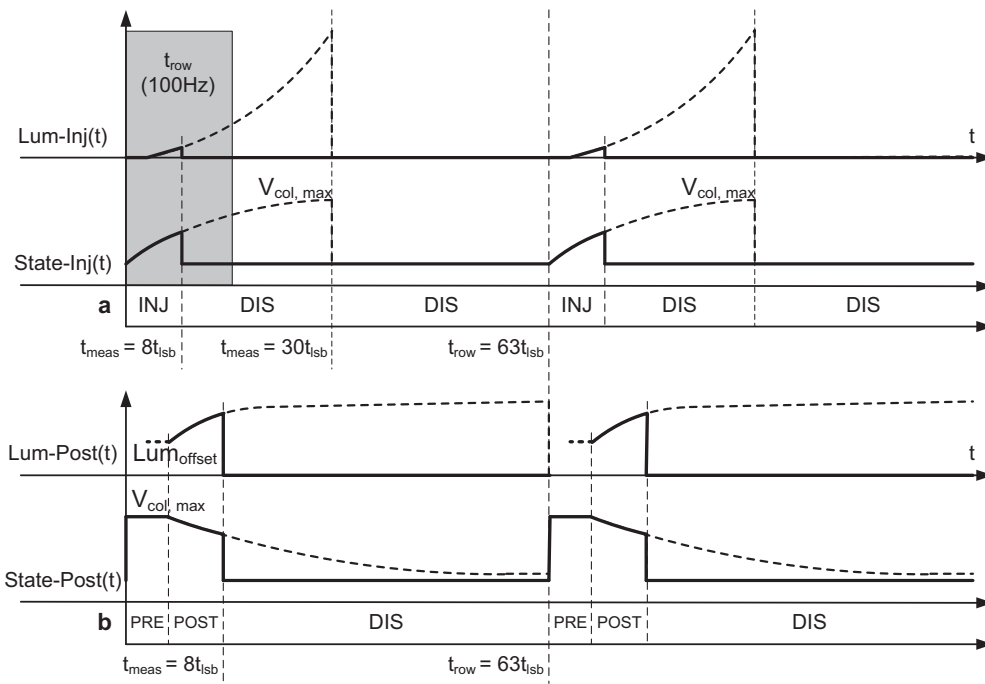


Figure 5.25: Display characterisation waveforms for the 1D-algorithm [24]

The driving sequence used to record the injection phase is similar to conventional driving with a variable current injection phase followed by immediate discharge to threshold voltage level. The driving sequence for post-luminescence characterisation consists of a voltage precharge phase, a variable post-luminescence phase and a subsequent discharge phase at threshold voltage level. During precharge the anodes are connected to an external voltage source adjusted at the maximum forward voltage level, i.e. $V_{col,max} = 7.25 V$ given by the amplitude of the constant

injection current and the diode properties.

For the characterisation process a longer row addressing time, hence a lower frame frequency must be chosen due to two reasons. On one hand, the concept requires in theory the full characterisation of both phases over the entire voltage driving range, i.e. from the threshold level $V_{th} = 2.5 V$ to the maximum forward voltage $V_{col,max} = 7.25 V$ for the injection phase and vice versa for the post-luminescence phase. While this is naturally met for the injection phase, the state curve decreases logarithmically during post-luminescence, in practice with a relatively large time constant, so that it is tending slowly to the lower limit of $V_{th} = 2.5 V$. The row characterisation time has to be extended to record this phase down to a voltage level sufficiently close to the lower limit and allow practical implementation. On the other hand, as mentioned in section 5.2.4, the algorithm starts by computing a time offset a starting point for any iteration corresponding to the initial state. As a consequence, it is not sufficient to characterise only the actual interval up to t_{row} , because with a starting point different (i.e. higher) than 0 and a relatively long injection time, the sequence of the algorithm (figure 5.22) may overshoot the *State_Inj* curve. The row characterisation time must be chosen to be sufficiently long to handle the theoretical worst case given by an initial offset $t_1 = t_{row}$ and $t_{search} = t_{inj} = t_{row}$. To satisfy the second condition, a characterisation time at least twice as long as the row addressing time must be ensured. For the present implementation with a nominal frame frequency of $90 Hz$ and 5-bit images on a 64-row display, the row addressing time is approximately $t_{row} = 174 \mu s$ with $t_{lsb} \approx 5 \mu s$ (section 5.2.2). The characterisation time is thus chosen to $t_{row,charact,inj} \approx 2 \cdot 34 \cdot 5 \mu s \approx 340 \mu s$. To satisfy the first condition in a sufficient manner, a characterisation time four times longer than the row addressing time is chosen, i.e. $t_{row,charact,post} \approx 4 \cdot 34 \cdot 5 \mu s \approx 680 \mu s$ leading to a characterisation frame frequency of $f_{charact,post} \approx 23 Hz$. Thus, the column voltage is permitted to decrease sufficiently enough, in practice down to $V_{col} = 2.8 V$. The difference to the lower limit of $V_{th} = 2.5 V$ may generate an error in theory, nevertheless this case has never occurred when processing test images as the discharge process at low V_{col} levels is very slow and the time needed to for V_{col} to drop e.g. from $2.9 V$ to $2.8 V$ is in practice very long and much longer than the addressing time.

Even though the injection phase requires half of the row characterisation time of the post-luminescence phase, it is compulsory to characterise the display at the same frame frequency for both cases. One reason is the frequency dependent

gain k of the photodiode-amperemeter sensing system. It has to be kept constant throughout the characterisation process to allow for consistent luminance readings. As a consequence, the same frame frequency of $f_{character} \approx 23 \text{ Hz}$ is assured also for the injection phase characterisation. Figure 5.25 depicts an example of waveforms driven to record the state (anode voltage) and luminance for both phases for a given injection or post-luminescence duration. The actual row addressing time and the injection characterisation range are marked accordingly.

As for the 2D-LUT characterisation, the voltage precharge needed to set the initial voltage in the post-luminescence characterisation is generating light. This offset needs to be subtracted from all subsequent measurements taken with a variable post-luminescence duration.

$$Lum_Post[0] = Lum_{offset} \geq 0 \quad (5.22)$$

$$Lum_Post[i] = Lum_Post[i] - Lum_{offset} \quad (5.23)$$

$$i \in [0, 126]$$

Similarly, the recording of the data-points is not equidistant. More measurements are made in the lower part of the curves to account for their non-linearity while in the upper more linear part a coarse measuring interval is sufficient. Nevertheless, to be able to compute arbitrary injection times and final states, the algorithm starts by interpolating the available measurements to ensure a sufficient resolution of the time axis.

In conclusion, two algorithms have been elaborated to demonstrate the SQC driving scheme. In spite of its complexity requiring 2D characterisation look-up tables and many interpolations, the first algorithm has been successfully used as a proof of concept. The second algorithm is innovative and considerably reduces the computation and display characterisation effort. It will be used further for visual validation and benchmarking.

6 Prototyping and Visual Validation

6.1 SQC Demonstrators

Two discrete demonstrators are developed to validate and benchmark the SQC driving scheme against the state of the art. This would not have been possible with commercial integrated drivers due to the limited access to direct anodes and cathodes driving signals as well as restricted driving patterns and electrical control parameters. The demonstrators are also used to characterise the OLED displays and generate the required look-up tables (section 5.2).

The demonstrators have an FPGA as digital controller and PCB based driver electronics to generate the appropriate currents and voltages for the PMOLED display anodes and cathodes.

FPGA-based designs are chosen to mimic as much as possible integrated driving chips. For the sake of simplicity they serve however only for the proof of the SQC concept and do not run SQC algorithms on-chip. The algorithms are computed in Matlab (section 5.2) and generate for each pixel the injection time and a discharge bit. Hence, the FPGA receives pre-computed image data to control the drivers accordingly. Section 8.2 recalls a subsequent integration concept with an on-chip algorithm [24].

The CAE tool *Eagle* [25] is used for schematic design and board layout. Xilinx *Modelsim* [80] is used for digital design and simulation. Xilinx *ISE Design Suite* [81] is used for synthesis and FPGA programming.

The main requirements for the choice of the FPGA hardware are:

- sufficient number of generic I/Os to control the display anodes and cathodes
- sufficient memory blocks (Block RAM) to store the data for at least one image
- the availability and affordability of an appropriate FPGA development board.

The driving electronics require several power supplies to implement and test the various driving schemes. They are made available off-board by means of external adjustable voltage sources as follows:

- supply voltage for the on-board anode constant current sources, level shifters and inverters - $V_{cc} : 14 V$
- gate drive voltage to set the OLED constant current amplitude - $V_{gate} : 8 V .. 10 V$
- cathodes common off voltage, level shifters and inverters supply - $V_{comh} : 8 V$
- precharge voltage - $V_{pre} : 0 V .. 8 V$
- discharge voltage - $V_{dis} : 0 V .. 3 V$

The supply of $14 V$ is needed for the current source transistors to operate in the saturation region and generate a constant current of $330 \mu A$ setting an OLED forward voltage of ca. $7.25 V$.

The $3.3V$ logic voltage of the FPGAs and level shifters is supplied by the FPGA development board power adapter.

The simplified schematic of the driving circuitry is depicted in figure 6.1. The two main blocks are the anodes and cathodes driver circuitry.

The main component of the anodes driver is the constant current source. It has been realised with pmos transistors and a basic current feedback circuit with one resistor [74]. The amplitude of the constant current is set by the values of the supply voltage V_{cc} , the gate voltage V_{gate} , the feedback resistor R_{fb} and the threshold voltage of the transistor. It is determined sufficiently precise with the formula:

$$I_0 \approx \frac{V_{cc} - (V_{gate} + V_{th,pmos})}{R_{fb}} \quad (6.1)$$

The constant current amplitude is set empirically to a value allowing in time-multiplexing an appropriate maximal brightness.

Apart from the adjustable supply voltages, the precision of the feedback resistor and the pmos threshold voltage determine the accuracy of the current amplitude. Thus, high precision 0.1% feedback resistors are used. They were delivered from the same production batch and were expected to have little deviation in their threshold voltage. The threshold voltage has been measured for several samples of the delivery roll and the values lie between $1.339 V$ and $1.366 V$. With R_{fb}

theoretically varying from $8.052\text{ k}\Omega$ to $8.068\text{ k}\Omega$ and the supplies set to $V_{cc} = 14\text{ V}$ and $V_{gate} = 10\text{ V}$, the oled current amplitude range is expected to be from $326\text{ }\mu\text{A}$ to $330\text{ }\mu\text{A}$. This variation is similar to the one of the current sources of an integrated driver. No differences in luminance have been visually perceived between identically driven display columns, neither at a high or a low nominal luminance.

For convenience, the nominal value of the current amplitude is thus defined as $I_0 = 330\text{ }\mu\text{A}$ and is given by the parameters $V_{cc} = 14\text{ V}$, $V_{gate} = 10\text{ V}$, $R_{fb} = 8.06\text{ k}\Omega$ and $V_{th,pmos} = 1.35\text{ V}$.

Two further identical feedback resistors can be individually switched in parallel to the nominal one by means of analogue switches. The two, three or fourfold OLED current amplitude can be thus digitally set in a fast and simple manner. This capability is compulsory for the implementation of multiline addressing [87] and is also used in [24] to realise a faster current precharge.

The OLEDs are controlled by means of pulse-width modulation and the constant current sources have thus to be switched on or off according to the programmed duty cycle. The gates of the pmos-based current sources have to be switched either to V_{gate} (on) or V_{cc} (off) accordingly. The FPGAs have I/O logic HIGH values of 3.3 V or 5 V and cannot drive the pmos-gate of the current source directly. By means of a level-shifter and an inverter shown in figure 6.1, the FPGA control signals are shifted to the required gate voltage levels to activate the current source with a logic *high* signal and turn it off with logic *low*.

Analogue switches are connected to each anode line to charge it to an externally adjustable potential in a controlled manner. Voltage precharge or discharge (section 4.1.1) is thus realised.

The role of the cathode driver is to switch the active row(s) to ground and lift the inactive ones to a potential ($V_{comh} = 8\text{ V}$) higher than the forward voltage of the OLEDs, so that they are reverse biased and do not produce any light (section 3.4). This is realised in a similar manner to the anode driver, using a level shifter in conjunction with an inverter shown in figure 6.1. The inverter is the actual driver to sink or source the necessary cathode current. A logic *high* signal activates the row and the *low* signal turns it off.

The analogue demonstrator boards are build modularly to allow the reuse of board designs and facilitate transportation, debugging and re-working.

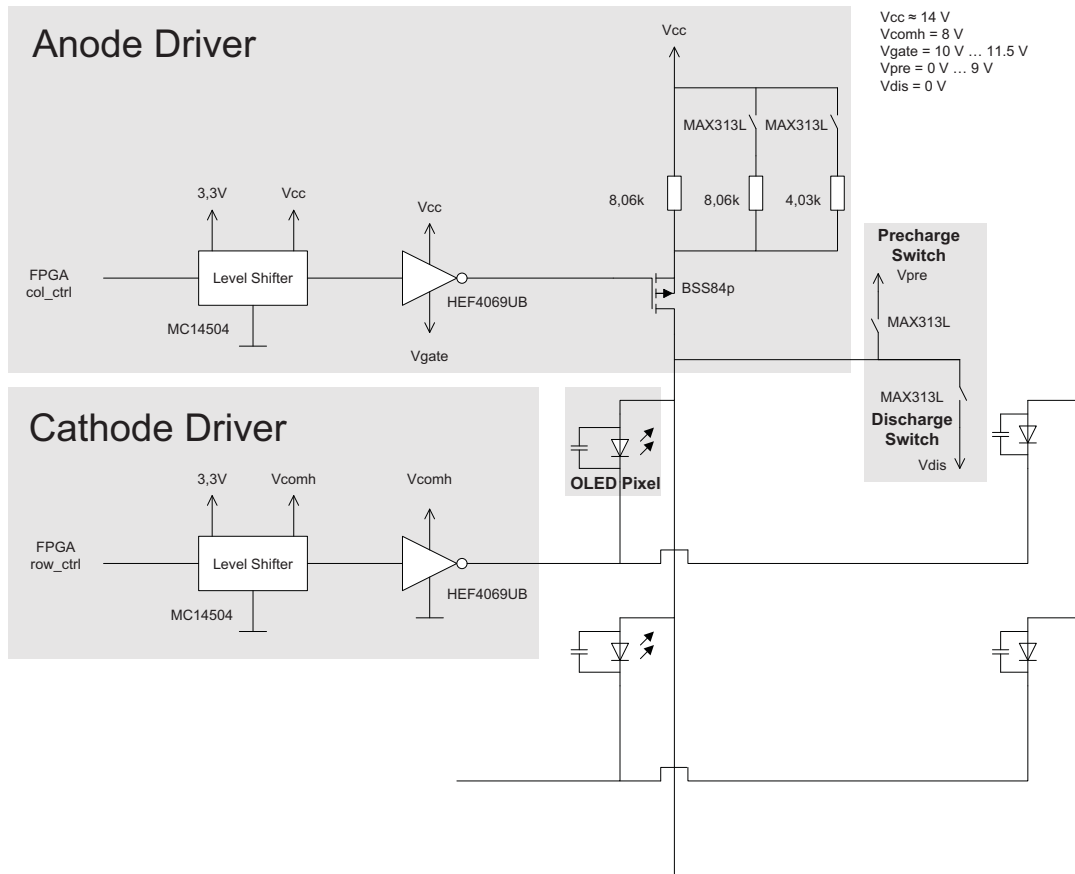


Figure 6.1: Simplified demonstrator schematic

6.1.1 The Spartan Demo-board

In a first instance, a demonstrator is build using the Digilent *D2-FT System Board* [23] with a Xilinx *Spartan IIE* FPGA [84] as digital controller. 172 generic I/Os and 64 kbit of block RAM are available.

It is designed to address 96 columns and 64 rows of the available 128 x 64 PLED displays. The multiple of four is convenient for the use of modular anode and cathode driver boards. Four of the the remaining 12 generic I/Os are used to control the global voltage discharge, precharge and current multiplication.

The size of the Block RAM allows to store at runtime one 96 x 64 image with a maximal resolution of 10 bits or 9 bits plus 1 discharge bit for the SQC implementation.

The on-board 50 MHz system clock is used, as it is fast enough to access the

6 Prototyping and Visual Validation

image data from the RAM blocks and generate 100 Hz flicker-free images.

Figure 6.2 depicts the assembled *Spartan* demonstrator. It has a modular design and consists of:

- the Digilent FPGA development board with a *Spartan IIE* FPGA,
- five identical level-shifter boards for 32 control signals each, three for the anodes and two for the cathodes,
- one control board for global precharge, discharge and the current multipliers,
- four identical stacked driver boards, each for 24 columns and 16 rows, containing the current sources, the current multipliers and the voltage precharge and discharge switches,
- one display adapter board with Zero-Insertion-Force (ZIF) connectors,
- one raw 128 x 64 PLED Display (Osram 1.6") with flexible connectors, restricted to reproduce 96 x 64 images.

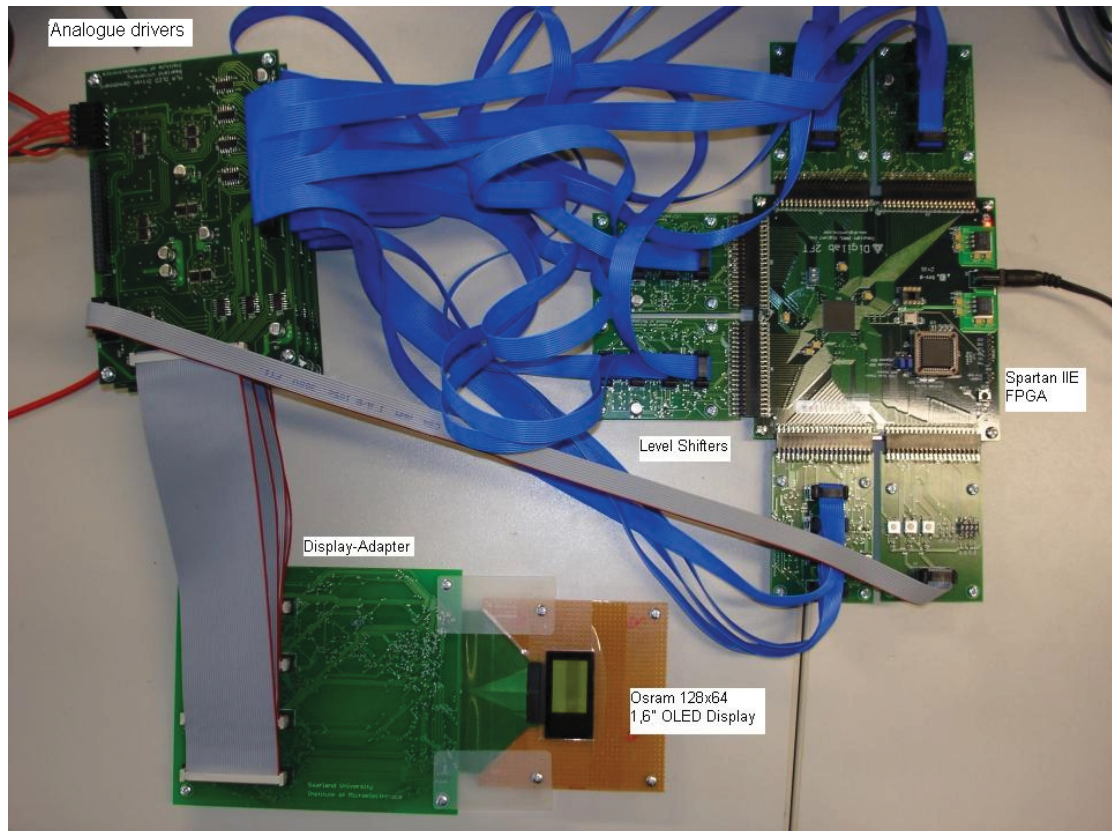


Figure 6.2: The *Spartan* demonstrator

One advantage of the *Spartan* demonstrator is the short FPGA configuration

time allowing rapid testing. Current multipliers facilitate the implementation of multiline addressing schemes. The anodes can be individually set in constant current or high-impedance mode and can be globally driven at different precharge and discharge voltages during the same pixel addressing time. This makes the demonstrator particularly suitable for display characterisation as required by the SQC algorithms. The form-factor of the display adapter boards is relatively small and the overall cost of the boards, the components and especially the FPGA and its development board is relatively low. A replica was therefore chosen to be used by students as demo-board in a digital design lab.

At the same time, the number of I/Os and the Block RAM size allow only for relatively low resolutions and for a single global discharge control signal. The latter prevents the board from implementing the SQC driving scheme that requires individual discharge capability for each anode. The boards are connected with many ribbon cables of different sizes such that assembling and transportation are cumbersome. Last but not least, the level shifter is the actual row driver. Its limited current sinking capability constrains the size of the display and the amplitude of the OLED current. On these grounds, a larger demonstrator is designed and built.

Figure 6.3 shows a test image generated by the *Spartan* demonstrator on the 2.7" Osram *Calgary* PLED display.

6.1.2 The Virtex Demo-board

Since the size and the resolution of displays has been increasing, a second larger demonstrator is developed. It is a more efficient vehicle for testing and demonstration purpose, in particular as the benefit of SQC for larger displays is more significant. This prototype is depicted in figure 6.4 and has the same basic circuitry as described in figure 6.1. It also has a modular design consisting of:

- a powerful *Virtex-5* FPGA [85] with 1200 I/OS and 10Mbit Block RAM which is embedded in a versatile FF1760 Prototyping Platform [82],
- a routing and interface board providing access to 780 control signals (two connectors of the interface board were not used),
- four identical analogue driver boards for 192 anodes and 128 cathodes overall, including level shifters,

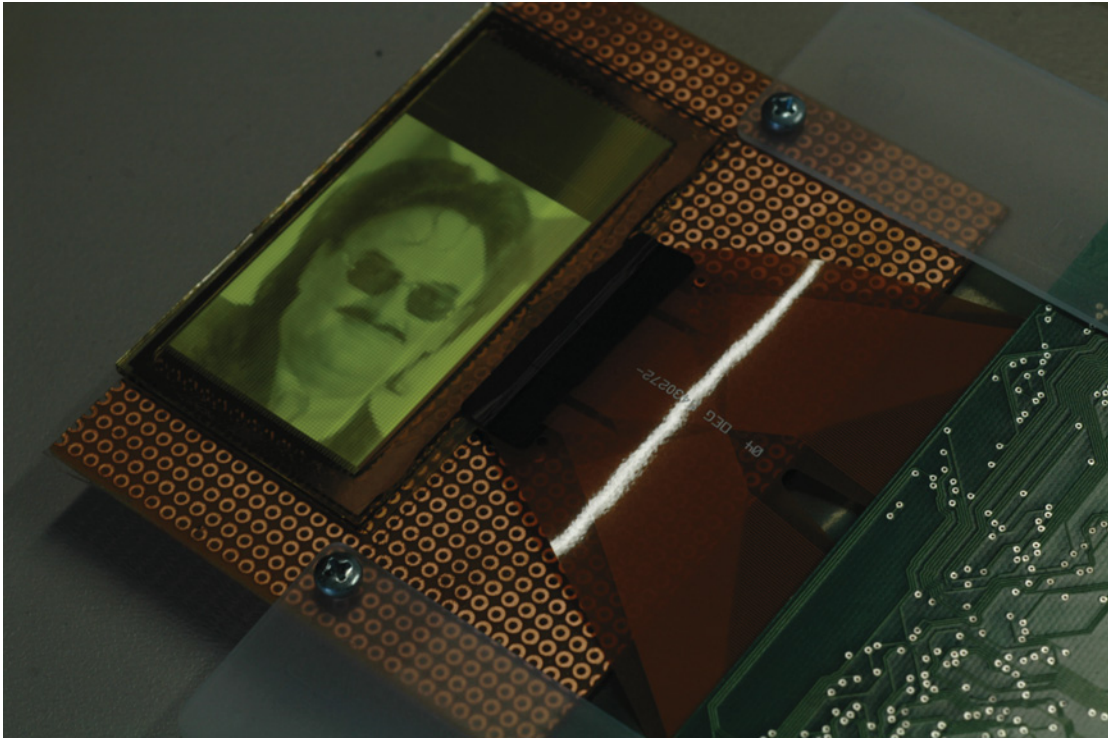


Figure 6.3: Test image generated with the *Spartan* demonstrator

- a display interface board with two ZIF connectors,
- two blank OSRAM *Calgary* 2.7" monochrome 128 x 64 OLED displays with flexible connectors. They can be driven simultaneously with two different driving schemes.

The above configuration of two parallel 96 x 64 drivers is chosen to keep the image size and aspect ratio used in the digital designs of the *Spartan* demonstrator and to minimise the number of the analogue driver boards. At the same time, displaying simultaneously two identical images driven with different driving schemes allows for a better assessment of differences in image perception. The individual current consumption can be also simultaneously recorded and compared.

In contrast to the previous demonstrator, this larger one can drive higher resolution displays and store much larger image data on the internal Block RAM. The main difference is the implementation of individual discharge per anode required by the SQC driving scheme. For each anode two control signals are thus needed, one for the constant current source and one for the discharge switch. Each anode can be thus set individually into one of the three states: constant current, high-impedance or discharge (i.e. constant voltage). Furthermore, the current

multiplication is controlled in groups of three consecutive anodes, allowing the separate control of the three colours red, green and blue for RGB displays. This feature was mainly realised to satisfy the requirements of multiline addressing [87].

The row drivers are realised with discrete pmos and nmos transistors to allow for a better current sourcing and sinking capability.

The demonstrator consists of stackable boards and no longer uses ribbon cables. It is thus easier to assemble and transport, it is more robust and has higher reliability.

One of the drawbacks of this demonstrator is the considerably longer FPGA configuration times. Moreover, the employed Xilinx FPGAs use volatile SRAM cells and keep their configuration only as long as power is supplied. To avoid configuring them each time on start-up, one can make use of the serial Config PROM. The one available on the *FF1760* development board is however too small, so that the design of a properly dimensioned Config PROM board was necessary.

Only one analogue switch per anode is designed to drive it at a constant voltage. The main reason is to reduce complexity, size and cost. Moreover, this circuitry is sufficient to implement the SQC driving scheme that requires individual discharge capability. Nevertheless, if the anodes need to be driven sequentially at two different voltage levels during the pixel addressing time, e.g. for display characterisation, requiring a precharge and a discharge level, this could be realised by means of an external digitally adjustable voltage regulator.

The demonstrator overall is versatile but relatively costly, especially due to the large FPGA and its development platform.

6.1.3 The PC Interface

Once the FPGA is configured, the demonstrators can be controlled with a PC using a graphical user interface (GUI) developed in Visual C++. The corresponding FPGA design and the GUI itself are conceived as flexible as possible to allow several settings. The main functions of the GUI are:

- uploading a series of test images. For each image, the raw 5-bit and the SQC data are transferred,
- selecting the driving scheme to be applied: conventional, *hZ* or SQC,
- uploading the linearisation tables for standard and SQC driving,



Figure 6.4: The dual *Virtex* demonstrator

- displaying a slide-show with the uploaded images,
- setting the t_{lsb} and discharge duration,
- a debug mode to send specific commands.

The serial RS232 COM Port of the PC is used for the data transfer. A transceiver interface board is built to match the FPGA digital UART signals to the RS232 input/output levels.

6.1.4 Generation of Digital Control Signals in VHDL

Several digital designs are implemented to display and evaluate images with the *Spartan* and the *Virtex* demonstrators. They all follow the generic structure depicted in figure 6.5.

The main digital blocks are: a central FSM controller, 96 individual column controllers, three RAM blocks with the raw and SQC image data, two linearisation arrays for the conventional and *hZ* driving schemes and the UART I/F for the PC downstream link.

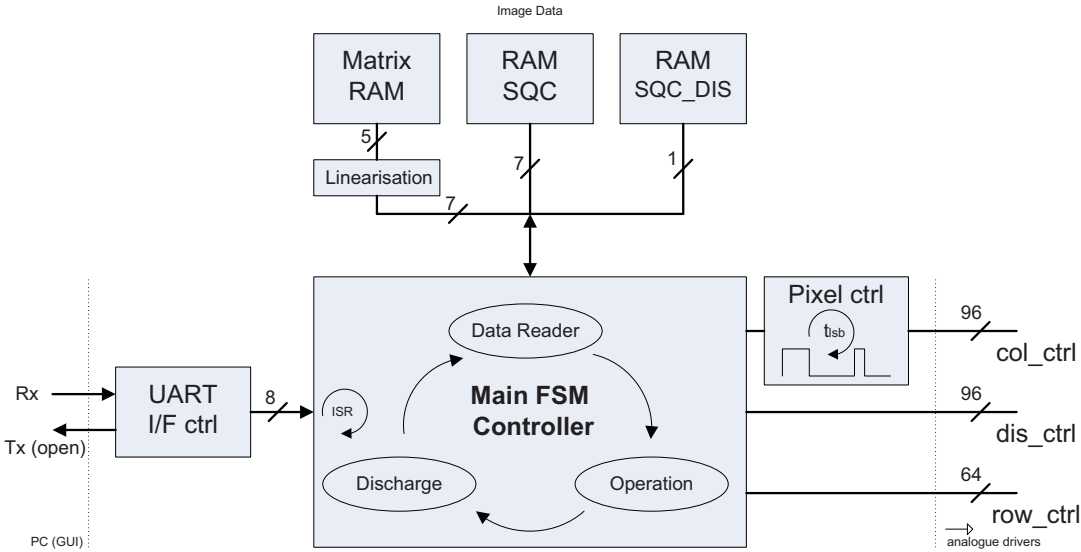


Figure 6.5: Digital design functional diagram

The main FSM controller is the core of the digital driver and has three basic states: it reads sequentially from the RAM blocks the 96 5-bit pixel brightness values of the row to be addressed and stores them into a one-dimensional data array, it loads the individual column controllers with this data and enables their lsb-clock to generate the desired anode PWM waveforms. Once the row addressing time is over, it enables the discharge counter and drives the discharge signals for all 96 anodes individually, depending on the driving scheme.

The main FSM also controls the row drivers. A numeric variable is incremented each time a new row is addressed, and is converted into an output driving vector enabling the addressed row and disabling the rest.

This block carries out further generic functions. It is linked to the UART I/F controller and can receive commands or data from the PC interface. It runs one of the three driving modes - conventional, *hZ* or SQC and selects the appropriate linearisation vectors. Upon request it updates the linearisation vectors with new external values or writes new raw and SQC image data into the three Block RAMs. It can adjust the t_{lsb} and thus the frame rate or the duration of the discharge cycle.

The column controller FSM is instantiated for all 96 anodes to be controlled. It has a register for the pwm duration corresponding to the pixel brightness and a counter running at the t_{lsb} pace. Once the values of the 96 pixels have been read

by the main FSM from the Block RAMs, they are loaded into the register and the t_{lsb} clock is enabled. Each anode control signal is then enabled and the constant current source is turned on as long as its PWM counter is running. Once an individual counter stops, the corresponding control signal is disabled. For the remaining row addressing time, the state of the anode depends on the driving scheme. For the standard driving scheme the anode is switched to ground by the individual discharge signal, while in the case of hZ or SQC driving the anode is left open.

Three Block RAMs are instantiated for each test image to make available the 96 x 64 data for implementing the three driving schemes. One Block RAM stores the raw 5-bit image values. Applying one of the two linearisation functions, conventional or hZ driving can be implemented by the main FSM. A further Block RAM stores the 7-bit SQC data and a third one the 1-bit individual discharge information. Both are used to implement SQC driving.

Synchronous single-port RAM blocks are used [85]. A *write-enable* bit controls the type of the operation to be performed. In read mode, for each clock edge, the value of the cell addressed in the address port *addr* is available at the *dout* output. In write mode, for each clock edge, the cell addressed in the address port is written with the value of the *din* input. The main FSM controller keeps track of the address range by means of the address counter that is incremented with each pixel value which is read or written.

The read operation is performed row by row and is thus very fast. It requires 96 system clock cycles which is important to bias as little as possible the driving sequence. The latter can be kept simple by always running sequentially the three states: data reading, operation and discharge. If data reading takes longer, due to longer read times and a larger number of values to read - which is usually the case for commercial drivers and high display resolutions - its implementation can be paralleled and carried out e.g. during the operation and discharge time. Their duration has usually a different order of magnitude, unless discharge is fully avoided and the operation time is zero due to a completely black row.

The default image is defined at design time when the block RAM is instantiated by uploading coefficient *coe* files. They contain a continuous vector with 96 x 64 values in hexadecimal format. Grey-scale JPEG pictures are used. The 5-bit conversion and coefficient file generation was realised in Matlab [67].

The UART I/F controller is based on an open-source module [11]. It communicates with the PC RS232 interface via the graphic user interface described in section 6.1.3. A downlink is implemented for the PC to send commands and data to the digital driver, however without any feedback mechanism. The link is stable, also for transmitting larger image data. This implementation is thus sufficient for testing, debugging and demonstration purposes. Each time when data are received, the controller generates an interrupt so that a simple Interrupt-Service-Routine (ISR) handles the transmission. The main FSM controller can then select the driving scheme, write the image data into the Block RAMs or adjust the linearisation vectors, the t_{lsb} or the discharge duration. During an UART ISR the driver is set on hold and no image is generated.

6.2 Measurements and Visual Perception

For the purpose of this work the outcome of the SQC algorithm is tested with a set of 36 mixed 96 x 64 5-bit grey-scale still images, 18 natural images and 18 graphics, displayed with a frame rate of 90 *Hz* and a single overall brightness level. The format of the source files is grey-scale JPEG with a native resolution of 8-bit, down-converted to 5-bit in Matlab before SQC processing.

The images are displayed with the *Virtex* demo-board (section 6.1.2) and are recorded with an SLR camera allowing for a sufficient exposure time. For this reason and to assure positioning consistency, the camera was mounted on a test fixture.

As outlined in section 6.1, SQC processing is carried out upfront in Matlab, the computed injection times are uploaded using a graphical interface and the FPGA generates the anodes, cathodes and discharge control signal to operate the driver.

To allow for a real-time perception and comparison of SQC with conventional driving, the driver makes use of the dual display capability. Each test image is displayed simultaneously with conventional and SQC driving. The display supply current and the discharge current are measured and recorded accordingly.

The SQC concept has been initially validated with the 2D-algorithm (section 5.2.3). As the 1D-algorithm (section 5.2.4) produces identical image quality and efficiency gains, only the 1D-version is used for further measurements and visual

benchmarking. The outcome of *hZ* driving is also not discussed further, as it has been only an intermediate stage in the SQC development. Moreover, as no difference has been visually perceived between SQC and conventionally generated images, only the former are recorded and compared further with their source. For the former, only the current consumption is measured.

Figure 6.6 shows the recorded SQC test images and their sources. The measurement results are provided in table 6.7. To better assess the image quality, two of the test images, one natural image and one graphic, are zoomed and depicted in figure 6.8. Natural images are reproduced with a very high visual quality. The quality of the graphics is also very good. A slight loss in detail for low grey-value pixels, visible for example among the corner triangles of the detailed graphic in figure 6.8 could be explained by the use of a very low grey-scale resolution, i.e. 5-bit. Increasing the number of control bits is expected to improve furthermore the visual quality.

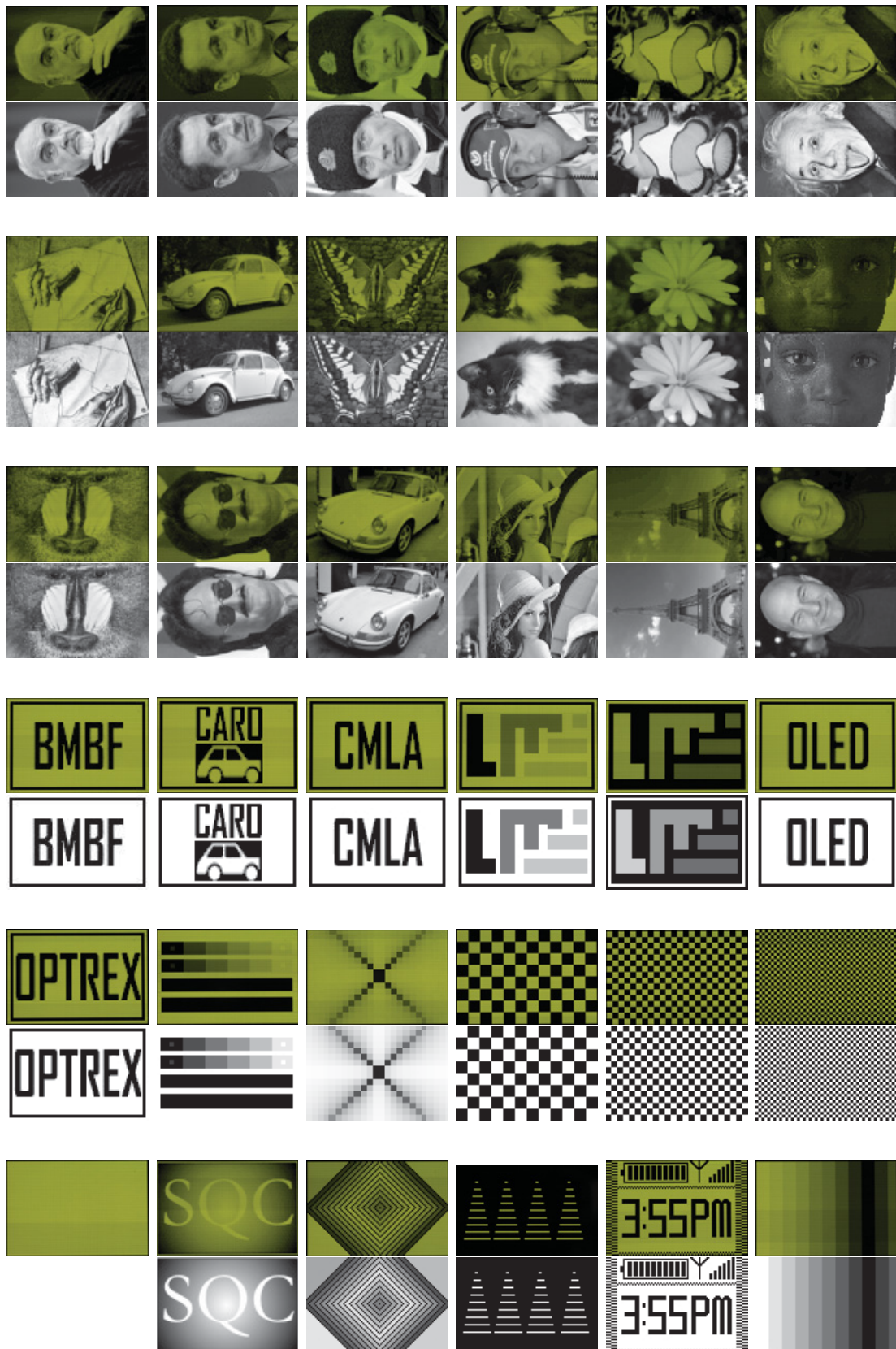


Figure 6.6: Recorded SQC test images (top), jpeg sources (bottom)

6 Prototyping and Visual Validation

dual 96x64 Demo f ~ 90 Hz									
	Conventional		SQC		Saving measured	Matlab	Discharge	Statistics	
Image	lcc(mA)	ldis(mA)	lcc(mA)	ldis(mA)	%	%	%		
								Sum Pictures SLA	300,40
00 sean connery	14,51	8,45	5,95	0,055	58,99	59	14,97	Sum Pictures SQC	125,60
01 sarkosy	15,18	9,55	5,56	0,01	63,37	64	0,33	Saving Pictures %	58,19
02 putin	16,69	9,42	7,19	0,05	56,92	57	3,16		
03 schumi2	18,74	10,38	8,35	0,06	55,44	56	3,08	Sum Graphics SLA	329,39
04 fish	16	8,66	7,24	0,1	54,75	55	17,32	Sum Graphics SQC	187,97
05 einstein	18,12	10,03	7,96	0,03	56,07	56	1,01	Saving Graphics %	42,93
06 escher	22,22	11,2	11,02	0,002	50,41	51	0,02		
07_vw_kaefer	16,45	9,52	6,92	0,075	57,93	58	2,38	Sum SLA	629,79
08 schmetterling	15,47	9,6	5,7	0,01	63,15	64	0,2	Sum SQC	313,57
09 katze	17,48	9,76	7,58	0,01	56,64	57	0,21	Saving total %	50,21
10 blume	17,14	9,61	7,36	0,03	57,06	57	3,92		
11 face1	13,55	9,7	4,34	0,015	67,97	68	0,5		
12 face3	18,03	10,42	7,5	0,005	58,40	59	0,03		
13 mosi	15,91	9,45	6,27	0,002	60,59	61	0,36		
14 porsche	17,09	9,4	7,58	0,1	55,65	56	10,68		
15 lena	18,64	10,3	8,24	0,035	55,79	56	1,32		
16 eiffel tower	17,22	10,3	6,74	0,01	60,86	61	0,05		
17 patrick stewart	11,96	7,65	4,1	0,04	65,72	66	8,94		
19_graphic_bmbf_rahmen	21,51	9,12	12,49	0,34	41,93	42	27,95		
23_graphic_caro_rahmen	20,71	8,62	12,16	0,395	41,28	41	32,62		
27_graphic_cmla_rahmen	21,97	9,22	12,83	0,27	41,60	42	26,6		
35_graphic_lme_rahmen	21,15	9,45	11,76	0,24	44,40	45	22,05		
37_graphic_lme_inv_rahmen	10,38	5,1	5,29	0,29	49,04	49	57,96		
38_graphic_oled_rahmen	22,25	9,3	13,03	0,3	41,44	42	25,96		
43_graphic_optrex_rahmen	20,08	8,35	11,76	0,33	41,43	42	34,08		
46 contrast	17,97	7,95	10,04	0,225	44,13	44	35,11		
47 cross	25,3	11,63	13,66	0,022	46,01	46	0,39		
48_checkerboard8	14,61	5,63	8,89	0,44	39,15	39	56,25		
49_checkerboard4	14,61	5,67	9,36	0,85	35,93	36	62,5		
50_checkerboard2	14,62	5,77	10,22	1,54	30,10	30	75		
51_all_on_31	28,87	12,25	16,75	0	41,98	42	0		
55_SQC	19,77	10,6	9,03	0,02	54,32	55	0,68		
66_muri2	17,6	8,95	9,2	0,9	47,73	48	37,24		
67_ct2a	1,69	0,63	1,49	0,475	11,83	11	100		
69_pm	19,09	7,76	12,33	1,32	35,41	46	49,63		
71_grey2	17,21	9,2	7,68	0	55,37	56	9,38		

Table 6.7: SQC measurement results

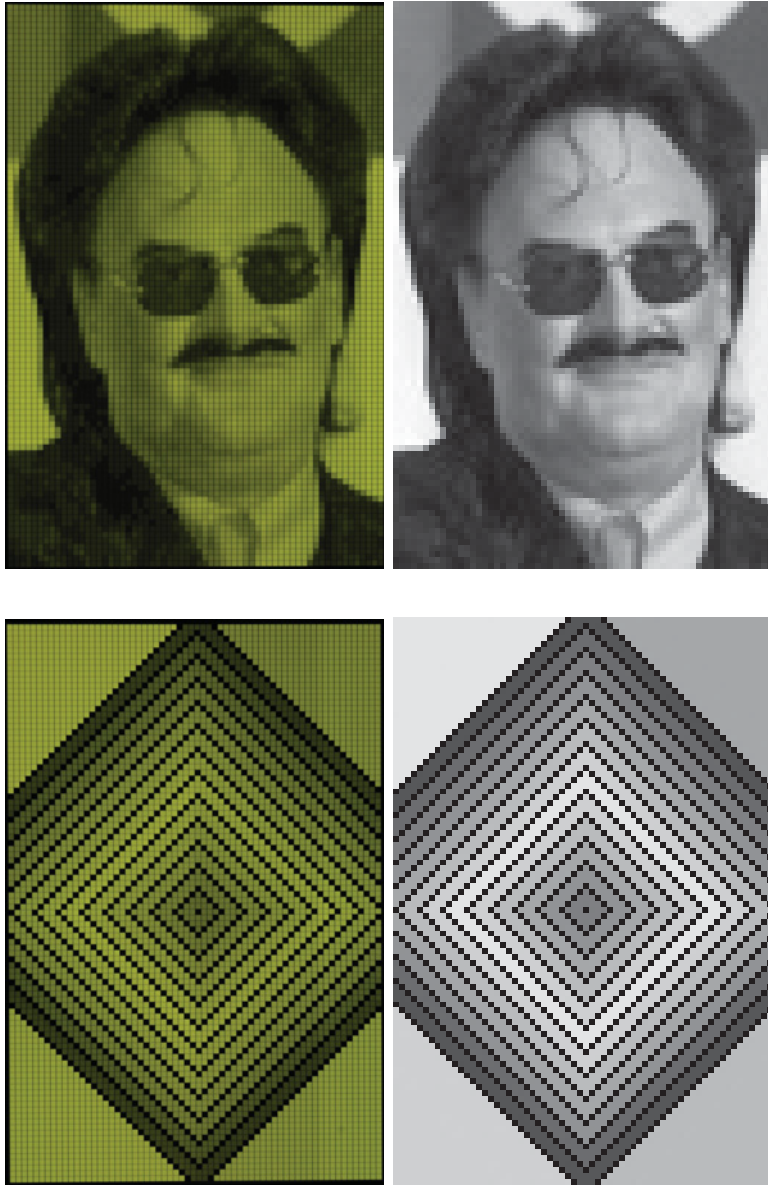


Figure 6.8: Recorded SQC test images (left), 5-bit sources (right)

An average power saving rate of ca. 50% with respect to conventional driving is measured for this set of test images. The figure is higher, i.e. ca. 58% for the subset of natural images, and lower, i.e. ca. 43% for graphics. This can be explained by the higher number of black pixels and in particular of transitions from very bright to very dark neighbouring pixels in graphics. A black pixel does not allow (local) power saving as illustrated in figure 5.9. Furthermore an extreme transition within one column from a full-scale bright pixel to a black one is usually not possible by natural discharge only and requires local discharge which in turn impacts the efficiency. For each image, the discharge current is recorded as well, reflecting this findings.

The histogram of the whole set is depicted in figure 5.10. It is the same set used in the analytical estimation of the average power saving rate in section 5.1.3. The estimated theoretical improvement of only 43% could be justified by the approximation in the definition of the ideal transfer curve.

Table 6.7 shows also the estimated power saving rate for each test image, by summing up and dividing the total injection times of SQC and conventional driving. A very good match between measurement and Matlab estimation is noted. Furthermore, the figure representing the share of discharged pixels in one picture follows the trend of the measured discharge current. There is no proportionality between the discharge current and the percentage of discharge pixels because each discharge operation is counting binary for the percentage and does not reflect the quantity of the energy lost. The latter could be quantified only through the remaining charge from the previously addressed pixel. For the selected set of test pictures, discharge is needed in average for 4.28% of the pixels of natural images and 41% for graphics. The high figure for graphics is given by the fact that this statistical value takes into account also the very frequent zero luminance (black) pixels that are discharged by default regardless of the remaining charge from the preceding pixel.

Figure 6.9 is a graphical representation of the energy saving for three exemplary test images. In each line the following images are displayed in this order: the 5-bit source image, a bitmap of the linearised injection times for conventional driving (section 5.1.2), a bitmap of the SQC injection times, a bitmap with the difference between the two and a last bitmap with the discharge bits.

The bitmap of the SQC injection times is darker than the one of conventional

driving. Energy is saved for most of the pixels, hence the greyness of difference bitmap. Only the graphic pattern has many black pixels in the difference bitmap indicating that in those cases no power is saved. This is due the many black pixels in the source image which implicitly have no potential for power saving.

A discharge bit is set when a very bright pixel is followed by a very dark one and always when the pixel is fully black (i.e. $Lum_{ij} = 0$). A very low percentage of discharge bits is noted for the two natural images, i.e. 0.36 % and 1.01 %. SQC brings about efficiency gains of 61 % and 56 % respectively. For the graphics, in spite of the high number of discharge bits, i.e. 37 %, the power saving rate is still high, i.e. 48 %, meaning that most of them are set for black pixels preceded by rather dark ones - as depicted in the SQC injection bitmap - so that the power loss due to forced discharge is acceptable. It is noted that the portrait images have been rotated and the addressing sequence is from right to left with columns and rows interchanged geometrically.

During the SQC implementation there have been concerns regarding the image stability. It was feared that error accumulation would occur, as the capacitive charge is virtually passed from one row to the next one in the addressing sequence. Nevertheless, the SQC images are perceived as stable and flicker-free. Chapter 7 shows several methods to analyse and demonstrate the robustness of this driving scheme. Also the level of detail and contrast were positively perceived by several viewers, with no shortcomings vis-à-vis conventional driving.

6.3 The Impact on Display Lifetime

The lifetime of an OLED display is of high importance and is quantified by the luminance *half-life* denoted as t_{50} , expressed by the time elapsed until it decays to 50% of its initial value. Several tens of thousands of hours are commonly reported figures nowadays (figure 2.4). They are in a first instance technology and colour dependent. The factors affecting the decay can be further attributed to the material itself or to the driving conditions. The former, induced e.g. through oxygen or water contamination can be overcome by proper encapsulation and sealing [41] so that the driving scheme plays a decisive role not only for the energy budget but also for the lifetime of display modules.

The impact of display driving on the luminance decay of several OLED display



Figure 6.9: Visualisation of power saving and discharge for three test images. In each row from left to right: 5-bit source, linearised conventional driving injection times, SQC injection times, their difference reflecting the power saving, the discharge bitmap

samples has been extensively investigated [41] [66]. The relevant driving parameters affecting the display degradation are temperature and the luminance itself. As described in section 4.1.1, the perceived luminance is proportional to the electrical charge converted into light, i.e. the time-integral of the OLED current. Assuming that the driving current waveform is rectangular in shape, the luminance is thus the product of the driving current density and driving duration, i.e. duty cycle.

The luminance decay has been characterised and curve fitted for variations in temperature, current density and duty cycle. In general, the degradation process can be expressed by the following law:

$$L(t)/L_0 = \frac{1}{1 + (t/t_{50})^\alpha}, \quad (6.2)$$

where L_0 is the initial luminance and α is a shape parameter. In the context of the current work, the current density expressed by the amplitude of the driving current is the variable to be further considered.

Figure 6.10 depicts the measurement and curve fitting results for a sample display driven with four different current amplitudes showing a strong non-linearity.

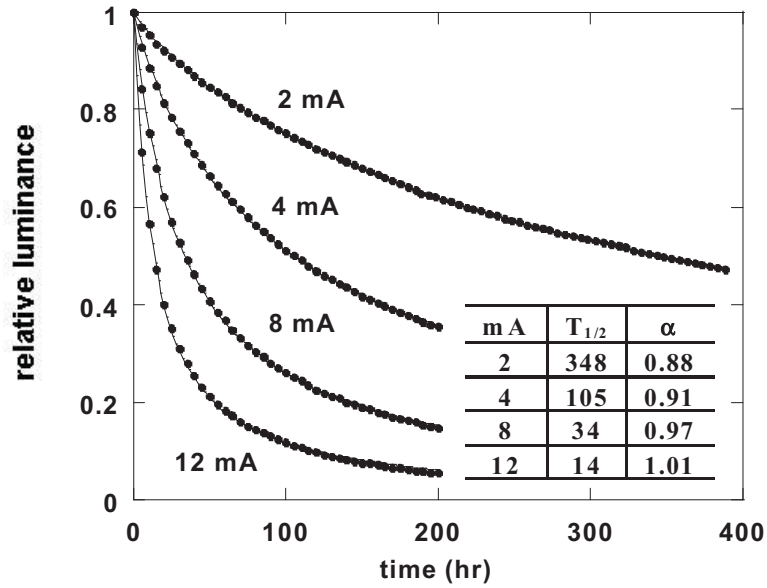


Figure 6.10: The luminance decay of four identical green SMOLEDs driven with different current amplitudes: measurements (dots), empirical fit to equation 6.2 (line) and fitting parameters (table) [41]

In order to quantify the impact of the constant current amplitude, the following equation fitted in [66] can be considered:

$$t_{50}(L) = t_{50}(L_0) \cdot \left(\frac{L}{L_0}\right)^{-c}, \quad (6.3)$$

where the power of decrement is in the range $2.15 \leq c \leq 3.86$ for a duty cycle $3\% \leq \delta \leq 1\%$ respectively. The duty cycle is considered over the entire frame and not only for the row addressing time.

SQC has a twofold impact on display lifetime by allowing a lower constant current amplitude with respect to conventional driving. This is given by:

- discharge at threshold voltage level that becomes the minimum anode voltage, and
- discarding the precharge phase and thus releasing the precharge time that can be used for extending the addressing phase.

The benefits of offsetting the ground potential to the threshold voltage level have already been illustrated in section 4.1.1 and in particular in figure 4.3. Given the voltage-current OLED waveform, it is obvious that if the pixel capacitance is naturally pre-charged at threshold voltage level, it would need a shorter injection time to reach the full-scale luminance than starting from ground potential. To ensure consistency by using the same time scale, hence *lsb*-duration, the constant current amplitude needs to be reduced accordingly. In the chosen example, the amplitude was decreased by ca. 20% from $415 \mu A$ to $330 \mu A$.

The conventional precharge duration is usually several t_{lsb} to charge sufficiently the cumulative anode capacitance, usually to the threshold voltage level of the diodes. In the preliminary research of the present work, a precharge duration of $3 \cdot t_{lsb}$, representing ca. 10% of the row addressing time, was considered appropriate. By discarding this phase, the time can be used for pixel addressing. This is realised by stretching the injection time and reducing the current amplitude accordingly. This technique is a fundamental principle of the Flattened-Singleline-Addressing (FSLA) and the subsequent Multiline-Addressing (MLA) techniques [37].

Even though the display under test has not been characterised in terms of lifetime decay, by means of equation 6.3 the cumulative reduction of injection current amplitude, i.e. $L = 70\% \cdot L_0$, can be translated roughly into an increase in lifetime of factor three, provided that an arbitrary power of decrement of $c = 3$ is chosen. This statement is neglecting duty cycle variation (increase) which is also quantified in [66] and should have a further positive impact.

In conclusion, SQC is a technology granting competitive benefits not only by reducing the power demand of display modules - for the display under test by roughly a factor of two - but also by increasing several-fold their lifetime.

7 SQC Performance and Robustness Considerations

Prior to the validation of SQC driving with discrete drivers (chapter 6) there have been concerns regarding the image quality and stability. More precise, as the algorithm computes iteratively the injection time and final state for each pixel which depend on the desired luminance and the initial state, it is not trivial that in each frame the initial and final states for one pixel are stationary and the luminance is constant. Only constant state variables allow for a stable still image or frame. The main concern has been that a difference between the nominal and actual initial state (voltage) would impact considerably the final state and would accumulate from one pixel to another leading to unsteady consecutive frames for the same image content.

Possible sources of errors are:

- SQC algorithm interpolations,
- SQC algorithm quantisations,
- display characterisation measurements set-up, e.g. ambient light interference, offset and linearity of the photo-sensor read-out chain (photodiode and picoamperemeter), averaging of the piccoamperemeter, the impact of the frame frequency,
- consistency and uniformity of pixel parameters, in particular the capacitance and the diode.

As presented in section 6.2, the perceived quality of the generated still images - natural images, portraits and graphics - is very good and the power saving rate has even exceeded initial expectations. The SQC images are stable, flicker-free and consistent in quality and luminance with the results of conventional driving.

This chapter explores the reasons behind the observed stability of SQC driving and

examines its robustness and fault tolerance. To this end a numerical method for image reconstruction in Matlab was elaborated. An arbitrary variation of physical display parameters would not have been possible in practice, so that the sensitivity analysis can be based at this stage only on numerical calculation and circuit simulation. The numerical exercise is also evidence of the consistency and validity of the theoretical concept and display modelling. Furthermore, PSpice simulations with different initial states are carried out to underpin the fast convergence of the state variables. The actual suppression of state errors is finally proven analytically.

7.1 Investigation Using Matlab

The SQC algorithm is presented in detail in sections 5.2.2 and 5.2.4. Only the 1D-algorithm is used for further testing and validation due to its innovative approach and potential for hardware implementation and mass production. It works in an iterative manner computing for each pixel the SQC injection time and the final state in function of the initial state, the desired luminance and the one-dimensional characterisation measurements of injection and post-luminance.

7.1.1 Convergence of the State Variable

A first evidence for the stability of SQC driving is provided by the output of the algorithm itself. For each column, the initial state of the first pixel is unknown at start-up. To allow for a defined starting point, reset could be performed at the beginning of each frame. However, this global discharge would impact power saving and is to be avoided. Thus, the initial state of the first pixel in one column is de-facto the final state of the last pixel of the column in the previous frame. As SQC is validated with still images only, the driving sequence is a continuous repetition of the same frame, always passing the final state of the last pixel to the first one. This state can however not be known at start-up, while the algorithm still needs a value to process the first pixel in each column of the first frame. It is thus set in Matlab to $V_{1,initial} = V_{th} = 2.5 V$. To assess the convergence of the state variable and the SQC injection times, but also to make sure that the first pixel is processed with the correct initial state once the first frame is completed, the algorithm carries out two iterations for each column.

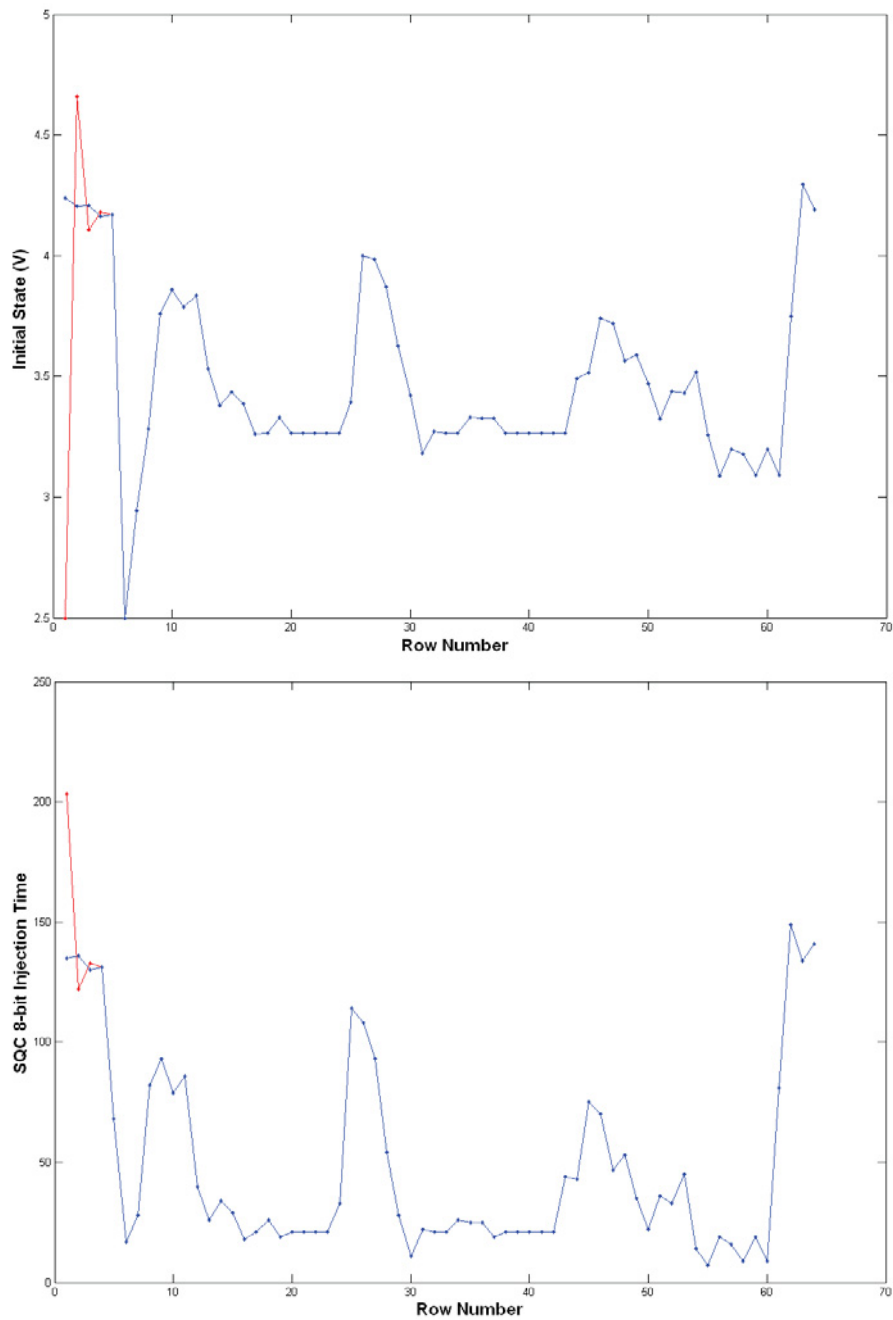


Figure 7.1: Matlab calculation of state variables (top) and SQC injection times (bottom) in one column for two consecutive iterations (first in red, second in blue)

Figure 7.1 shows the outcome of the two frame iterations for computing the initial states and injection times for each pixel in one arbitrary column of a test image. It shows that with two different initial states of $2.5V$ and $4.25V$, the output

converges after four pixels to a stationary set of state variables and injection times, i.e. SQC bit-values. Moreover, the second initial state of the first pixel is the actual final state of the last pixel of the same column so that this set of computed state variables and injection time will remain constant for each repetition of the frame. It is obvious that any deviation of state will not be accumulated but declined within a short time period. In this relatively extreme example it disappears after four rows.

7.1.2 Image Reconstruction

The SQC algorithm uses binary search to compute for each pixel the injection time needed to produce the desired luminance during injection and post-luminescence as a function of a specific initial state. In fact, the algorithm finds $\Delta_{Lum,best}$, i.e. the best match for the nominal luminance (listings 5.2). It is the sum of an injection part Lum_{inj} and a post-luminescence part Lum_{post} , both extracted from the one-dimensional characterisation LUTs (figure 5.25). Due to discretisation and interpolation errors, $\Delta_{Lum,best}$ may slightly deviate from the nominal luminance.

Matlab provides the means to visualise virtually the equivalent of any image generated with SQC driving. This is accomplished by reconstructing the pixel luminances from the values generated by the algorithm and displaying the new matrix using an appropriate function. This can then be compared with the original source image, either through simultaneous visual perception or by computing and assessing the difference matrix.

In a first instance, in order to assess mainly the quantisation errors, a test image was reconstructed from the luminance match determined for each pixel by means of binary search, i.e. $\Delta_{Lum,best}$. The result is depicted in figure 7.2 which shows that this reconstruction is identical to the 5-bit source, a fact also proven by the zero delta matrix. The tiny quantisation errors visible in the higher resolution reconstruction of one column using the native luminance current values (figure 7.4) are eliminated once compressed down to 5-bit.

A more interesting approach is the image reconstruction using the fundamental SQC equation, as for each pixel all parameters are either measurable or computed by the algorithm. While this equation reflects the physical properties of the display, this method allows to mimic the display as accurate as possible. More

important, it also allows to validate the SQC equation and display modelling as they are to some extent decoupled from the characterisation LUTs (figure 5.25). Equation 4.13 can be written as:

$$Lum = k \cdot (I_0 \cdot t_{inj} + C_{eq} \cdot (V_{col,i} - V_{col,i+1})) \quad (7.1)$$

The values of t_{inj} , $V_{col,i}$ and $V_{col,i+1}$ are given by the SQC algorithm itself. The injection current amplitude is set at $I_0 = 330 \mu A$. The cumulative column capacitance C_{eq} and the amplification factor k are determined using the methods described in 3.1. Hence $C_{eq} \approx 63 \cdot 72 pF$ and $k \approx 160 \frac{1}{s}$. The value of this factor is slightly corrected so that the maximum of one arbitrary column in this reconstruction is matching the equivalent of the ideal reconstruction of $\Delta_{Lum,best}$. Hence $k_{corrected} \approx 154 \frac{1}{s}$ delivers the best visual matching. One of the implications of these numerical values is that both components of the pixel luminance, namely the injection charge $Q_{inj} = I_0 \cdot t_{inj}$ and the capacitive charge $Q_{cap} = C_{eq} \cdot (V_{col,i} - V_{col,i+1})$ have the same order of magnitude and neither can be neglected analytically.

Figure 7.2 shows the result of the SQC image reconstruction compressed down to 5-bit next to the image source and the identical ideal reconstruction described above. This virtual SQC image is equivalent to the one that would be generated by the actual display. The difference to the source image is barely perceivable with the bare eye. To highlight it, the delta matrix is computed and reproduced. As no difference in pixel luminance is greater than 1-bit (out of 31), it is amplified and illustrated as artefacts in figure 7.2.

It can be observed that the few 1-bit deviations happen in the very dark regions of the image. All together they account for 1% of the overall image luminance. They could be attributed to the fact that two sensitive parameters of the SQC reconstruction formula, i.e. C_{eq} and k , are approximations as they cannot be determined with higher precision. In addition, they may be eliminated or reduced if the SQC algorithm is implemented with a resolution e.g. of 8 bit or even higher.

A further way for visualising the errors in the two reconstruction approaches is to plot for each one the reconstructed luminance values of all pixels in one arbitrary column and compare them with the equivalent source. This is depicted for one natural image in figure 7.3 highlighting some affected pixels. One error becomes obvious when the nominal constant consecutive luminance of bright pixels is only



Figure 7.2: Image reconstruction in Matlab, from left to right: 5-bit source image, identical reconstruction with $\Delta_{Lum,best}$, SQC image and its 1-bit difference matrix with respect to the source

approximated in the reproductions. As mentioned, for the $\Delta_{Lum,best}$ reproduction the discretisation error is apparently low enough to be eliminated with the 5-bit greyscale resolution.

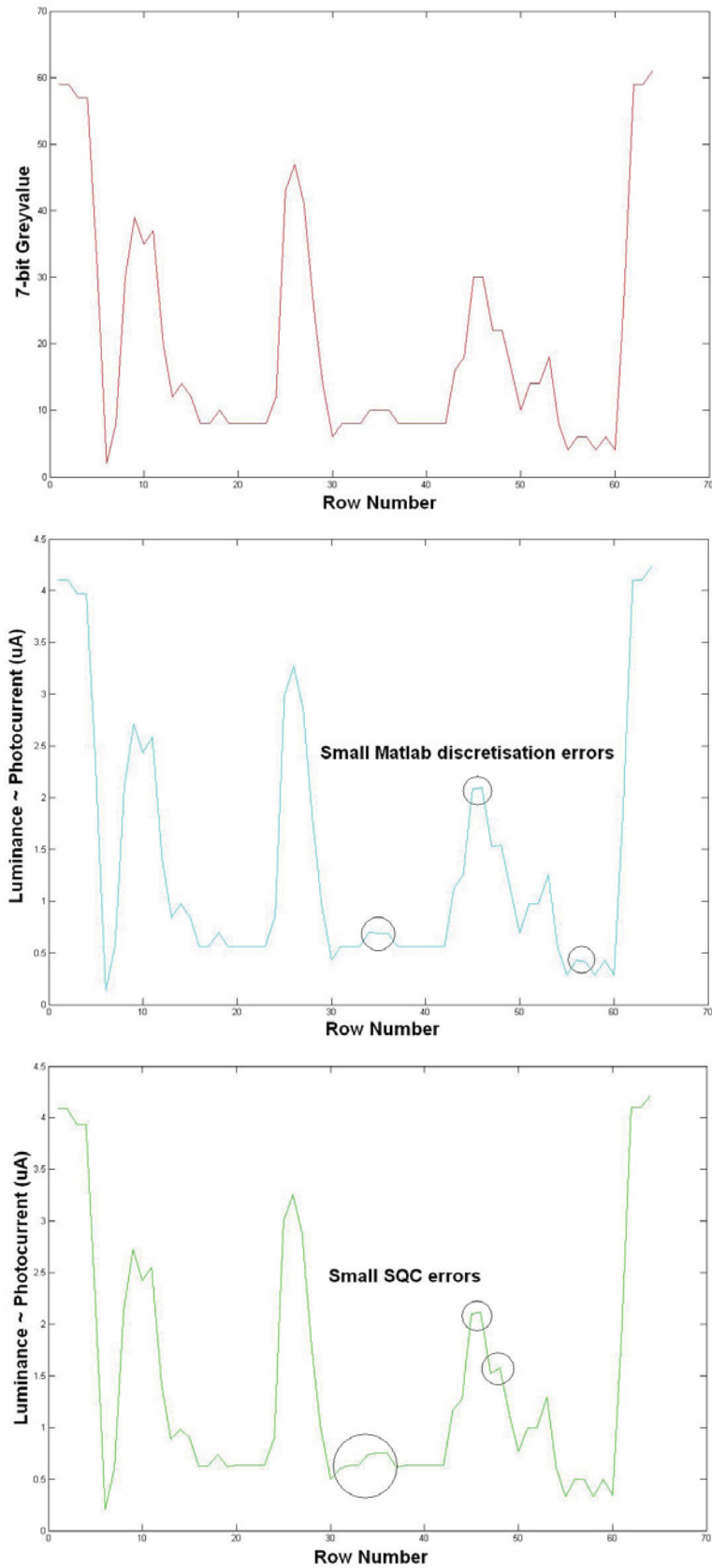


Figure 7.3: Matlab image reconstruction of consecutive pixels, top to bottom: 5-bit source, reconstruction with $\Delta_{Lum,best}$, SQC reconstruction

7.1.3 Sensitivity Analysis

The other sections of this chapter demonstrate the stability of SQC driving, in particular the consistency between the algorithm and the understanding and modelling of PMOLED displays. The visual perception and the image reconstruction prove that pixel parameters are stationary within one column and potential state errors do not accumulate but decline rapidly. Nevertheless, a further concern regarding the SQC image quality and robustness has been raised, namely to what extent they are prone to a variation of display or circuit parameters.

Equation 7.1 is the basis for SQC image reconstruction. For testing the robustness of the driving scheme, the injection current amplitude, the cumulative capacitance and the state variables (voltages) can be varied. k is only a constant amplification factor and can be disregarded for the purpose of this exercise. To easily compare the images before and after parameter variation and to use the same full-scale display range, the current and the capacitance are only reduced, not increased. A reduction by 10% was chosen. This can be considered as a realistic limit for the variations in production. To mimic an uncontrolled variation of each pixel state, the state voltages are reduced randomly within 10%.

It can be observed in figure 7.4 that a reduction of the injection current or cumulative capacitance translates into an overall reduction of brightness, perceived to a large extent as linear, i.e. the image structure is not altered nor does it show artefacts. As in both cases the sum of the delta matrix accounts for 10% of the overall image brightness (sum of grey-values), the dependence can also be considered largely proportional. From this perspective, SQC driving can be considered very robust. Thus it may not be necessary to adjust display parameters like C_{eq} for each individual panel. One parameter extracted for a display model would suffice for mass production.

The result of the random variation of state variables produced artefacts, maintaining however to a large extent the image structure. The delta matrix is noisy, in-line with the random function. The fact that it accounts for 5% of the overall image brightness confirms the uniform distribution of the random generator. Nevertheless, as shown in the other sections of this chapter, this kind of variation of state variables does not occur and robustness is in turn not impacted.



Figure 7.4: Parameter variation in Matlab. From left to right: 5-bit SQC image, SQC reconstruction with parameter variation, difference matrix. From top to bottom: 10% reduction of injection current, 10% reduction of cumulative capacitance, random reduction within 10% of state variables (voltages)

7.2 Circuit Analysis Based on PSpice Simulations

This section presents simulation results supporting the assumption that the state variable is stationary within a column during the SQC addressing sequence. Due to the relatively high cumulative capacitance, the state variables have a considerable impact on the pixel luminance. It is thus important that in practice the voltage at the beginning and the end of the pixel addressing time is consistent with the values predicted by the SQC algorithm. The previous sections showed that a still image generated by means of SQC driving is uniform and stable. This means in turn that any potential error or state deviation from the nominal value is not accumulated but obviously suppressed.

To underpin this conclusion, a PSpice simulation environment was set up to imitate the driving sequence and plot the state variable within one column. For this purpose a circuit simplification has been carried out, in line with the one presented in section 3.4 and depicted in figure 3.10. Furthermore, as the main purpose of this exercise is to study error propagation and any discharge would mean a state reset, SQC driving without discharge is modelled. All pixels are practically equal and the remaining charge is passed from one pixel to the other within one column. An equivalent circuit with one diode tied to ground in parallel to the cumulative column capacitance and the row idle voltage source V_{comh} is thus sufficient. An arbitrary test driving sequence is emulated with a digitally controlled current source allowing for injection and postluminescence durations in the order of magnitude of the real implementation with a row addressing time $t_{row} \approx 150 \mu s$. For the diode model and pixel capacitance, the parameters described in section 3.1 are used.

The main idea behind this simulation is to test the impact of a deviation of the state variable, i.e. the anode voltage, from its nominal values. The easiest way of visualising this effect and assessing it in a qualitative manner is to drive simultaneously two identical diode-capacitance equivalent circuits with the same injection current waveform but different initial states. The latter can be easily implemented in PSpice by assigning two different initial conditions (voltages) to the identical cumulative capacitances. The values $V_{cap,i,1} = -5 V$ and $V_{cap,i,2} = -3 V$ have been set to mimic a very large state deviation with two different initial states of $V_{col,i,1} = 3 V$ and $V_{col,i,2} = 5 V$, provided that $V_{comh} = 8 V$.

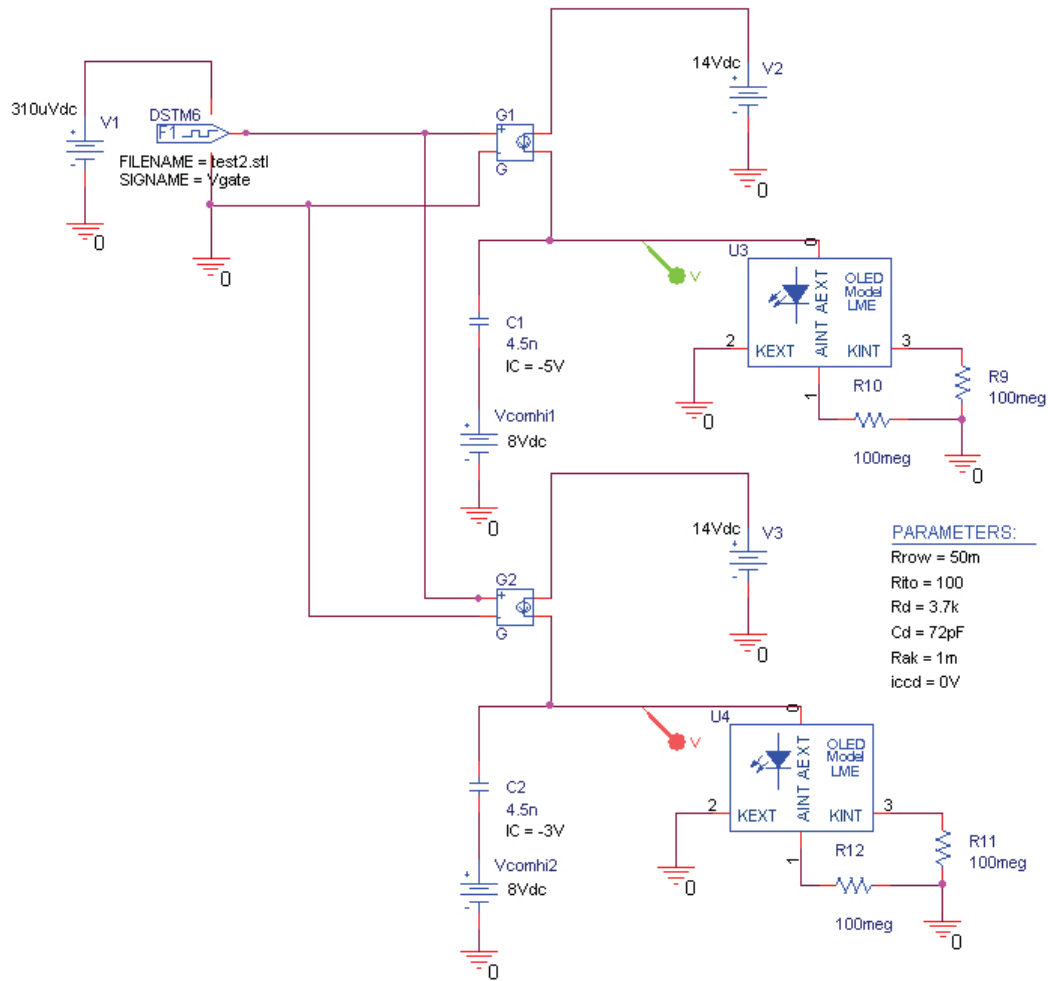


Figure 7.5: Simulation set-up to test the evolution of the state variable with different initial conditions

Figure 7.5 shows the described schematic. The digital driving stimuli are stored in an external file. The two simulated anode voltage waveforms are shown in figure 7.6. It can be observed that even a unrealistically high initial state difference of $2V$ is significantly reduced after the first injection sequence to ca. $200mV$ and it is then fully absorbed during the postluminescence phase and in the next slots. This fact has also been confirmed for other initial values.

The main conclusion is that any deviation of the state variable is phased out very quickly by the nature of the OLED-capacitor system itself. The anode voltage waveform depends mainly on the injection time and current amplitude and considerably less on the initial state. This contributes to the proven stability

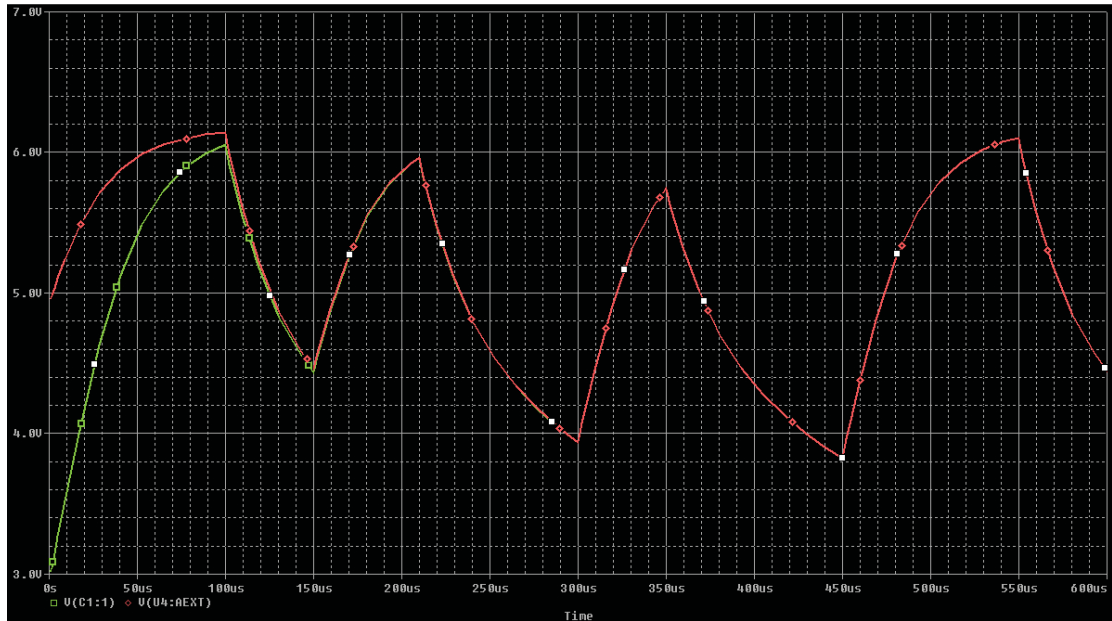


Figure 7.6: Anode voltage waveforms for two different initial states

of the SQC concept. The next section will provide analytical evidence for this error resilience.

7.3 Calculus

Simulations (sections 7.1.1 and 7.2) and experiments (section 6.2) confirm the stability and robustness of SQC driving. The generated test images are flicker and noise free and reproduce genuinely their sources. At the basis of this outcome is the capability of the display itself to suppress any deviation of the state variable, i.e. the anode voltage. This section makes use of an equivalent circuitry and basic equations to demonstrate analytically this property.

As in section 7.2, the equivalent circuit is simplified to a diode-capacitor parallel circuit with an idle row voltage source V_{comh} (figure 7.7).

The purpose is now to prove that any difference between the initial anode voltage and its nominal value is decreasing during the pixel addressing sequence. The latter is split into injection and post-luminescence and the anode voltage waveform is shown qualitatively in figure 7.8 for two different initial states, $V_{A,1} < V_{B,1}$.

It is to demonstrate that

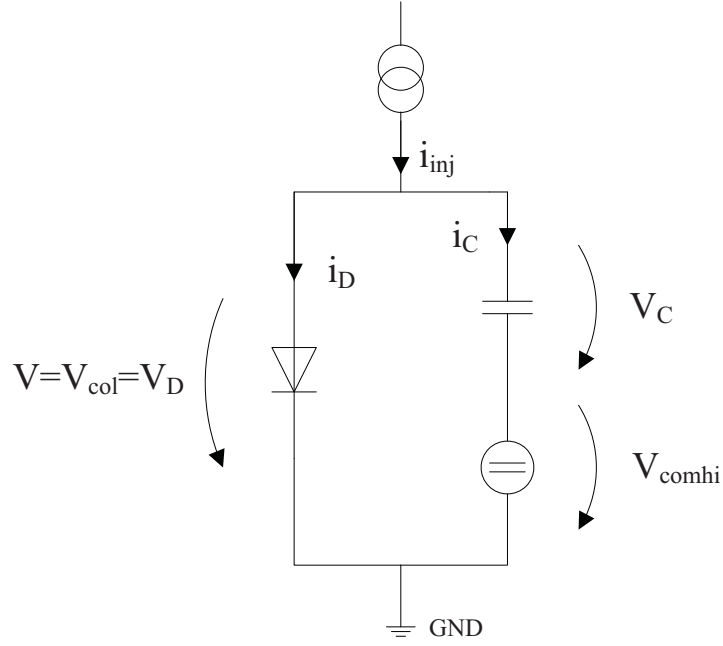


Figure 7.7: Diode-capacitor equivalent circuit

$$\Delta V_1 > \Delta V_2 > \Delta V_3 \quad (7.2)$$

The diode forward current-voltage relation is approximated as:

$$i_D(t) = i_S \cdot (e^{\frac{V_D(t)}{N \cdot V_T}} - 1) \approx i_S \cdot (e^{\frac{V_D}{N \cdot V_T}}) \quad (7.3)$$

for $V_D \gg N \cdot V_T \approx N \cdot 25.8 \text{ mV}$ at 25° C . i_S is the inverse saturation current, usually in the range of a few nA . The emission coefficient N typically varies from 1 to 2 for solid-state diodes. For the current OLED model $N \approx 18$. The capacitive current is:

$$i_C(t) = C \cdot \frac{\delta V_C(t)}{\delta t} \quad (7.4)$$

and $V_C(t) = V_{comh} + V_D(t)$.

Hypothesis 7.2 is demonstrated if the following inequality holds for both sections of the addressing sequence:

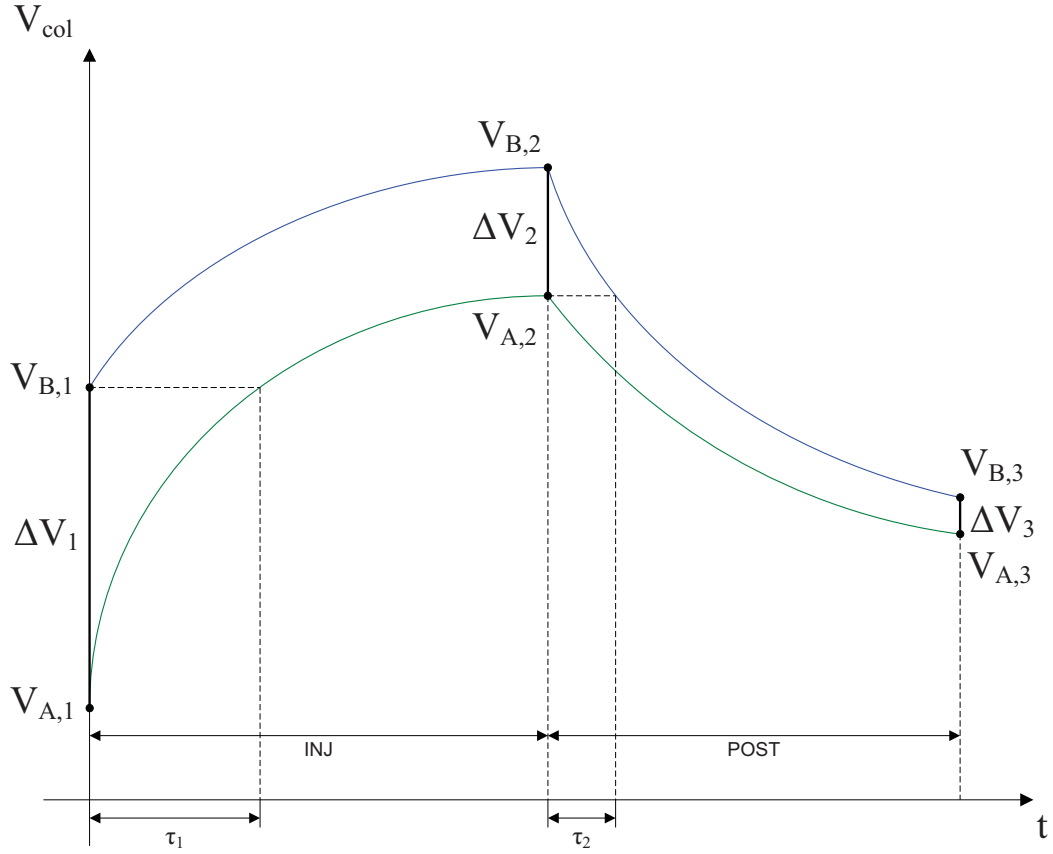


Figure 7.8: Anode voltage difference suppression - qualitative

$$\frac{\delta}{\delta t}(V_B(t) - V_A(t)) < 0 \quad (7.5)$$

For the injection part, the constant injection current equals the sum of the diode and the capacitive current

$$i_D(t) + i_C(t) = i_{inj} \quad (7.6)$$

Given that V_{comh} is constant, $\frac{\delta V_C(t)}{\delta t} = \frac{\delta V_D(t)}{\delta t}$. Together with equation 7.3, 7.6 and 7.4, this leads to:

$$\frac{\delta V_D(t)}{\delta t} = \frac{1}{C} \cdot (i_{inj} - i_S \cdot e^{\frac{V_D(t)}{N \cdot V_T}}) \quad (7.7)$$

with

$$V_D(t) = V_{col}(t) = V(t)$$

The time derivative of the anode voltage difference can be then expressed as:

$$\frac{\delta}{\delta t}(V_B(t) - V_A(t)) = \frac{-i_S}{C} \cdot (e^{\frac{V_B(t)}{N \cdot V_T}} - e^{\frac{V_A(t)}{N \cdot V_T}}) \quad (7.8)$$

As $V_A(t)$ and $V_B(t)$ are in fact the same monotonically increasing function but shifted in time by a constant τ_1 :

$$V_B(t) = V_A(t + \tau_1) \quad (7.9)$$

and

$$V_A(t + \tau_1) > V_A(t)$$

It means in turn that:

$$e^{\frac{V_A(t+\tau_1)}{N \cdot V_T}} - e^{\frac{V_A(t)}{N \cdot V_T}} > 0 \quad (7.10)$$

With $i_S > 0$, inequality 7.5 is thus demonstrated for the injection part such that $\Delta V_1 > \Delta V_2$.

In the case of post-luminescence, the inequality is demonstrated in an analogue manner. The injection current is zero and the initial conditions are $V_{A,2} < V_{B,2}$. The voltage decay in a diode-capacitor circuit has been investigated in [34] confirming a logarithmic curve.

With $i_{inj} = 0$ and $V_A(t)$ and $V_B(t)$ being the same monotonically decreasing function but shifted in time by a constant τ_2 , so that $V_A(t) = V_B(t + \tau_2)$, the equivalent of equation 7.8 becomes:

$$\frac{\delta}{\delta t}(V_B(t) - V_A(t)) = \frac{-i_S}{C} \cdot (e^{\frac{V_B(t)}{N \cdot V_T}} - e^{\frac{V_B(t+\tau_2)}{N \cdot V_T}}) \quad (7.11)$$

Given that $V_B(t) > V_B(t + \tau_2)$, it means in turn that

$$e^{\frac{V_B(t)}{N \cdot V_T}} - e^{\frac{V_B(t+\tau_2)}{N \cdot V_T}} > 0 \quad (7.12)$$

With $i_S > 0$, inequality 7.5 is also demonstrated for the post-luminescence part so that overall $\Delta V_1 > \Delta V_2 > \Delta V_3$. This analytical proof shows that any deviation from the nominal state variable is diminished by the system itself throughout the addressing process. In addition, this constructive decay is very fast, a fact demonstrated in practice and by the simulation outlined in section 7.2. This property is instrumental for the anode voltage to be stationary and stable during a frame addressing sequence, regardless of the initial state and of potential local deviations which is a pre-requisite for the proven image quality.

8 Summary, Future Work and Potential Impact

8.1 Summary

The main outcome of the present work is the elaboration and demonstration of a new power-efficient driving scheme for passive-matrix OLED displays, ranging from conceptual design to hardware validation using discrete electronics and programmable logic.

To this end, a monochrome polymer OLED display has been modelled and characterised and a scalable PSpice simulation environment has been set up.

The power loss in conventional PMOLED drivers has been analysed and broken down into its resistive and capacitive components. In addition, the dependency on the display resolution has been shown on the basis of a numerical example. The new driving scheme has been designed with the purpose of avoiding the dominating capacitive power loss, in particular of high-resolution displays.

In a first instance, the principle of *natural* discharge (post-luminescence) has been introduced. In conjunction with discharge at threshold voltage level it already improves the power budget of the driver considerably. The remaining capacitive power dissipation is then overcome by eliminating the discharge phase for the majority of the pixels. This means in turn that within one column the remaining capacitive charge at the end of the row addressing time is passed to the next addressed pixel so that the energy stored in OLED capacitances is not wasted but conserved. The challenge arising with this approach is the fact that the initial voltage (state) before each addressing sequence becomes variable.

An analytical method to estimate the display- and content-dependent power saving potential of SQC has been elaborated. To ensure consistency in the comparison

of driving schemes, a method for linearising the luminance transfer functions has been applied.

An algorithm has been co-developed in order to compute upfront the digital control signals, e.g. the injection time for each pixel as a function of the initial state and the display properties. The light emission is correlated with the time integral of the OLED current. The driving scheme is thus denoted as state-dependent and charge-controlled (SQC).

The SQC concept has been first validated on the basis of a straightforward method requiring complex 2D-LUT display characterisation and large memory resources. An innovative approach with simplified 1D-characterisation and an algorithm using fast binary search has been then introduced and validated. This algorithm allowed an efficient hardware implementation demonstrated within a subsequent diploma thesis [24].

To prove the visual quality and the benefits of SQC, a demonstrator using discrete components has been designed and set up to drive two 96 x 64 displays simultaneously. The SQC algorithm has been used to generate in Matlab the pixel injection times for each image. This data has been then transferred with a graphical user interface to the on-board FPGA to control the column drivers and generate the test images to be validated. The generation of digital driver control signals was done in VHDL.

A set of 36 still greyscale images - 18 natural images and 18 graphics - has been used to test and benchmark SQC with respect to conventional driving. An average power saving rate of 50% (58% for natural images and 43% for graphics) has been measured. As supported by a numerical example, this figure is expected to rise above 80% with increasing resolutions and decreasing thickness of OLED displays. The SQC image quality is very good, with no perceivable difference with respect to conventional driving. In the current set-up, some very minor loss of dark details may be compensated by employing a higher grey-scale resolution during pre-processing.

In addition to experimental validation, numerical methods have been developed to assess this novel driving scheme. An image reconstruction technique has been used in Matlab to demonstrate the validity of the SQC theory and investigate visually potential quantification errors.

The SQC development has ended with an assessment of robustness and sensitivity

to display parameter variation using Matlab reconstruction, PSpice simulation and calculus. The outcome has confirmed the perceived stability and image brilliance.

In addition to power saving, another key parameter, i.e. the lifetime of PMOLED displays, is improved several-fold, roughly by a factor of three for the display under test. The SQC driving scheme is thus an enabling technology for efficient PMOLED display modules.

8.2 Outlook and Future Work

The feasibility and benefits of SQC driving have been demonstrated. Nevertheless, the proof of concept has been limited to one single monochrome display model and applied to a set of still test images with constant brightness and frame rate. Should SQC ever be industrially exploited, the following configurations need to be qualified as well, also as most of them can be adjusted in current mobile devices:

- full-video with different frame rates
- RGB colour
- different brightness levels
- different image settings (e.g. contrast, saturation, hue, colour temperature)
- several displays, different in size and resolution
- characterisation and compensation for ageing and wear-out.

To implement a discrete brightness scale, there are two basic approaches. Either the display is fully characterised with different anode current amplitudes and a set of LUTs is made available for each brightness level, or one single nominal LUT is generated and the other brightness settings are approximated with a linear equation as described in [4] and supported by the outcome of current amplitude variation presented in section 7.1.3. The latter approach may lead to some non-uniform brightness variation while the former may be memory intensive.

An important constraint for commercial usage is the realisation as integrated circuit. To this end, an SQC processor has been subsequently developed and implemented in FPGA [24]. The pipeline architecture meets the real-time processing requirements and allows for reasonable chip size and cost. In addition, the driving scheme has been extended with a high-current precharge phase to facilitate shorter row addressing times and increase efficiency and lifetime. Overall, the current

results confirm the feasibility of SQC system integration.

To combine the power efficiency of SQC with further lifetime extension techniques, its application to flattened singleline (FSLA) or multiline addressing (MLA) can be explored. This may however be particularly challenging due to the variable row addressing time requiring complex multi-dimensional LUTs. Nevertheless, in [52] the application to multiline addressing is declared feasible.

8.3 Innovation Potential

The decreasing number of publications and the very few commercial products launched over the past years acknowledge the decay of PMOLED in favour of AMOLED. The main reason is the requirement for high display resolutions even on small glasses. A breakthrough has been further hindered by the driver chip being usually placed on the shorter display edge, so that the longer edge is the cathode side leading to a higher number of rows.

Nevertheless, PMOLED may still satisfy a niche market of applications with flexible or transparent small to medium-size displays like smart-watches or fitness monitors [35]. Should this be the case, SQC driving will become a mandatory technology due to the high power-saving benefits.

By reducing the driving current amplitude SQC is eligible not only for impacting the power demand of display modules but also for increasing their lifetime.

SQC might be also applied to energy-sensitive components with a similar matrix structure and sheet capacitance, likely to be found in mobile high-resolution sensor or memory arrays.

Bibliography

- [1] Antoniadis, H. 2003. *An Overview of OLED Display Technology - OSRAM Opto Semiconductors Inc* [Online], http://www.avsusergroups.org/tfug_pdfs/TFUG_05_2003_Antoniadis.pdf [Accessed: August 2014].
- [2] Agilent 2014. *Agilent InfiniiVision 5000/6000/7000 Series Oscilloscopes* [Online], <http://cp.literature.agilent.com/litweb/pdf/54695-97015.pdf> [Accessed: August 2014].
- [3] Bender, J. P., Norris, B. J., Wager, J.F. 1998. *OLED Modelling via Spice*, International Workshop on Organic Electroluminescence 87-90, 4th International conference on the science and technology of display phosphors.
- [4] Bender, A. 2008. *Analyse und Evaluation eines verlustleistungsoptimierten Treiberschemas für ein Passive-Matrix-OLED-Display*, Diploma Thesis, Institute of Microelectronics, Saarland University.
- [5] Bockaert, V. 2014. *Sensor Linearity* [Online], www.dpreview.com/glossary/camera-system/sensor-linearity [Accessed: August 2009].
- [6] Buczek, M. 2007. *Verlustleistungsoptimiertes Treiberschema für ein PMOLED - Display*, Diploma Thesis, Institute of Microelectronics, Saarland University.
- [7] Buczek, M., Codrea, C., Jung, T., Wahl, J., Xu, C. 2009. *Innovative addressing scheme to enhance the lifetime of PMOLED displays*, Proceedings of Electronic Displays Conference, Nuremberg, Germany.
- [8] Buczek, M., Codrea, Xu, C. 2010. *Multiplied Power Efficiency of PMOLED through SQC - a driving scheme converting capacitive energy into light*, Proceedings of Electronic Displays Conference, Nuremberg, Germany.
- [9] Buczek, M. 2008. *Various*, Matlab Code.

Bibliography

- [10] Cadence 2014. *Allegro AMS Simulator* [Online], www.cadence.com/products/pcb/ams_simulator/pages/default.aspx [Accessed: August 2014].
- [11] Carton, P. 2014. *MiniUART IP Core Specification, VHDL utility file, GNU public license* [Online], www.opencores.org [Accessed: August 2014].
- [12] Chaussy, D., Mas, C., Tupin, F. 2006. *New OLED Driver IC Optimizes Module Power Consumption, Image Quality, Reliability, and Cost*, SID Symposium Digest of Technical Papers, Volume 37, Issue 1, p.406–409.
- [13] Chen, S.-Y., Li, Y.-M., Chen, C.-L., Chiang, J. 2003. *Low Peak Current Driving Scheme for Passive Matrix-OLED*, SID Symposium Digest of Technical Papers 01/2003, 34(1).
- [14] Chen, S.-L. 2005. *Method for Driving Passive Matrix OLED*, Patent Application US20060279492 A1.
- [15] Clare Micronix 2002. *AN100.3 - Using the MXED102 and MXED202*, Application Note.
- [16] CNET 2014. *Samsung Gear S review: The smartwatch that's also a smartphone* [Online], www.cnet.com/products/samsung-gear-s/ [Accessed: August 2014].
- [17] Codrea, C., Buczek, M., Xu, C. 2008. *A Power-Efficient Driving Scheme for PMOLED Displays*, Int. Proceedings IDRC, Orlando, USA, p.75.
- [18] Codrea, C., Buczek, M., Xu, C. 2009. *Increasing PMOLED Efficiency by Decimating the Charging/Discharging Power Loss*, 16th International Display Workshops, IDW, Miyazaki, Japan, Volume 1.
- [19] Colegrove, J. 2012. *OLED Display and OLED Lighting: Technologies and Market Forecast - DisplaySearch*, Semicon West Conference.
- [20] Dagois, J.-P. 2003. *Image Display Device with Capacitive Energy Recovery*, Patent Application US20060125733 A1.
- [21] Dialog Semiconductor 2008. *DA8622 WQVGA PMOLED driver*, Product Brief.
- [22] Dialog Semiconductor 2010. *DA8620 240 x 320 OLED Driver*, Data Sheet.

- [23] Digilent 2014. *Digilent D2FT FPGA-Based Development Board - product site* [Online], www.digilentinc.com/Products/Detail.cfm?Prod=D2FT [Accessed: August 2014].
- [24] Dobrev, Y. 2010. *Analyse und Evaluation eines verlustleistungsoptimierten Treiberschemas für ein Passive-Matrix-OLED-Display*, Diploma Thesis, Institute of Microelectronics, Saarland University.
- [25] Eagle 2009. *EAGLE PCB Design Software* [Online], www.cadsoft.de/?language=de [Accessed: August 2009].
- [26] Eisenbrand, F., Hitzelberger, C., Karrenbauer, A., Soh, K. M., Wahl, J., Xu, C. 2005. *Method for Driving Matrix Displays - Verfahren zur Ansteuerung von Matrixanzeigen*, Patents DE102005063159 B4, EP1966786A1, WO2007079947A1, US20090195563, CN101366069A.
- [27] Electronic Design 2001. *OLED And Cholesteric Displays Demand New Driver-IC Designs* [Online], <http://electronicdesign.com/displays/oled-and-cholesteric-displays-demand-new-driver-ic-designs> [Accessed: August 2009]
- [28] Fluke 2009. *Fluke Digital Multimeters - product site* [Online], www.fluke.com/fluke/r0en/Products/ [Accessed: August 2009].
- [29] Freudenrich, C. 2014. *How OLEDs Work* [Online], <http://electronics.howstuffworks.com/oled3.htm> [Accessed: August 2014].
- [30] Fyfe, D. 2007. *Total Matrix Addressing for OLED Displays*, 9th Annual DisplaySearch US FPD Conference.
- [31] Graham, L. 2014. *AMOLED Mobile Phone Panel Costs Expected to Fall Below LCD - press release* [Online], www.displaysearch.com/cps/rde/xchg/displaysearch/hs.xsl/140716_amoled_mobile_phone_panel_costs_expected_to_fall_below_lcd.asp [Accessed: August 2014].
- [32] Han, X. 2007. *Development of an OLED circuit model*, preliminary research, Institute of Microelectronics, Saarland University.
- [33] Heider, U. 2013. *OLED - Status quo and Merck's position*, Merck Information Day 2013, Darmstadt, Germany.
- [34] Hellen, E. H. 2003. *Verifying the diode-capacitor circuit voltage decay*, American Journal of Physics 71, p.797.

Bibliography

- [35] Huawei 2014. *Talkband B1 - product site* [Online], <http://consumer.huawei.com/minisite/worldwide/talkband-b1/index.htm> [Accessed: August 2014].
- [36] HyperPhysics 2014. *Resistivity and Temperature Coefficient at 20 C* [Online], <http://hyperphysics.phy-astr.gsu.edu/hbase/tables/rstiv.html> [Accessed: August 2014].
- [37] Karrenbauer, A. 2007. *Engineering Combinatorial Optimization Algorithms to Improve the Lifetime of OLED Displays*, Dissertation, Saarland University.
- [38] Keithley 2009. *Model 6485 5-1/2 digit Picoammeter with 10fA Resolution - product site* [Online], www.keithley.com/products/dcac/sensitive/lowcurrent?mn=6485 [Accessed: August 2009].
- [39] Kietzke, T. 2013. *LCDs -A high hurdle for new large display technologies*, Merck Information Day 2013, Darmstadt, Germany.
- [40] Kim, J., Kim, S. 2009. *Design of a PMOLED Driver Circuit to Compensate for the Non-Uniformity Problem in the Manufacturing Process*, *Journal of the Korean Physical Society*, Vol. 55, No. 5.
- [41] Kobrin, P., Boehmer, E., King, P., Fisher, R., Robinson, S., Green, P. 2003. *Time Dependence of OLED Luminance*, SID Symposium Digest of Technical Papers Volume 34, Issue 1, p.539–541.
- [42] Landsburg, G, 2002. *Drivers for Novel Displays - OLEDs and bistable LCDs require special driver chips that combine digital and analog IC technologies*, Information Display, vol. 18, p.18-23.
- [43] LeChevalier, R. 2003. *Ramp Control Boost Current Method*, Patent Application US20030156101 A1.
- [44] LeChevalier, R. 2006. *Method and System for Precharging OLED/PLED Displays With a Precharge Latency*, Patent US6943500 B2.
- [45] Lenovo 2014. *Lenovo S800 - product site* [Online], <http://lenovomobile.com.ph/mobile-phones/s800> [Accessed: August 2014].
- [46] LG 2014. *LG OLED TV - product site* [Online], www.lg.com/us/experience-tvs/oled-tv/oled-display.jsp [Accessed: August 2014].
- [47] Mathworks 2014. *PSpice SLPS and Cadence Allegro AMS Simulator SLPS*

- [Online], www.mathworks.nl/products/connections/product_detail/product_35793.html [Accessed: August 2014].
- [48] Mathworks 2014. *Matlab - The Language of Technical Computing* [Online], www.mathworks.nl/products/matlab/ [Accessed: August 2014].
- [49] Maxtec 2014. *MD300 C2 Pulse Oximeter - datasheet* [Online], <http://www.maxtec.com/wp-content/uploads/2014/11/MD300C2DataSheet.d.pdf> [Accessed: August 2014].
- [50] Mertens, R. 2014. *OLED* [Online], www.oled-info.com/pmoled [Accessed: August 2014].
- [51] Microsoft 2014. *Microsoft Visual Studio* [Online], www.microsoft.com/germany/visualstudio/default.aspx [Accessed: August 2014].
- [52] Miller, M. E., Arnold, A. D., Hamilton Jr., J.F. 2007. *Reduced Power Consumption in OLED Display System*, Patent Application US20090021455 A1.
- [53] Nanomarkets 2014. *Opportunities for OLED Materials* [Online], <http://de.slideshare.net/NanoMarkets/oled-mater> [Accessed: August 2014].
- [54] Ng, R. 2004. *Design and Application of OLED Drivers - Solomon Systech* [Online], www.eetasia.com/ARTICLES/2004APR/A/2004APR22_MSD_TAC.pdf [Accessed: August 2014].
- [55] NASA 2012. *This Week at NASA ...* [Online], www.nasa.gov/multimedia/podcasting/TWAN_11_23_12_prt.htm [Accessed: August 2014].
- [56] Newport 2012, *818 Series Photodetector Guide*, User's Manual.
- [57] OKI Semiconductor 2005, *ML9362DVx Specification (258-Channel Organic EL Anode Driver)*, Datasheet.
- [58] OLED Association 2014 . *Continued Advances in OLED Technologies and Materials Accelerate the Emergence of New High Performance Displays and Lighting Products* [Online], www.swarthmore.edu/NatSci/echeeve1/Ref/MatlabCurveFit/MatlabCftool.html [Accessed: August 2014].
- [59] Otellini P., Gelles J. 2012. *Obama in Arizona to applaud Intel as a tech leader in American manufacturing* [Online], <http://articles.philly.com/2012->

Bibliography

- 01-26/business/30667060_1_moore-s-law-intel-ceo-paul-otellini-smartphones-and-tablets [Accessed: August 2014].
- [60] OTI Lumionics 2014. *OLED History* [Online], www.otilumionics.com/oleds/history/ [Accessed: August 2014].
- [61] Roberts, M., Akino, N., Asada, K., Benzie, P., Hamamatsu, H., Hatcher, M., King, S., Snedden, E., Stevens, A., Tanaka, S., Toner, J., Wilson, R., Young, W., Yamada, T. 2012. *Progress in Polymer OLED Efficiency*, ICCEL2012, Fukuoka, Japan, 2012.
- [62] Samsung 2014. *Samsung Galaxy Tablet S - product site* [Online], www.samsung.com/global/microsite/galaxytabs/ [Accessed: August 2014].
- [63] Sekine, C., Tsubata, Y., Yamada, T., Kitano, M., Doi, S. 2014. *Recent progress of high performance polymer OLED and OPV materials for organic printed electronics*, Science and Technology of Advanced Material, Volume 15, Number 3.
- [64] Smith, E.C. 2008. *Total matrix addressing*, Journal of the Society for Information Display, Volume 16, Issue 2, pages 201–209.
- [65] Soh, K. M., Klein, S., Hitzelberger, C., Xu, C. 2005. *Electrical and optical characterization of PM OLED displays*, Proceedings of the 25th Display research conference, EuroDisplay 2005, p.393-396.
- [66] Soh, K. M. , Xu, C., Hitzelberger, C. 2006. *Dependence of OLED Display Degradation on Driving Conditions*, SID Mid Europe Chapter Fall Meeting.
- [67] Soh, K. M. 2007 *jpg-to-coe.m*, Matlab Code
- [68] Solomon Systech 2007, *SSD1331, 96RGB x 64 Dot Matrix OLED/PLED Segment/Common Driver with Controller*, Datasheet.
- [69] Somerville, A., Hiroshima, S., Kitaguchi, T. 2009. *Back to Back Pre-charge Scheme*, Patent Application US20100295845 A1.
- [70] Sony 2014. *Sony Ericsson Liveview watch micro display* [Online], www.sonymobile.com/de/products/accessories/liveview/ [Accessed: August 2014].
- [71] STMicroelectronics 2014, *Notebook LED backlight: what's down the road to make green tech a leverage for final customers choice*. [Online],

- www.st.com/st-web-ui/static/active/cn/resource/sales_and_marketing/promotional_material/magazine/TP%201058%20Notebook%20LED%20backlight%203.pdf [Accessed: August 2014].
- [72] Strasser, E. 2014. *What's so Difficult about Making an OLED TV?* [Online], <http://news.oled-display.net/lg-launch-curved-ultra-hd-4k-oled-tv-in-q4-2014/> [Accessed: August 2014].
- [73] Tanghe, G., Thielemanns, R. 2003. *Organic light-emitting diode (Oled) pre-charge circuit for use in a large-screen display*, Patents US7079092 B2, EP1471493 A1.
- [74] Tietze, U., Schenk, C., 2002. *Halbleiter-Schaltungstechnik*, Springer, 12. Auflage.
- [75] VLSI Standards 2014. *ITO Sheet Resistance Standard* [Online], www.vlsistandards.com/pdf/products/Electrical/ITO.pdf [Accessed: August 2014].
- [76] Volkert, P., Xu, C. 2014. *Principle and validation of digital driving for active matrix organic light emitting diodes displays*, Journal of the Society for Information Display, Volume 22, Issue 1, p.43-54.
- [77] Wager, J. F. 2014. *Flat-Panel-Display Backplanes: LTPS or IGZO for AMLCDs or AMOLED Displays?* [Online], <http://informationdisplay.org/IDArchive/2014/MarchApril/FrontlineTechnologyDisplayBackplanes.aspx> [Accessed: August 2014].
- [78] Wikipedia 2014. *OLED* [Online], <http://en.wikipedia.org/wiki/OLED> [Accessed: August 2014].
- [79] Wikipedia 2014. *Gamma correction* [Online], http://en.wikipedia.org/wiki/Gamma_correction [Accessed: August 2014].
- [80] Xilinx 2009. *ModelSim Xilinx Edition* [Online], www.xilinx.com/tools/mxe.htm [Accessed: August 2009].
- [81] Xilinx 2009. *ISE WebPACK Design Software* [Online], www.xilinx.com/products/design-tools/ise-design-suite/ise-webpack.htm [Accessed: August 2009].
- [82] Xilinx 2011. *Virtex-5 LX FPGA FF1760 Prototyping Platform* [Online],

- www.xilinx.com/products/boards-and-kits/hw-afx-ff1760-500-g.html
[Accessed: August 2014].
- [83] Xilinx 2011. *Virtex-5 LX FPGA Prototype Platform User Guide* [Online], www.xilinx.com/support/documentation/boards_and_kits/ug222.pdf
[Accessed: August 2014].
- [84] Xilinx 2013. *Spartan-IIe FPGA Family Data Sheet* [Online], www.xilinx.com/support/documentation/data_sheets/ds077.pdf
[Accessed: August 2014].
- [85] Xilinx 2014. *Virtex-5 FPGA Data Sheet* [Online], www.xilinx.com/support/documentation/data_sheets/ds202.pdf [Accessed: August 2014].
- [86] Xu, C., Soh, K. M., Hitzelberger, C. 2006. *Dependence of OLED Display Degradation on Driving Conditions*, SID Mid Europe Chapter Fall Meeting.
- [87] Xu, C., Karrenbauer, A., Soh, K. M., Codrea, C. 2008. *Consecutive multiline addressing: A scheme for addressing PMOLEDs*, Journal of the Society for Information Display, Volume 16, Issue 2, pages 211–219.
- [88] Xu, C., Codrea, C., Karrenbauer, A. 2008. *Verfahren und Treiber zum Ansteuern einer Passivmatrix-OLED-Anzeige / Method and Driver for Actuating a Passive-Matrix OLED Display*, Patent Applications DE102008024126 A1, US20110181632, WO2009141085A1, CN102037506A.
- [89] Xu, C. 2009. *Mikroelektronik 4*, Lecture slides, Institute of Microelectronics, Saarland University.
- [90] Xu, C. 2010. *Gamma-Korrektur-Algorithmen mit Lookup-Tabellen zur Steuerung von PMOLED Displays*, Patent Description - not published.
- [91] Yang, J.-S., Yoo, D.-J., Yun, J.-R., Seong, E.-K., Lee, J.-H., K.-S., Park, J.-K., Se, J.-Y., Kim J.-Y. 2006 *PMOLED Driver Design with Pre-charge Power Saving Algorithm*, SID Symposium Digest of Technical Papers, Volume 37, p.347-350.